Bridging Atomistic and Continuum Space Charge Models in Solid Electrolytes

Wellock, Georgie

Award date:
2020

Awarding institution:
University of Bath

Thesis

Bridging Atomistic and Continuum Space Charge Models in Solid Electrolytes

Georgina Leanne Wellock

A thesis submitted for the degree of Doctor of Philosophy

University of Bath

Department of Chemistry

September 2019

Abstract

The use of solid state electrolytes in electrochemical devices has become paramount in recent decades. The increased utilisation is due to the provision of important advantages with respect to the conventional industrial processes of the relevant technologies. In particular, the use of solid electrolytes offer for technologies such as batteries, increased safety and potentially higher ionic conductivities, and for solid oxide fuel cells, high energy conversion efficiency, improved robustness and greater fuel flexibility. Solid electrolytes have the ability to conduct due to defects in the crystal lattice. These defects include ionic vacancies where an ions are removed from their explicit sites creating diffusion paths throughout the material.

Most solid electrolytes used in solid state electrochemical devices are polycrystalline, with regions of crystallographic disorder (grain boundaries) separating regions that are perfectly crystalline (bulk). The structural distortion in the grain boundaries creates a difference in chemical potential compared to the bulk which in turn causes variations in defect segregation energies (the change in free energy associated with moving a defect from the bulk to a boundary). Non-zero segregation energies indicates spontaneous redistribution of defects from the bulk to, or away from, the grain boundaries.

Segregation of defects to, or away from grain boundaries results in the formation of space charge. Space charge comprises of a charged grain boundary core, where defects are accumulated or depleted respectively and adjacent space charge regions where electrostatic forces dictate a region of depleted or accumulated charge carriers respectively. The variation of charge carriers in these regions can result in a large variation in ionic conductivity throughout the material.

The formation and resulting effects of space charge regions can be studied mathematically by solving Poisson's equation. In this thesis we discuss a mathematical framework and the associated open source software produced throughout the project for modelling space

charge formation on a site explicit basis, and the effect on the ionic conductivity under a range of conditions. The simulations carried out include, different materials, different grain boundary orientations and different inter-grain boundary separations under a variety of conditions including, but not limited to, the effect of defect concentrations and temperatures.

Declaration of work done in conjunction with others

The main results presented throughout this thesis are calculated using a Poisson-Boltzmann solver which required input data in the form of defect segregation energies and defect positions. This input data been calculated by collaborators at the University of Bath.

For chapters 5-7, the $Gd-CeO_2$ crystal structures were created and defect segregation energies calculated using classical interatomic potential methods by Joel Statham and Dr. Marco Molinari.

For chapter 6, the Li_3OCl crystal structures were created and defect segregation energies calculated using density functional theory by Dr. James Dawson and Prof. Pieremanuele Canepa.

The methods used to create the crystal structures and calculate the defect segregation energies are described in detail in chapter 2.

Acknowledgements

This thesis becomes a reality with the kind support and help of many individuals. I would like to express my sincere thanks to all of them.

First and foremost, my gratitude goes to my primary supervisor Dr. Benjamin Morgan who has provided exceptional guidance throughout my postgraduate education. His unwavering enthusiasm kept me engaged through the highs and lows, and his ability as a teacher has developed my skills not only in science, but also in clear communication and software engineering. His influence and wealth of knowledge helped me successfully carry out this project. My gratitude extends to my secondary supervisor Prof. Steve Parker, who always offered a fresh perspective and imaginative discussion throughout the project.

I am also incredibly grateful to the rest of the Morgan Group, who have been an absolute pleasure to work alongside over the past 4 years. In particular, I am thankful to Dr. Conn O'Rourke who has been there from the start, always willing to offer a shoulder to cry on. To Alex Squires for his exceptional scientific insight and support, and to Jacob Dean for his willingness to help and unparalleled banter.

I would also like to express my thanks to my collaborators for their assistance and wisdom, to the insightful individuals I have met at conferences for their exciting discussions and to the members of the other Computational Chemistry groups at the University of Bath who have made the past four years incredibly enjoyable.

Finally, I will forever appreciate the unconditional love and support from my family. Throughout my PhD, my parents and sister Katherine have always offered encouragement, a positive outlook, and some tough love when required. My closest friends Eleanor and Verity have provided constant cheer and my partner Samuel brightened every day, offering motivation in his sincere interest in my work and in his passion for knowledge.

Contents

List of Figures

List of Tables

Chapter 1

Solid Electrolytes

1.1 Introduction

Solid electrolytes are solid materials that conduct electricity through the motion of ions, and exhibit negligible electronic transport.[3] Solid electrolytes include both crystalline and amorphous inorganic solids, as well as ion-conducting polymers.[4] Crystalline solid electrolytes can have high ionic conductivities, with ionic species migrating through the mobile ion sublattice, a rigid framework with channels that act as ionic conduction pathways.[5] Ionic diffusion occurs in all ionic solids, but in most materials this process is slow. The contrasting fast ion diffusion exhibited by solid electrolytes makes them useful in a variety of applications, such as solid oxide fuel cells[6,7] and all–solid-state batteries.[8,9]

1.1.1 Solid Electrolytes in Fuel cells

Fuel cells are electrochemical cells that generate electricity from an electrochemical reaction between oxygen and hydrogen.[10] A fuel cell consists of two electrodes separated by an electrolyte and can produce electricity continuously, providing fuel and oxygen are supplied.[11] The first fuel cell was invented by William Grove in 1839.[12] He conducted experiments in a gas voltaic battery and proved that electric current could be produced from an electrochemical reaction between hydrogen and oxygen in the presence of a platinum catalyst.[13] Despite being first demonstrated nearly two centuries ago, it is only in the last three decades that fuel cells have offered a realistic prospect of being commercially viable.[7]

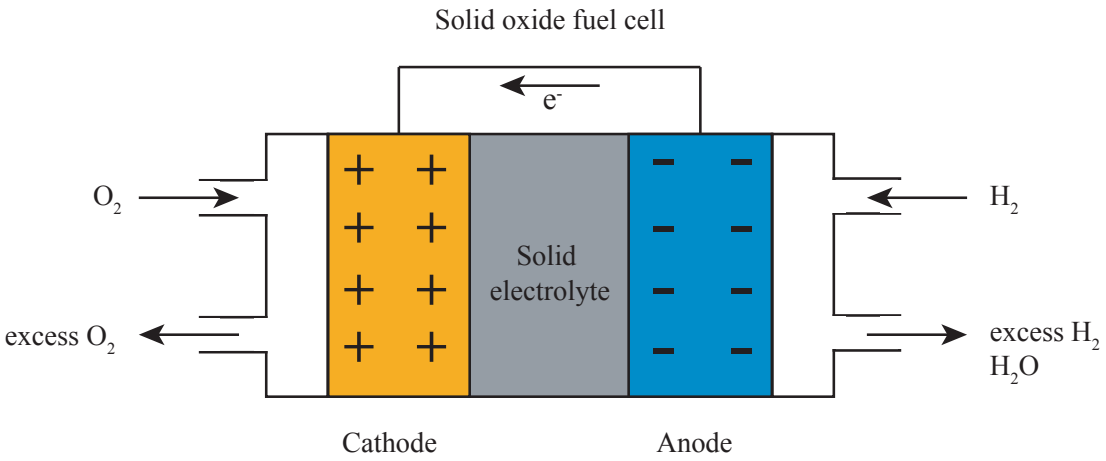

Figure 1.1: Solid oxide fuel cell schematic showing fuel input and products output and the flow of electrons through the system

In a typical fuel cell, the hydrogen combustion reaction is split into two electrochemical half reactions, half one reaction occurs at the anode,

$$\mathrm{H_2} \rightleftharpoons 2\,\mathrm{H^+} + 2\,\mathrm{e^-}, \tag{1.1}$$

and the other half reaction occurs at the cathode,

$$\frac{1}{2}\,\mathrm{O_2} + 2\,\mathrm{H^+} + 2\,\mathrm{e^-} \rightleftharpoons \mathrm{H_2O}, \tag{1.2}$$

with the electrolyte acting to spatially separate these two reactions.[14] The electrons transferred from the fuel (in this example H_2) are forced to flow through an external circuit to complete the reaction.[1] Air is supplied to the cathode and fuel is supplied to the anode. H_2 is oxidised at the anode, releasing electrons. The electrons then pass through a wire to the cathode, creating an electric current, where they reduce the oxygen at the electrode/electrolyte interface. Fuel cells are clean and efficient energy devices because the only byproduct of the reaction is water.[13]

There are five major fuel cell types based on the same underlying electrochemical principles, listed in table 1.1. They each offer advantages and disadvantages due to the variety in operating temperature, materials, fuel tolerance and performance.

Polymer electrolyte membrane fuel cells are currently one of the most commonly used fuel cell technologies due to their low operating temperature, however they require expensive

Fuel cell	**PEMFC**[15,16]	**PAFC**[17,18]	**AFC**[19,20]	**MCFC**[21,22]	**SOFC**[23,24]
Electrolyte	Polymer membrane	Liquid H_3PO_4 (immobilised)	Liquid KOH (immobilised)	Molten carbonate	Ceramic
Charge carrier	H^+	H^+	OH^-	$CO_3{}^{2-}$	O^{2-}
Operating temperature	80 °C	200 °C	60 °C - 220 °C	650 °C	600 °C- 1000 °C
Catalyst	Platinum	Platinum	Platinum	Nickel	Perovskites
Cell components	Carbon based	Carbon based	Carbon based	Stainless based	Ceramic based
Fuel compatibility	H_2, methanol	H_2	H_2	H_2, CH_4	H_2, CH_4, CO_2

Table 1.1: Description of the major fuel cell types.[1]

catalysts and highly pure fuel.[13,25] Due to the disadvantages with polymer electrolyte membrane fuel cells,[16] there is substantial research into alternatives such as solid oxide fuel cells.[26] Solid oxide fuel cells are one of the most promising fuel cell technologies because of several features,[27] including low cost, low air pollution, tolerance to impurities in fuel, relatively high fuel conversion and fewer problems with electrode corrosion and maintenance compared to other fuel cell technologies.[28] There are, however, some concerns regarding solid oxide fuel cells, due to performance degradation with time. This is commonly associated with the fuel cell materials[29] exhibiting instability in the complex operating environment, including the exposure to high operating temperatures.[30] It is therefore important to work towards creating intermediate temperature solid oxide fuel cells to mitigate the device degradation and enhance performance. The improvement of solid oxide fuel cell performance can be achieved not only by investigating the use of new materials[31–33] in solid oxide fuel cells, but also by obtaining a more complete understanding of the chemistry of pre-existing materials such as stabilized zirconia, doped bismuth oxide, doped lanthanum gallate and doped ceria,[13] with an aim to decrease the required operating temperature and thus increase fuel cell lifetimes.[34]

1.1.2 Solid Electrolytes in All–Solid State Li-Ion Batteries

Like a fuel cell, a battery is a device in which chemical energy is converted into electricity. Historically, the term 'battery' was used to describe a system composed of multiples cells, however the usage has evolved to include single cell devices.[35] A battery cell is comprised

of positive and negative electrodes separated by an electrolyte and connected through an external circuit.[36–38] Batteries differ from fuel cells as batteries store energy, and once depleted must be discarded or recharged, whereas a fuel cell continuously produces electricity while fuel and oxygen are supplied.[38] In any battery, the materials used for the anode and cathode determine the voltage and capacity of the battery and the electrolyte determines the operating boundaries for these materials.[39] Together these materials determine the prospective properties of the battery. In a conventional lithium-ion battery, the typical anode material is graphite and until recently the usual cathode material was lithium cobalt oxide $LiCoO_2$,[40] with a liquid-organic lithium salt electrolyte.

In a typical lithium-ion battery, the cell chemistry depends on an intercalation mechanism, which involves the insertion of lithium ions into the crystalline lattice of each of the electrodes.[41] The reaction is split into two electrochemical half reactions, the cathode half reaction,

$$\mathrm{LiCoO_2} \rightleftharpoons \mathrm{Li_{(1-x)}CoO_2} + x\,\mathrm{Li^+} + x\mathrm{e^-}, \tag{1.3}$$

and the anode half reaction,

$$x\,\mathrm{Li^+} + x\mathrm{e^-} + 6\,\mathrm{C} \rightleftharpoons \mathrm{Li}_x\mathrm{C}_6. \tag{1.4}$$

During charging, an oxidation reaction at the cathode releases electrons to the negative terminal and ions into the electrolyte. The electrons are forced through the external circuit to the anode and the ions pass through the electrolyte to complete the reaction at the anode.[42] During discharging, this process is reversed. This creates a flow of current converting the chemical energy to electricity.[43]

The term battery was first used in 1749 by Benjamin Franklin to describe a set of linked capacitors that were charged with a static generator and discharged by touching metal to their electrode.[44] This instigated a continuous development of batteries leading to those used today. Lithium-ion batteries have become one of the most prominent technologies in human history since their commercialisation in the early 1990s.[45] Compared to other commonly used batteries, such as lead acid, nickel-cadmium, nickel-zinc and nickel-metal hydride batteries, lithium-ion batteries demonstrate advantages such as high energy density and a long cycle life. Conventional lithium-ion batteries, however, suffer from critical safety issues due to the organic liquid electrolytes which are highly flammable and can lead

to battery fires and explosions.[46] One proposed solution is to replace these conventional liquid electrolytes with solid electrolytes to form all–solid-state lithium-ion batteries. Such solid-state batteries in principle offer high thermal stabilities and improved safety, high voltage, high energy density and a low self discharge rate.[47]

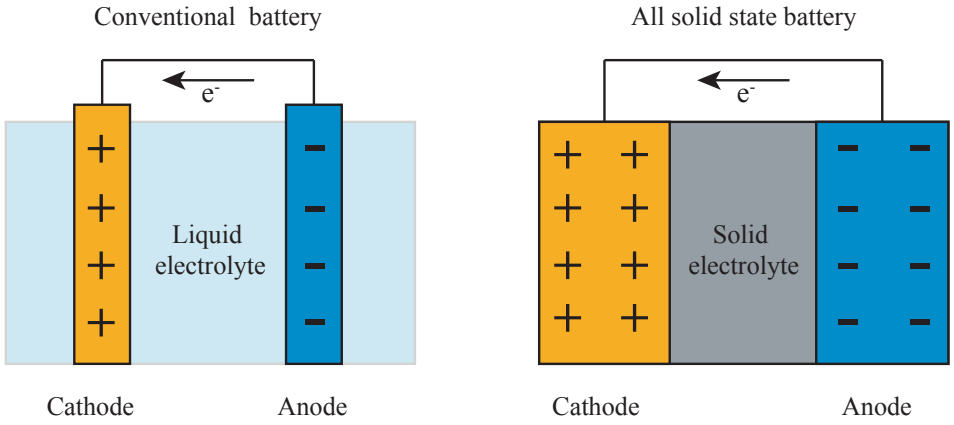

Figure 1.2: Conventional and solid state battery schematics, showing the difference in electrolyte.

The working principles are the same for conventional lithium ion batteries and all–solid-state batteries. During charging lithium ions deintercalate from the cathode and move through the electrolyte into the anode through an external circuit. During discharging movement of the lithium ions is reversed.[48] To be commercially viable, battery electrolytes must meet a number of requirements, including exhibiting an ionic conductivity above 1×10^{-4} S cm^{-1} at room temperature with negligible electronic conductivity and exhibiting a wide electrochemical stability window.[49] No existing Li-ion solid electrolytes meet all of the criteria, however there are several solid materials that have the potential to act as as solid electrolytes for all–solid-state batteries, including sodium super ionic conductors (NASICON),[50–52] lithium super ionic conductors (LISICON),[53–55] lithium phosphorus oxynitride (LiPON),[56,57] garnets,[58–60] perovskites,[61,62] and anti-perovskites.[48] In the future, conventional batteries may be replaced by solid electrolyte batteries in a wide range of applications ranging from microelectronics to aerospace.[63]

1.2 Challenges

As discussed, solid electrolytes offer advantages over traditional liquid electrolytes due to high ionic conductivities while offering improved safety, low cost and fewer problems with device maintenance. There are, however, fundamental challenges which need to be

addressed to make the use of solid electrolytes in electrochemical devices commercially viable. The upmost of these challenges is to produce solid electrolytes which exhibit high ionic conductivities at ambient temperatures. In order to achieve this, it is required that the chemistry and ionic conductivity mechanisms within crystalline solid electrolytes are better understood.

1.2.1 Defects, Grain Boundaries and Space Charge Formation

Ionic conductivity in solid electrolytes depends on the crystalline structure at the microscopic level.[64] The arrangement of atoms within the crystal lattice determines the local potential energy profiles for diffusion,[65] as ionic transport in crystalline solids usually occurs by ions hopping from one atomic site in the crystal lattice to another.[66,67] To exhibit an ionic conductivity, ions must be free to diffuse and move through the solid and therefore it is necessary to have partial occupancy or energetically equivalent of near-equivalent sites.[4]Ionic diffusion in solids is usually possible because of point defects, such as vacancies,[68] existing in the crystal structure and the formation of pathways for ionic transport.

In perfect crystals, translational symmetry requires that defect concentrations and mobilities are uniform throughout the system.[69] In real solid electrolytes, however, translational symmetry is broken by the presence of surfaces and grain boundaries.[70] Grain boundaries exist at the interface between grains of the same structure and composition, but differing orientation.[71] This inhomogeneity can result in local defect concentrations and defect mobilities deviating from their bulk values through the formation of "space-charge regions".[72–74] Because the standard chemical potentials of point defects at grain boundaries can differ from bulk values, these defects will be accumulated or depleted at the grain boundary core. The grain boundary core is not well defined throughout the literature. In some studies the grain boundary core is a single atomic spacing at the center of the grain boundary, in other studies (including this thesis) the grain boundary core is the region where the variation in chemical potential, and thus the defect segregation, is greatest. If these defects are charged (as in the case of a solid electrolyte) this accumulation / depletion produces a net local charge, and electrostatic interaction dictates that the defects in the adjacent regions will also redistribute, forming space-charge regions where there is a local depletion or accumulation of charge carriers relative to the charge at the grain boundary core.[75–77] Ionic conductivities depend on charge carrier concentrations and so space-charge formation can strongly affect local ionic conductivities, and, in turn, affect

macroscopic conductivities in polycrystalline solid electrolytes.[78,79]

The formation of space-charge regions in crystalline solid electrolytes has been extensively studied due to the potentially large impact on the ionic conductivity of the material. A range of computational techniques can be implemented to better understand space charge formation and properties in solid electrolytes. The most common of which includes the implementation of a 1D continuum Poisson-Boltzmann model[80–83] to minimise the free energy of the system directly. This leads to a computationally cheap and conceptually simple model, which can self-consistently describe the space charge properties at electrochemical equilibrium. Alternatively, atomistic modelling can be used to analyse the space charge properties in solid electrolytes. Atomistic molecular dynamics or Monte Carlo techniques are used to examine the relationship between the crystal structure, defect distributions and ionic conductivities.[84–87] Atomistic techniques give a complete description of the time-average positions in 3D space, however are computationally expensive and conceptually complex.

The concepts introduced briefly in this chapter are expanded throughout the thesis. Defect species and diffusion, grain boundaries and space charge formation are discussed in more detail in chapter 2 and the Poisson-Boltzmann and atomistic computational models are discussed in more detail in chapter 4.

1.3 Overview of Thesis

The objective for this work, and the focus of this thesis is to bridge atomistic and continuum space charge models in order to create a robust, more physically accurate space charge model. The aim of which is to provide a better understanding of space charge formation and properties to assist in the design of materials for use in solid-state electrochemical devices. In this thesis, the theory of ionic diffusion (chapter 2) and historical space charge models (chapter 3) are discussed, and implementation of an integrated atomistic and continuum model is presented in chapter 4 onward. This integrated atomistic-continuum model has been developed into published open source software (PYSCSES).[88]

PYSCSES is a Poisson-Boltzmann space charge model which takes explicit defect positions and defect segregation energies obtained through atomistic classical or first principles simulations and solves the Poisson-Boltzmann equation using a second order finite difference approximation. This gives spatially resolved electrostatic potential, charge density and defect distribution profiles from the grain boundary into the bulk. The defect distribu-

tions produced allow the calculation of effective parallel and perpendicular grain boundary resistivities and activation energies. The model also allows variation in atomic structure and 'operating' conditions to enable the exploration of the space charge properties for a wide range of cases. The mathematical models implemented are discussed further in chapter 4

In chapter 5, the space charge properties calculated using PYSCSES are compared to historical and commonly used space charge models to investigate the impact of including the explicit crystalline structure of the solid electrolyte in determining it's space charge properties. Common approximations such as the mobility of defects within the structure (Mott-Schottky and Gouy-Chapman approximations) have been investigated, along with determining whether including the charge of the non-defective species in the model has an effect.

In chapter 6, the space charge properties of a well known and well documented solid oxide fuel cell structure $Gd-CeO_2$, where space charge formation has been extensively studied is modelled and explored, and in chapter 8 a relatively novel potential solid electrolyte for use in solid state lithium ion batteries, the anti-perovskite Li_3OCl, where space charge formation has not previously been considered is modelled and explored. In chapter 7 the effect of the proximity of grain boundaries to one another (effectively nanoionic systems) is modelled in order to see how the explicit structure affects well known conceptual properties.

Generally, throughout the various test cases, it has found that inclusion of the explicit lattice structure in Poisson-Boltzmann space charge modelling is of importance.

Chapter 2

Theory of Diffusion in Solids

2.1 Crystal Lattice Structure

Solids are characterised by incompressibility, rigidity and mechanical strength.[89] Solids can be amorphous, whereby the arrangement of atoms is randomly structured or crystalline[90] whereby the arrangement of atoms is orderly structured. This ordered structure can be considered in the long range, in that, the crystal structure can be considered as the repetition of a unit cell in three dimensions.[91]

2.1.1 Unit Cells

The unit cell of a crystal is defined as the smallest repeating unit that has the full symmetry of the crystal structure.[92] The geometry of the unit cell is defined by the cell edges (*a, b, c*) and the angles between the cell edges (α, β, γ).[93] The position of atoms are defined in terms of fractional coordinates (x_i, y_i, z_i) along the cell edges measured from the origin.[94]

2.1.2 Crystal Systems

In crystallography, the crystal structure is defined by defining lattice points within the lattice system and then attaching atoms (the basis) to these lattice points. Crystal structures can be classified into seven crystal systems,[95] detailed in table 2.1. These crystal systems are sets of reference axes which have direction and cell length and cell angle equalities and inequalities.

The Bravais lattice are the distinct lattice types which when repeated can define the crystalline arrangement. These can be any of 14 possible three-dimensional configurations as shown in figure 2.1.

Crystal System	Axial Relationships
Cubic	$a = b = c$, $\alpha = \beta = \gamma = 90°$
Tetragonal	$a = b \neq c$, $\alpha = \beta = \gamma = 90°$
Orthorhombic	$a \neq b \neq c$, $\alpha = \beta = \gamma = 90°$
Monoclinic	$a \neq b \neq c$, $\alpha = 90°\beta \neq 90°\gamma = 90°$
Triclinic	$a \neq b \neq c$, $\alpha \neq 90°\beta \neq 90°\gamma \neq 90°$
Hexagonal	$a = b \neq c$, $\alpha = \beta = 90°\gamma = 120°$
Trigonal	$a = b = c$, $\alpha = \beta = \gamma$
Rhombohedral	$a' = b' = c'$, (hexagonal axes), $\alpha' = \beta' = 90°\gamma' = 120°$

Table 2.1: Seven categories of crystal system.[2]

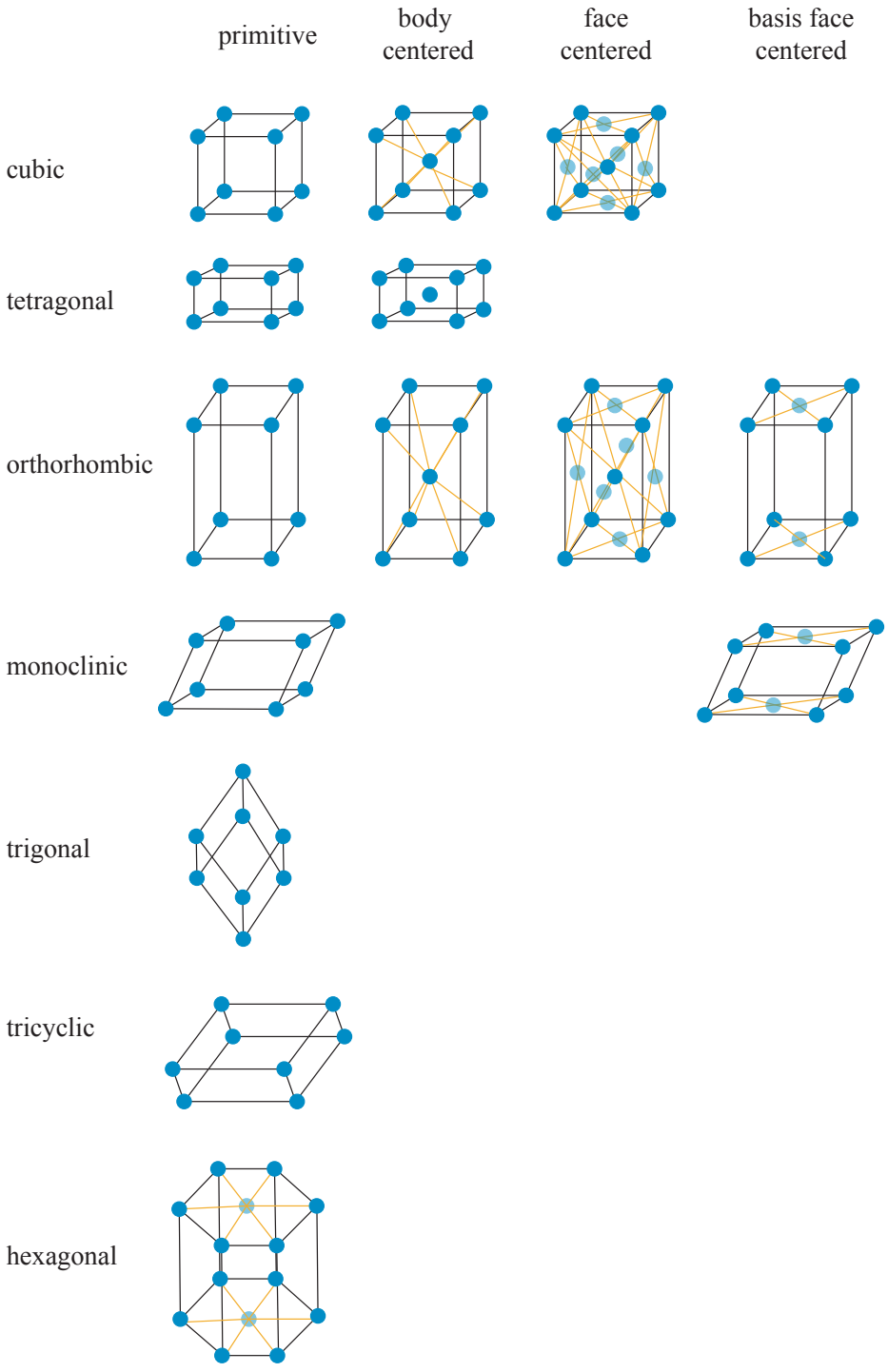

Figure 2.1: The 14 Bravais lattices of crystalline lattice structure.

2.1.3 Irregularities in the Crystal Structure

Real crystals are not perfectly periodic, but feature irregularities in the ideal arrangement as described above. Crystal irregularities include, the local modifications of the crystalline arrangement of atoms, called defects, which facilitate the movement of atoms through the body of the of the crystal.[96] Defects exist in crystal lattices because their presence up to a certain concentration leads to a reduction in the free energy. The creation of a single defect requires a certain amount of energy, ΔH, but offers a considerable increase in entropy, ΔS, because of the number of configurations in which a single defect can occupy a single site.

This leads to an increase in configurational entropy, given by the Boltzmann formula,

$$S = k \ln W, \tag{2.1}$$

where W is the number of microstates (arrangements) in the macrostate. This increase in entropy offsets the enthalpy required to form the defect and due to the relationship,

$$\Delta G = \Delta H - T\Delta S, \tag{2.2}$$

the total free energy of the system decreases. Once the defect concentration is increased, the energy required to form a defect becomes larger and the entropy gain becomes smaller due to the disordered nature of the crystal lattice. In real materials, a free energy minimum exists where the number of defects in the system is in thermodynamic equilibrium, shown in figure 2.2.[92]

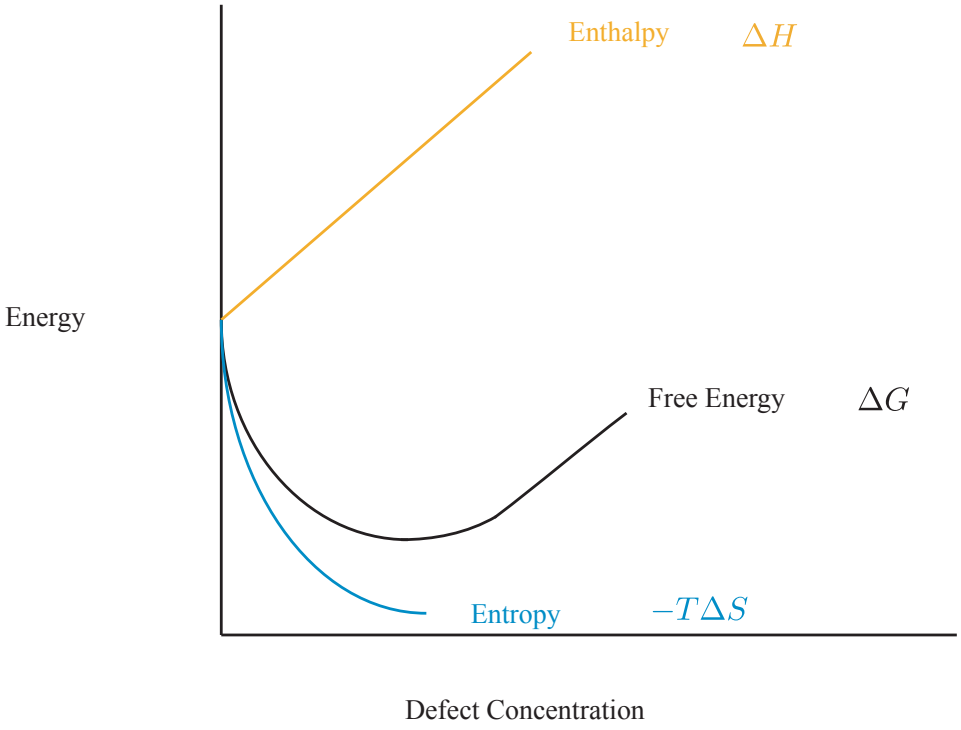

Figure 2.2: Energy change on introducing defects into a perfect crystal.

Alternatively, the irregularity of real crystals include structural modifications, such as the presence of interfaces, which can affect local chemical potentials. These irregularities critically determine many of the electrical and mechanical properties of crystalline materials.[97,98]

2.2 Defects

2.2.1 Point defects

Stoichiometric crystal structures are often disrupted by the presence of point defects. In the stoichiometric crystal, all sites are occupied by an ion, but these ions can be displaced. In the case that an ion is removed from its site, a vacancy is formed in the crystal structure. Vacancies are simply unoccupied lattice sites (figure 2.3(a)). Ions can also occupy regions of space between the explicit crystalline sites, known as interstitial sites. When the interstitial ions are of the same chemical species as the host lattice, they are termed 'self-interstitials'(figure 2.3(b)).[99,100] Defects may also be formed by the inclusion of foreign ions in the crystal structure. These foreign ions are a different chemical species from the host crystal and may be substitutional (where they replace a

host ion)(figure 2.3(e)) or interstitial (where they occupy the otherwise empty interstices of the host lattice - figure 2.3(c)), discussed in more detail in section 2.2.3. The final common point defect is known as an anti-site defect whereby ions are present on the wrong sublattice(figure 2.3(d)), for example V atoms on the Ga sublattice in V_2Ga_5.[96] The defect species focused on throughout this thesis are vacancies and interstitial defects, which often occur in the crystal structure as defect pairs.

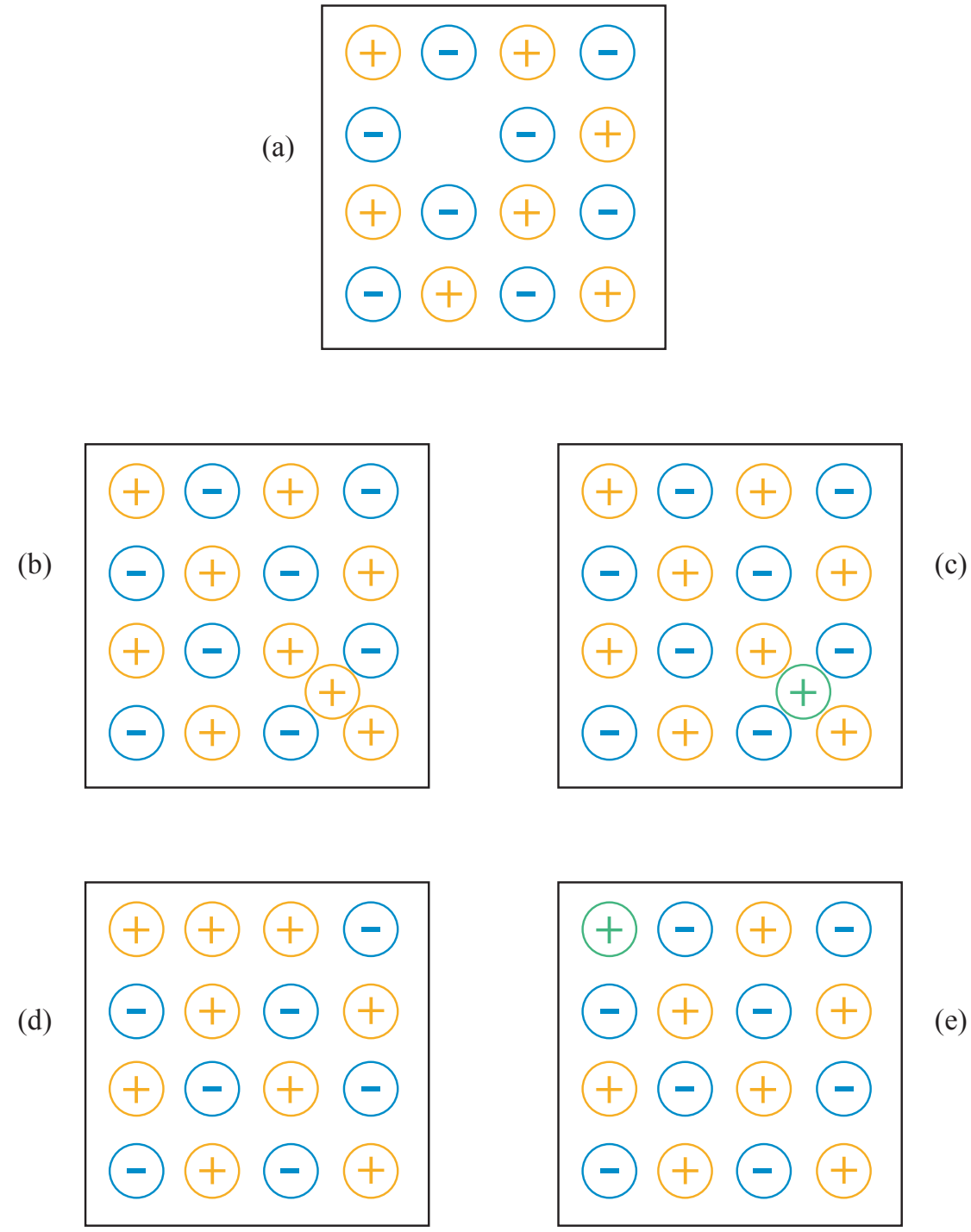

Figure 2.3: Schematic depicting the most common types of point defects that can exist in crystalline structures. (a): vacancy, (b): self-interstitial, (c): interstitial, (d): substitutional, (e): anti-site.

2.2.2 Defect pairs

Because of the large number of possible defects that can be present in even simple crystals, a full thermodynamic analysis of all possible defect species can quickly become quite

complex.[101] Often, however, a small number of defect species dominate, and can be considered in isolation. A further conceptual simplification is possible by noting that defect formation must obey mass balance (the total number of each atomic species is constant) and the resulting defective system must still exhibit net charge neutrality. These two factors mean that defect chemistry can often be considered in terms of charge neutral defect pairs.[102,103]

Schottky defect pairs are formed when charge neutral combinations of ions are removed from their sites. The stoichiometric removal of ions maintains charge neutrality throughout the crystal.[104]

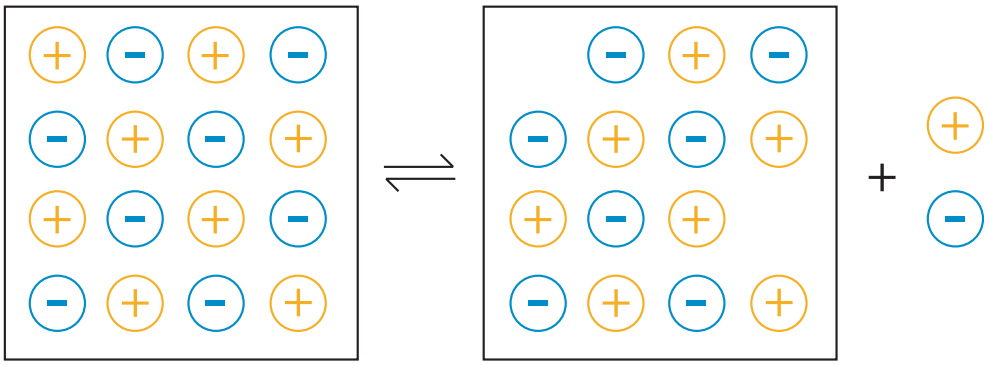

Figure 2.4: Schematic of a typical Schottky defect pair forming in a solid electrolyte

For example, the formation of Schottky defects in MgO:

$$\mathrm{Mg}_{\mathrm{Mg}}^{\times} + \mathrm{O}_{\mathrm{O}}^{\times} \rightleftharpoons V''_{\mathrm{Mg}} + V_{\mathrm{O}}^{\bullet\bullet} + \mathrm{Mg}_{\mathrm{surface}} + \mathrm{O}_{\mathrm{surface}}. \tag{2.3}$$

Frenkel defect pairs are formed when an ion is displaced from its lattice site and is relocated on an interstital site, forming a vacancy and an interstitial.[105]

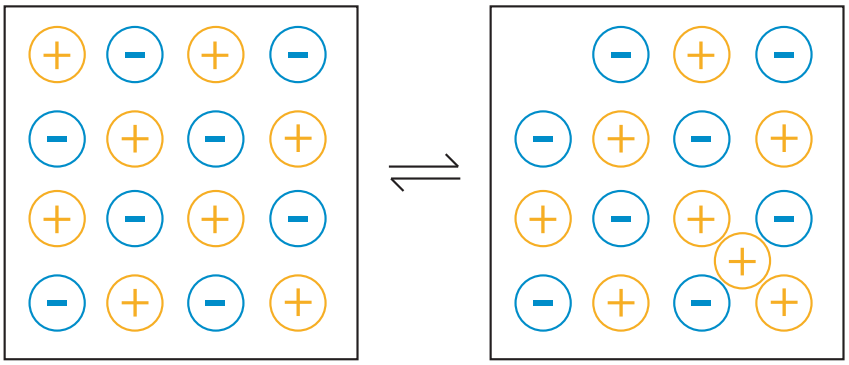

Figure 2.5: Schematic of a typical Frenkel defect pair forming in a solid electrolyte

For example, the formation of oxygen Frenkel pairs in MgO:

$$\mathrm{O}_{\mathrm{O}}^{\times} \rightleftharpoons \mathrm{O}_{\mathrm{i}}'' + V_{\mathrm{O}}^{\bullet\bullet}. \tag{2.4}$$

2.2.3 Extrinsic defects

The properties of a crystalline material can be altered by doping the system with extrinsic ions.[106] Dopant ions can be isovalent,[107,108] whereby the dopant ion has the same charge as the ion it is substituting, or aliovalent, whereby the dopant ion has a difference charge to the ion it is substituting. Defect concentrations can be increased in solid electrolytes by aliovalently doping the system. Aliovalent dopant ions are charge compensated to maintain charge neutrality throughout the system.[109]

There are four fundamental ionic mechanisms for achieving charge balance through defect formation in solid electrolytes.[110] Doping with a higher valent cation leads to the creation of either cation vacancies or anion interstitials and doping with lower valent cations leads to the formation of either cation interstitials or anion vacancies. Alternatively, other possible charge compensation mechanisms include electronic compensation, whereby the charge is compensated by a change in the number of electrons or holes in the system, or by the formation of anti-sites.[96] In figure 2.6, neutral M is added to the structure, which takes on a net +2 charge + 2 e^-. The electrons could exist in the conduction band (as with superconductors), but in a wide-gap material, it is more favourable to form a charge compensating "acceptor" (supervalent extrinsic defect is called a "donor" because it donates excess electrons) defect.

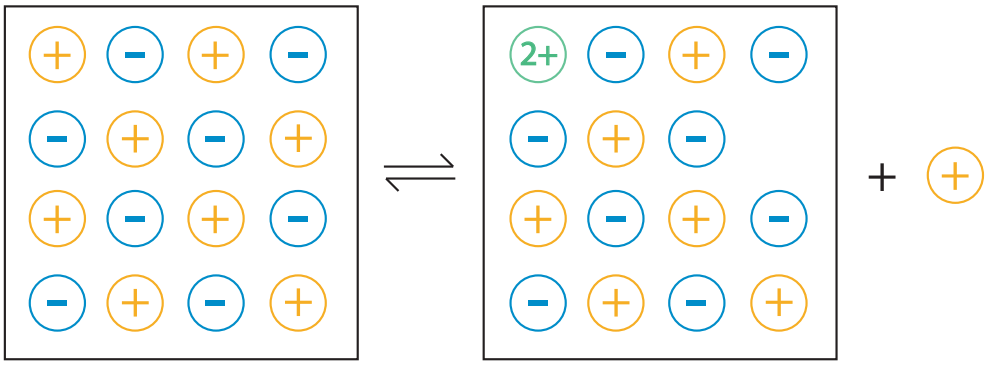

Figure 2.6: The formation of a vacancy due to aliovalently doping with an extrinsic ion.

In wide-gap metal oxides, this charge compensation often occurs through the generation of oxygen vacancies in the solid structure. For example, the formation of defects due to doping in Gd doped CeO_2[111] (while this shows an individual aliovalent doping reaction, typical doping concentrations are as high as 20 %),

$$2\,Ce_{Ce}^{\times} + 4\,O_{O}^{\times} + 2\,Gd \rightleftharpoons 2\,Gd_{Ce}' + 3\,O_{O}^{\times} + V_{O}^{\bullet\bullet} + 2\,Ce. \tag{2.5}$$

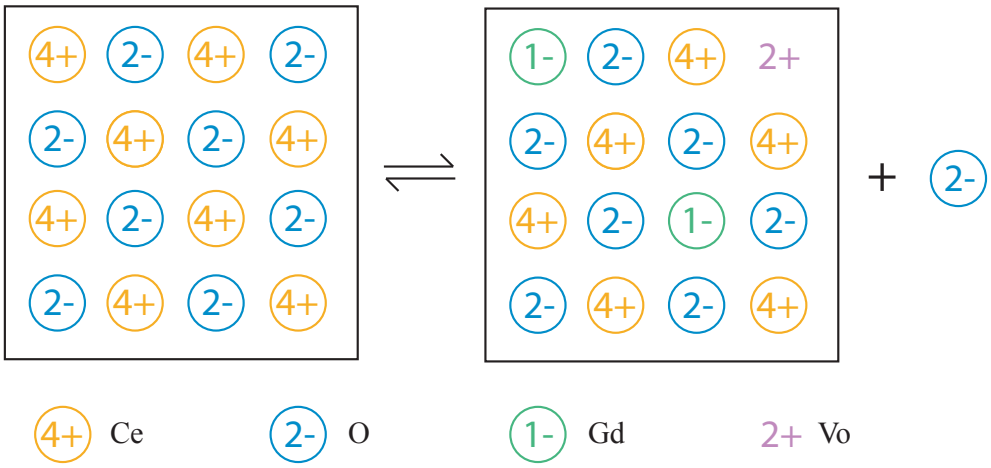

Figure 2.7: Schematic of a typical defect pair forming in Gd−CeO_2 due to aliovalent doping

2.3 Defect Transport

2.3.1 Theory of Defect Transport

The process of migration of atoms through solid is a fundamental part of solid-state chemistry. The standard model for diffusion in crystalline solids considers ionic transport as a sequence of "hops" between well-defined lattice sites, allowing atoms to move through inter-connected diffusion channels in the crystal structure framework.[112–115] Within this model, diffusion is only possible because of the existence of point defects, since these provide vacant sites to facilitate ion hops. In interstitial lattice diffusion, particles migrate from interstitial site, (empty space between lattice sites), to interstitial site (figure 2.8(a)). In vacancy lattice diffusion, particles migrate through the point vacancy sites (figure 2.8(b)).[116]

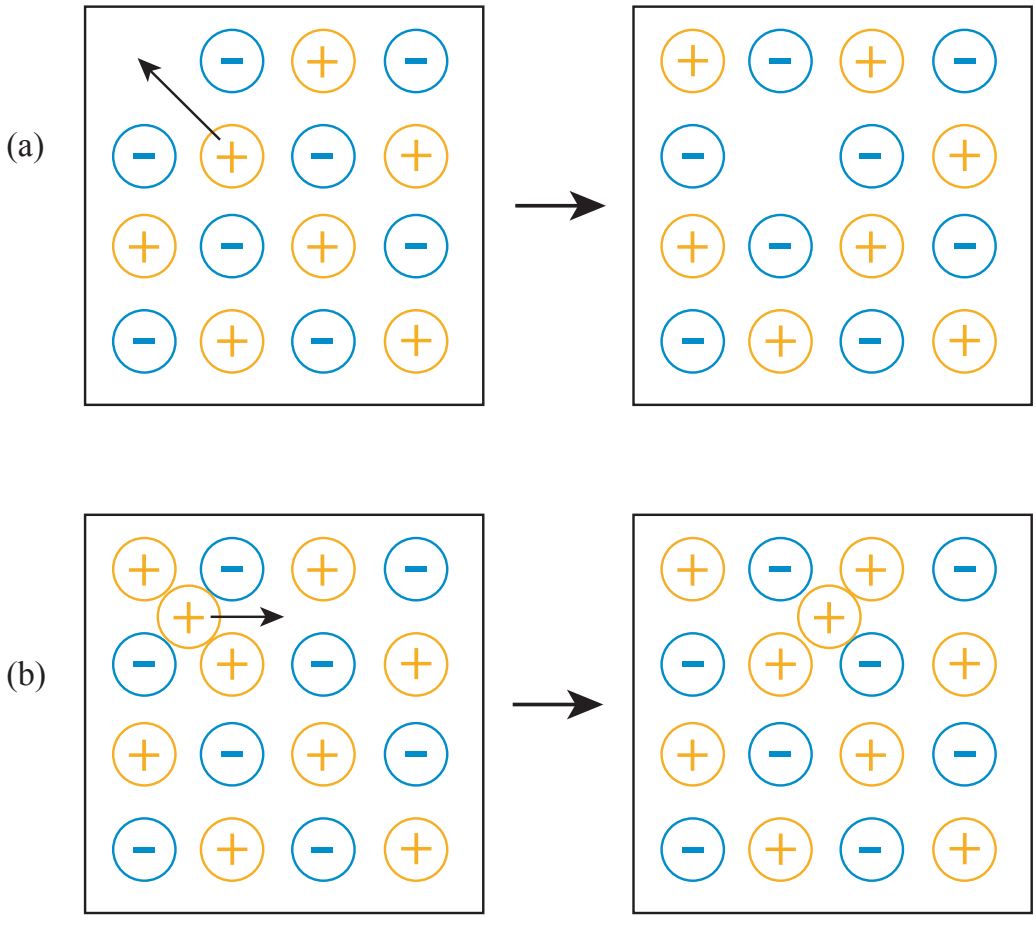

Figure 2.8: Schematic of a typical vacancy diffusion mechanism (a), and a typical interstitial diffusion mechanism (b)

Solid electrolytes can be considered in terms of 'fixed' ions that vibrate on their crystal-

lographic sites, defining diffusion pathways, and 'mobile' ions that can move through the diffusion pathways.[117] Diffusion paths in solid electrolytes are dependent on crystalline structure, and play a crucial role in the definition of macroscopic transport coefficients of the solid electrolyte, such as diffusion coefficient and ionic conductivity.[58] Particle diffusion in solid electrolytes may be described in terms of these sequential discrete hops when a number of criteria are met[118]

1. The hop time (τ_h) compared with the time in a site (τ_R) must be such that $\tau_h \gg \tau_R$.
2. The mean thermal vibration frequency of particles between hops (ν) must be such that $\tau_R \gg \nu$.
3. The distance over which a particle travels during a hop (d) must be greater than the amplitude of the thermal motion (a), $d \gg a$.
4. The maximum change in the potential energy due to particle rearrangement (ΔE) must be greater than the thermal energy, $\Delta E \gg kT$.

If these conditions are met, and the hops are independent (if the particles are considered as non-interacting) then the tracer diffusion coefficient can be approximated as,

$$D^* = \frac{1}{6} a^2 \tilde{\nu}, \tag{2.6}$$

where $\tilde{\nu}$ is the average hop rate per atom. The ionic conductivity can be given by,

$$\sigma = \frac{cz^2}{kT} \frac{1}{6} a^2 \tilde{\nu}, \tag{2.7}$$

where c and z are the mobile charge carrier concentration and charge respectively. These relationships can be combined to relate D^* and σ in the Nernst-Einstein relation,[119,120]

$$\frac{\sigma}{D^*} = \frac{cz^2}{kT}. \tag{2.8}$$

As ionic mobility is defined as,[121]

$$\mu = \frac{D^* z}{kT}, \tag{2.9}$$

the expression for ionic conductivity can be expressed as a product of the mobile charge

carrier concentration, charge and mobility,[122]

$$\sigma = cz\mu \tag{2.10}$$

The work carried out throughout this thesis considers mobile charge carriers to be in the dilute limit. However, it can be noted that in real solid electrolytes inter-particle interactions can be significant and hops cannot be assumed statistically independent. Individual hopping probabilities depend on the positions of nearby atoms, trajectories are correlated, and the system dynamics deviates from random walk behaviour. The diffusion coefficient becomes,[58]

$$D^* = \frac{1}{6}a^2\tilde{\nu}f, \tag{2.11}$$

where f is a single particle correlation factor that accounts for the deviations from random walk behaviour. This factor has its origin in the correlation in directions between successive atomic jumps of the tracer as induced by a defect. Correlations between hops made by different ions then modify the ionic conductivity, which becomes

$$\sigma = \frac{cz^2}{kT}\frac{1}{6}a^2\tilde{\nu}f_I, \tag{2.12}$$

where f_I is the collective or "physical" correlation factor (the correlation factor for conductivity, compared to f: the correlation factor for isotope diffusion). The combined relationship deviates from Nernst-Einstein behaviour to become,

$$\frac{\sigma}{D^*} = \frac{cz^2}{kT}\frac{f_I}{f}. \tag{2.13}$$

2.3.2 Defect Pair Contributions

Schottky defect pairs lead to vacancy migration, where sites that would be occupied in a non-defective structure are unoccupied and an ion adjacent to the vacancy can hop into it, leaving its own site vacant. Frenkel defect pairs can lead to both interstitial migration and vacancy migration.[123] In the dilute limit, the concentration of defects in a system is proportional to the ionic conductivity.[124] The presence of defects can be increased by increasing the operating temperature of the system, or by aliovalenty doping of the system

and forcing the creation of defects through the requirement of charge neutrality.[125]

2.4 Grain Boundaries and Surfaces

In perfect crystals, translational symmetry requires that defect concentrations and mobilities are uniform throughout the system. Solid electrolytes, however, are often polycrystalline with distinct crystallographic regions separated by grain boundaries,[126] where two bulk crystalline grains meet. These two grains differ in mutual orientations and the grain boundary is a structurally distorted transition region, where the atoms are shifted from their regular positions compared to the crystal interior. These inhomogeneities can result in local defect concentrations and mobilities deviating from their bulk values.[127,128] Due to the relationship between ionic conductivity and mobile charge carrier concentration these deviations can have a large effect on the ionic conductivity of the solid electrolyte.[129] Due to mobile charge carriers segregating to the grain boundary core, often low local conductivity dominates for perpendicular ionic conduction and high local conductivity dominates for parallel ionic conduction.[96]

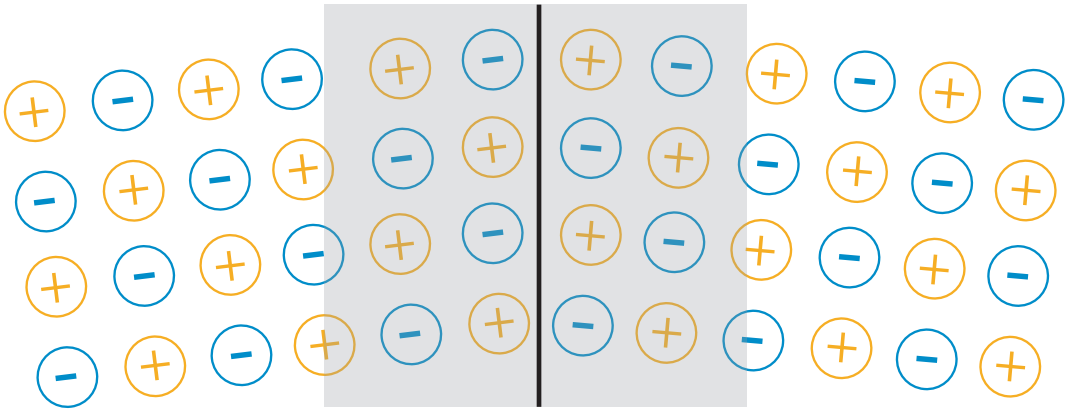

Figure 2.9: An example grain boundary which may be present in solid electrolytes, depicting the structural distortion in the grain boundary region.

Grain boundaries are homo-interfaces, however, hetero-interfaces can also exist between different materials, for example in BaF_2 – CaF_2 heterostructures. These heterostructures consist of alternating layers of BaF_2 and CaF_2. The interfaces between the layers of BaF_2 and CaF_2 exhibit increased conductivity in the direction parallel to the interface, with experimental data showing that the heterostructure has a higher ionic conductivity than either of the bulk materials.[130] Through extensive literature it has been shown that the presence of grain boundaries and interfaces between crystalline regions has a significant

effect on the ionic conductivity of the material and this is commonly attributed to the formation of space charge regions.

2.4.1 Grain boundary structure

The orientation of the surface of a crystalline structure is defined by the termination. Cleavage of a bulk crystal at different planes will result in different surface terminations. These surface terminations are described using Miller indices,[2,131,132] which identify the orientation of a surface. To define the Miller index of a surface, the fractional coordinates where the plane cuts the x, y and z axes of the unit cell are taken. The reciprocal of these fractional coordinates are the Miller indices (h, k, l) in the x, y and z direction respectively.

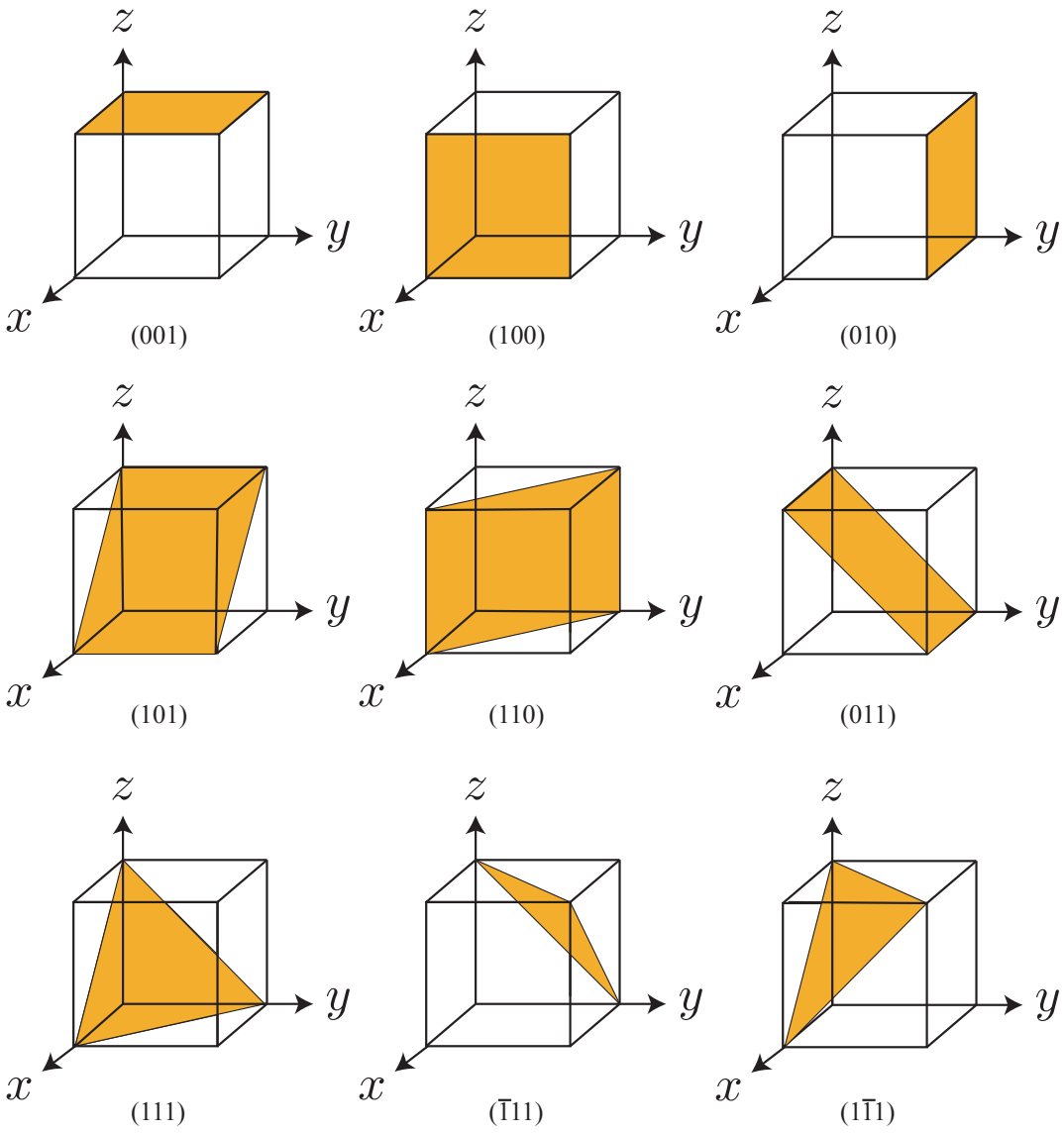

Figure 2.10: Schematic of the Miller indices for the different cleavage planes in a cubic structure.

Grain boundaries are commonly treated by considering the surface orientation of each of the grains. Grain boundary atomic structure strongly depends on the macroscopic degrees of freedom in the form of mutual misorientation, including the rotational axis o, the rotational angle θ and the orientation normal to the grain boundary plane n, and the microscopic degrees of freedom regarding the translational states of the two different crystals. Depending on the type of rotation angle, the grain boundary can be of tilt or twist type. In the tilt boundary,[133] the rotation axis is parallel to the boundary plane and in the twist boundary[134] the rotation occurs around an axis perpendicular to the boundary plane.[135] Depending on the mirror image plane of tilt grain boundaries, the

grain boundary can symmetrical or asymmetrical.[136] A symmetrical[137] grain boundary is found when the grain boundary plane represents the mirror image plane, and the grain boundary is described using the same Miller indices from both adjoining grains. The combination of these degrees of freedom leads to four categories of grain boundary.

Grain boundary category	Miller indices	Tilt angle ϕ
Symmetric tilt grain boundary	$h_1k_1l_1 = h_2k_2l_2$	$\phi = 0$
Asymmetric tilt grain boundary	$h_1k_1l_1 \neq h_2k_2l_2$	$\phi = 0$
Twist grain boundary	$h_1k_1l_1 = h_2k_2l_2$	$\phi \neq 0$
Mixed grain boundary	$h_1k_1l_1 \neq h_2k_2l_2$	$\phi \neq 0$

Table 2.2: Four categories of grain boundary, described in terms of degrees of freedom.

According to coincident site lattice theory,[138–140] grain boundaries can be defined by the degree of fit between the two grain boundary planes, Σ, which is given by the reciprocal of the ratio of coincident sites to the total number of sites. A high density of coincidence sites in the boundary plane is geometrically necessary for the formation of a low-energy reference structure.[141] For a symmetric tilt grain boundary, where $h_1k_1l_1 = h_2k_2l_2$, $\Sigma = \delta(h^2 + k^2 + l^2)$.

The full description of a grain boundary is given by the Miller indices (hkl), the rotation axis $[h_ok_ol_o]$, the normal axis to the grain boundary plane, the rotation axis and Σ using the nomenclature,

$$\frac{\Sigma n(hkl)}{[h_ok_ol_o]}\theta \tag{2.14}$$

2.5 Space Charge Formation

2.5.1 Overview of space charge formation

At a crystalline boundary, the local atomic structure often differs significantly from the bulk crystal, which results in mobile ions or defects having different chemical potentials compared to defects in the bulk structure. This variation in standard chemical potential is the defect segregation energy - the change in free energy associated with moving a defect from the bulk to a boundary. Non-zero segregation energies indicate a driving force for mobile defects to spontaneously segregate to, or from, surfaces and boundaries.

In an ionic solid, asymmetric redistribution of charged defects such as vacancies and interstitials, produces local charge regions. The accumulation or depletion of defects at a surface or interface (such as a grain boundary) produces a net local charge. Electrostatic interactions between the charged surface or boundary cause defects in adjacent regions to

also redistribute. This process results in the formation of 'space charge regions'.[72–79] At equilibrium, variations in local chemical potentials are exactly balanced by variations in local electrostatic potentials, giving uniform electrochemical potentials.[142,143]

The thermodynamic origin of space charge formation[144,145] is illustrated schematically in figure 2.11. Figure 2.11 (a), a negative segregation energy causes positively charged defects to segregate to the grain boundary core. Figure 2.11 (b), the concentration of positively charged defects is enhanced at the grain boundary core. Figure 2.11 (c), the grain boundary core now carries a net local positive charge.

Taking into consideration electrostatics and interacting species. Figure 2.11 (d), the repulsion of positively charged defects from the regions adjacent to the grain boundary core. Figure 2.11 (e), the concentration of positively charged defects is depleted in the regions adjacent to the grain boundary core. Figure 2.11 (f), the regions adjacent to the grain boundary core carry a net local charge - the space charge regions.

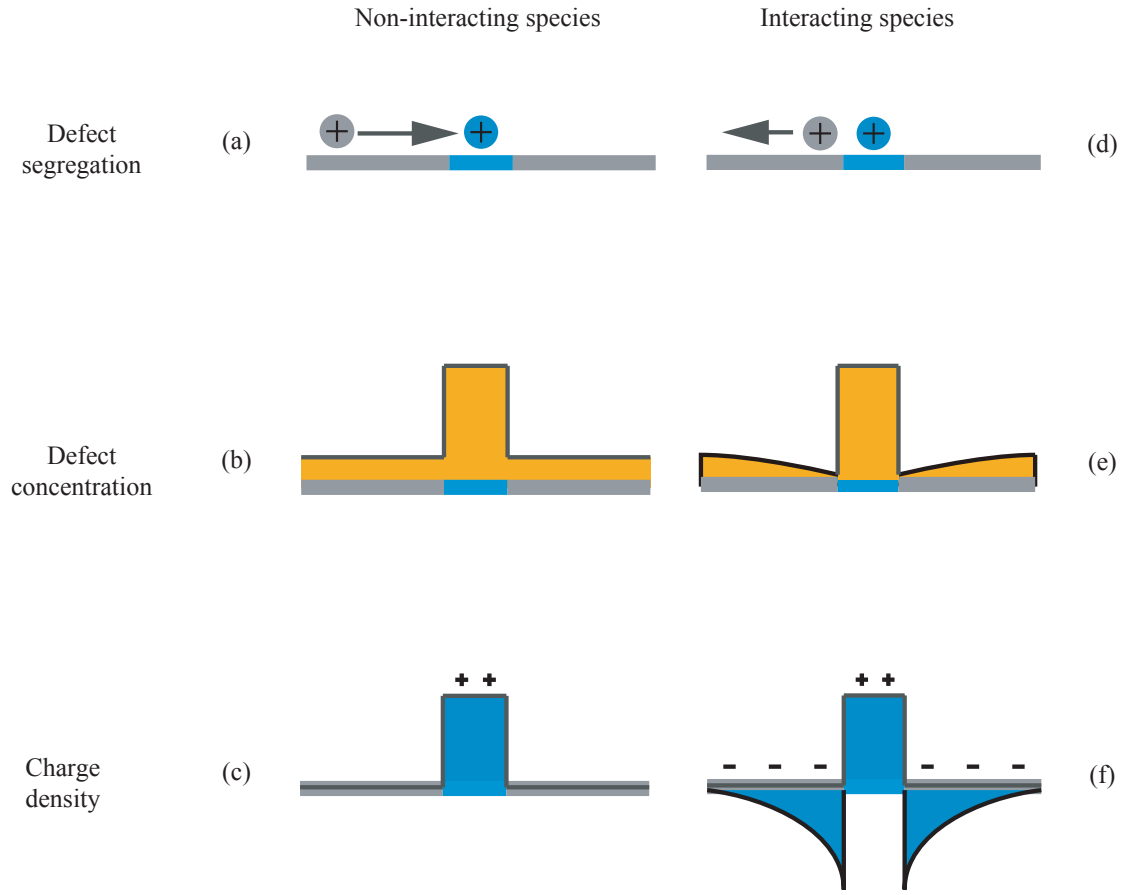

Figure 2.11: Schematic describing the different stages of space charge formation. (a): non-interacting species migrate to the grain boundary core due to favourable segregation energies, (b): the accumulation of defects at the grain boundary core, (c): the grain boundary core develops a net charge. (d): interacting defects are repelled away from the charged grain boundary core, (e): the regions adjacent to the grain boundary core have a depletion of defects, (f): the regions adjacent to the grain boundary carry a net charge.

2.5.2 Thermodynamics of space charge formation

The thermodynamics of defect segregation can be illustrated by considering the defect equilibria for a Frenkel-disordered MX crystal. The two relevant bulk defects are the M vacancy, $V_{\mathrm{M}}{}'$ and the M interstitial, $\mathrm{M}_i{}^*$, and the segregation is to, or away from the surface (s). The formation of a Frenkel pair can be separated into the following two defect equilibria,[146]

$$M_M^{\times} + V_{\mathrm{s}}^{\times} \rightleftharpoons M_{\mathrm{s}}^{\bullet} + V'_M, (\Delta G_{\mathrm{A}}), \tag{2.15}$$

and,

$$M_{\mathrm{s}}^{\bullet} + V_{\mathrm{i}}^{\times} \rightleftharpoons M_{\mathrm{i}}^{\bullet} + V_{\mathrm{s}}^{\times}, (\Delta G_{\mathrm{B}}). \tag{2.16}$$

If the free energy change for equation 2.16 (ΔG_{A}) is greater than the free energy for equation 2.15 (ΔG_{B}), the equilibrium of equation 2.15 will shift to the right. This shift occurs due to M ions being stabilised at the surface, and are therefore enriched at the surface boundary. In compensation, the concentration of vacancies will be increased throughout the crystal. If ΔG_{B} is greater than ΔG_{A}, the concentration of vacancies will be increased at the surface boundary due to surface stabilisation of the vacancies and the concentration of M ions occupying interstitial sites will be increased throughout the crystal.[142,143]

2.6 Space Charge Properties and Grain Boundary Resistivity

Although grain boundary cores are usually only a few interatomic spacings wide, space charge regions are typically much broader. A key question surrounding space-charge formation is the degree to which the space charge extends into the bulk electrolyte. A popular metric for describing the length over which a space-charge distribution decays to bulk defect concentrations is the Debye length, λ, which is the characteristic length scale obtained from the Gouy-Chapman model.[147] The details of the Gouy-Chapman model, and the related Mott-Schottky model, and the derivation of the Debye length are given in chapter 3.

$$\lambda = \sqrt{\frac{\epsilon RT}{2z^2F^2c_\infty}}. \tag{2.17}$$

As the space charge region is a region of depleted or accumulated charge carriers, the relatively broad nature of the space charge region can make significant contributions to macroscopic ionic conductivities. The parallel and perpendicular ionic conductivities of an inhomogenous system, such as a solid electrolyte grain boundary and adjacent space-charge regions, can be expressed as integrals over parallel slices,

$$r^{\parallel} = \frac{1}{\int_0^{L_{\mathrm{x}}} \sigma_{\mathrm{x}} d\mathrm{x}}, \tag{2.18}$$

and

$$r^{\perp} = \int_0^{L_{\mathrm{x}}} \sigma_{\mathrm{x}}^{-1} d\mathrm{x}, \tag{2.19}$$

where σ is the ionic conductivity. The enhancement or depletion of defects in grain boundary space-charge regions will cause a local increase or decrease in ionic conductivity. The net conductivity across or along a grain boundary is therefore different to the bulk. In oxide ion conductors, oxygen vacancies typically segregate to the grain boundary core and become 'trapped' due to the favourability of the site, with an oxygen vacancy depletion in the space charge region. This leads to the material exhibiting a 'grain boundary resistivity'. A full understanding of the role of boundaries in solid electrolytes therefore requires an understanding of spatial variations in crystalline structure, defect behaviour and space charge formation, and is important because of the large effect the irregularities can cause on the macroscopic material properties.

Chapter 3

Standard Space Charge Models

3.1 The Historical Development of Space Charge Theory

The concept of a "space-charge" was described early in the development of theories of liquid electrolytes. In 1853, Helmholtz realised that when a charged electrode was immersed in an electrolytic solution, it would attract oppositely-charged ions and repel like-charges, leading to a region close to the electrode with a net opposite charge.[148] This concept was developed into the double layer model by Gouy in 1910,[149] who suggested that interfacial potential at a charged surface could be attributed to the presence of a number of ions with a given charge at the surface and an equal amount of oppositely charged ions in the solution. The double layer theory was also developed by Chapman in 1913[150] who developed the diffuse double layer theory by observing that capacitance of the electrolyte was not constant and electrostatic potential decayed away from the electrode following a Boltzmann distribution. This became the origin of Poisson-Boltzmann theory, whereby charge carriers were treated as point charges in a continuum dielectric and local point charge concentrations follow Boltzmann statistics, which when combined with Poisson's equation to calculate electrostatic potential, gives the Poisson-Boltzmann equation.

The formation of space-charges in solid electrolytes was first conceptualised by Frenkel in 1946. Frenkel emphasised that regions close to the surface in predominantly Schottky disordered pure crystals experience deviations from bulk stoichiometry and local charge neutrality, due to the difference in standard chemical potentials between anion and cation vacancies. The resulting effect being that the crystal should have a charged surface with an adjacent space charge region.[151] Following this, in 1953 Lehovic stated that the space charge in the surface zone causes an electrostatic potential difference between the bulk and

surface of the crystal and suggested that the difference in the charge carrier concentration between the surface and the bulk should lead to surface ionic conduction. Lehovic also created the first numerical model to calculate the thickness and magnitude of the space charge layer.[152] Lehovic's model formed the basis of numerical space charge theory which was extended into a comprehensive model in 1965 by Kliewer and Koehler. The model included derivation of equations for the local density of charge carriers in the presence of an electrostatic potential, obtained by minimising the free energy of the entire crystal.[153] This approach, which considered only the diffuse space charge region using Boltzmann statistics, was extended by Blakely and Danyluk[154] to include "Fermi-Dirac–like" statistics. This enforced an appropriate description for non-interacting particles occupying a fixed number of sites on a lattice. The model was enforced at the surface as well as including the probability of a site to be occupied by a particular particle using Fermi distribution functions.[154,155]

The first numerical model for defect segregation to grain boundaries was introduced in 1957 by McLean,[156] which subsequently influenced further advancements made by Yan, Cannon and Bower[157] who combined the model of McLean and that of Kliewer and Kohler. The resulting model connected space charge, elastic energy due to size misfit or defects in the matrix, and dipole interactions. In 1984, Maier studied space charge regions in solid two phase systems, such as AgCl with an inert second phase of alumina or silica. Maier used the description of defect distributions described by Kliewer and Koehler, derived from the analytical solution for the non-linear Poisson-Boltzmann equation, combined with the influence of the second inert phase, including the possibility of surface interactions. Using the free enthalpy of formation for the defects Maier calculated profiles for the electrochemical and chemical potentials, electric potential, charge density and dielectric displacement of the interface for the system MX/MX′.[142]

The early theoretical models for space-charge formation, such as those by Kliewer and Koehler and Blakely and Danyluk, all follow what is termed the global approach, where an expression for the free energy of the entire crystal is constructed then minimised to yield equations for the local defect concentrations. In 1980, Franceshetti proved that the same solution can be obtained using a local thermodynamic formalism, where electrochemical potentials are defined for the defect species and proper behaviour of the locally defined potentials in thermodynamic equilibrium is required.[158] This local thermodynamic formalism became the base for more recent models for the theoretical treatment of space charges.

In the years following Franceschetti's model, vast advancements in the understanding of space charge layers at various boundaries under a range of conditions were made by Maier. In 1995, Maier and co-workers presented a combined discrete–continuous model for quantitatively analysing interfaces in solid ionic conductors.[72] This differed from previous models, which focused on only a continuum description of the space charge region of the interface, and instead considered both the grain boundary core and space charge region. In the discrete-continuous model the interface is divided into core and space charge regions with the core being treated in a discrete manner using a Dirac delta function. By assuming the material constants, such as the standard chemical potentials and defect mobilities, behave as step functions, the space charge region is then treated using a standard continuum approximation.

In 2000, McIntyre introduced a mathematical model to calculate the equilibrium grain boundary depletion layer widths and conductivity profiles. In this model a method to numerically solve the Poisson-Boltzmann equation using an iterative procedure is described. Starting with an initial guess for the interfacial charge density, the Poisson-Boltzmann equation can be solved to calculate the potential (Φ), using boundary conditions defined as $\Phi_0 = 0.0$ and $\frac{d\Phi}{dx}_{\infty} = 0.0$. The potential is used to calculate the defect distributions and a new value of the charge density can be calculated. This sequence is iterated until the calculations converge on final values of the charge density, the potential, and the defect distribution.[159]

De Souza suggested an alternate route to calculate the space charge potential in 2002. In the approach of De Souza, Poisson's equation is solved numerically using an iterative procedure on one side of the grain boundary, using an initial guess for the boundary condition at Φ_0 and the second boundary condition $\frac{d\Phi}{dx}_{\infty} = 0.0$. Oxygen vacancies are treated as dilute non-interacting species and therefore the electrochemical potential follows a Boltzmann distribution. Following this, Gauss's law is applied to calculate the value of the grain boundary charge. The grain boundary charge is also calculated using an alternate route,

$$Q_{GB} = 2ew_c c_{i,\infty} \left(\frac{N_i \exp^{(-\Delta g_i + 2e\Phi_0)/kT}}{N_i + c_{i,\infty} \exp^{(-\Delta g_i + 2e\Phi_0)/kT}} \right), \tag{3.1}$$

and the value of Φ_0 is varied to minimise the difference between the two calculated values of the grain boundary charge.[160]

3.2 1D Space Charge Models

3.2.1 Poisson-Boltzmann Equation

A short derivation of the Poisson-Boltzmann equation follows, with full details given in section 4.1.

Most historical methods for calculating space-charge properties in solid electrolytes can be considered as "continuum" approaches, where charge carriers are treated as point charges within a continuum dielectric. As mentioned above, early theoretical models used to describe space-charge theory follow what is termed a global approach, whereby an expression for the free energy of the entire crystal is constructed, and then minimised to yield equations for the local defect concentrations.[153–155] This is equivalent to defining electrochemical potentials for the defect species and requiring that these defect species electrochemical potentials are equal throughout the system.[158] For some simple one-dimensional models, the problem of minimising the total free energy can be solved directly, or converted to a set of coupled second order differential equations to be solved using standard methods. A popular method to define the local equations that can be solved to minimise the free energy is the Poisson-Boltzmann model. The Poisson-Boltzmann model combines the defined electrochemical potential with Poisson's equation, resulting in an expression which can be solved self-consistently to describe the defect distributions, charge density and electrostatic potential over the interfacial region.[72,161]

The electrochemical potential for point defects in a continuum dielectric is given as,

$$\mu_i = \mu_i^\circ + RT\ln c_{i,x} + z_i F \Phi_x, \tag{3.2}$$

where μ_i° is the standard chemical potential, $RT\ln c_{i,x}$ is the free energy per mole due to configurational disorder, with the defect concentration $c_{i,x} = \frac{N_i}{N_{sites}}$. z_i is the charge of defect i, Φ is the electrostatic potential and F is the Faraday constant. At equilibrium, the electrochemical potential of each defect species is constant throughout the system. We can therefore equate the defect electrochemical potentials at each point in space with "bulk" values, where the bulk is defined as some reference point with $\Phi = 0$ and $c_i = c_\infty$, which allows the derivation of the Boltzmann relation,

$$c_{i,x} = \exp\left(\frac{\Delta\mu_i^\circ - z_i F \Delta\Phi_x}{RT}\right). \tag{3.3}$$

At each point, the charge density of each defect species is given by the product of that defect concentration and its charge, and summing these gives the net local charge density.

$$\rho = \sum_i c_{i,x} z_i F. \tag{3.4}$$

The local charge density is related to the second derivative of the electrostatic potential as given in Poisson's equation,

$$\nabla^2 \Phi_x = \frac{-\rho}{\epsilon \epsilon_0}. \tag{3.5}$$

These three relationships can be combined to give the Poisson-Boltzmann equation as described,

$$\nabla^2 \Phi = -\sum_x \frac{c_\infty z_i F}{\epsilon_0 \epsilon} \exp\left(\frac{-z_i F \Phi_x}{kT}\right). \tag{3.6}$$

3.2.2 Analytical Poisson-Boltzmann Solutions

The Linearised Poisson-Boltzmann Equation

A linearised form of the PB equation (Eqn. 3.7) can be derived by expanding the exponential term as a Taylor expansion around $\Phi = 0$, and taking only linear terms, for example assuming Φ is small ($\frac{-zF\Phi}{kT} \rightarrow 0.0$) . This gives a linear equation of the form,

$$\nabla^2 \Phi \approx -\sum_x \frac{c_\infty z_i F}{\epsilon_0 \epsilon} \left(1 - \frac{z_i F \Phi_x}{kT}\right), \tag{3.7}$$

which can be expanded,

$$\nabla^2 \Phi \approx -\sum_x \frac{c_\infty z_i F}{\epsilon_0 \epsilon} - \sum_x \frac{z_i^2 F^2 c_\infty \Phi_x}{\epsilon_0 \epsilon kT}. \tag{3.8}$$

As the first summation is zero due to electroneutrality, the linearised Poisson-Boltzmann equation becomes

$$\nabla^2 \Phi \approx \sum_x \frac{z_i^2 F^2 c_\infty \Phi_x}{\epsilon_0 \epsilon kT}. \tag{3.9}$$

The general solution of the "linearised Poisson-Boltzmann" equation, assuming a 1:1 electrolyte with equal but opposite charge is

$$\Phi_x = C_1 \cdot \exp^{-\kappa x} + C_2 \cdot \exp^{\kappa x} \tag{3.10}$$

with

$$\kappa = \sqrt{\frac{2c_o e^2}{\epsilon\epsilon_0 k_B T}} \tag{3.11}$$

C_1 and C_2 are constants, which are defined by the boundary conditions. If we use Dirichlet boundary conditions and require that $\Phi(x = 0) = \Phi_0$ and $\Phi(x \to \infty) = 0$, then $C_1 = \Phi_0$ and $C_2 = 0$. Using this choice of boundary condition means that the grain boundary core is not explicitly included in the model, but only appears by determining Φ_0 to set as the $x = 0$ boundary, which is typically referred to as the "space-charge potential".

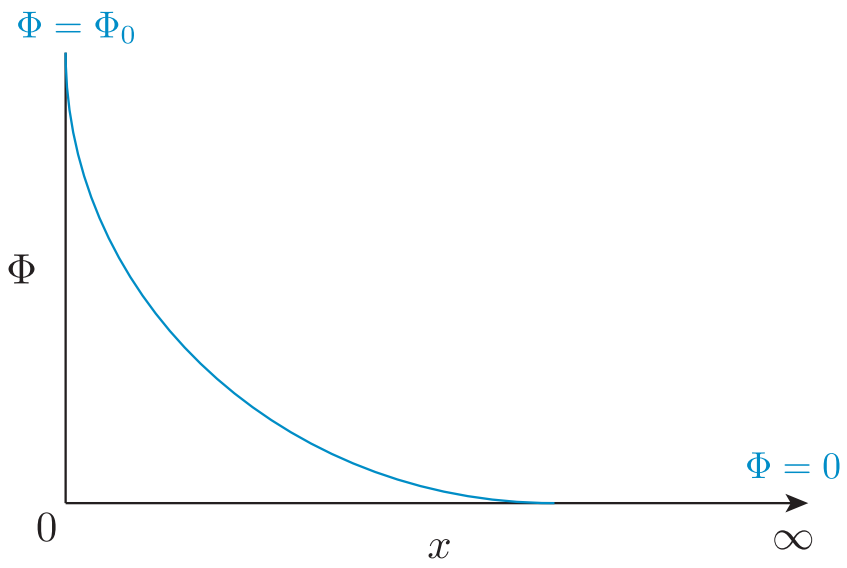

Figure 3.1: Dirichlet boundary conditions are applied to calculate the space charge potential from the grain boundary into the bulk.

The potential is then given by

$$\Phi = \Phi_0 \cdot \exp^{-\kappa x}. \tag{3.12}$$

Factoring out Φ, the constants can be assigned to κ^2,

$$\kappa^2 = \sum_x \frac{z_i^2 F^2 c_\infty}{\epsilon_0 \epsilon k T}. \tag{3.13}$$

The Debye length, the characteristic length scale for which the charged region around a defect decays monotonically, is equivalent to $\frac{1}{\kappa}$ and is given by the expression,

$$\lambda_D = \sqrt{\frac{\epsilon \epsilon_0 k T}{z_i^2 F^2 c_\infty}}. \tag{3.14}$$

3.2.3 Mott-Schottky and Gouy-Chapman Approximations

Defects in a solid electrolyte structure may be considered either immobile or mobile, meaning two approximations need to be considered. If some defects are considered immobile, the space charge model follows a Mott-Schottky approximation whereas if all defects are considered mobile, the space charge model follows a Gouy-Chapman approximation.

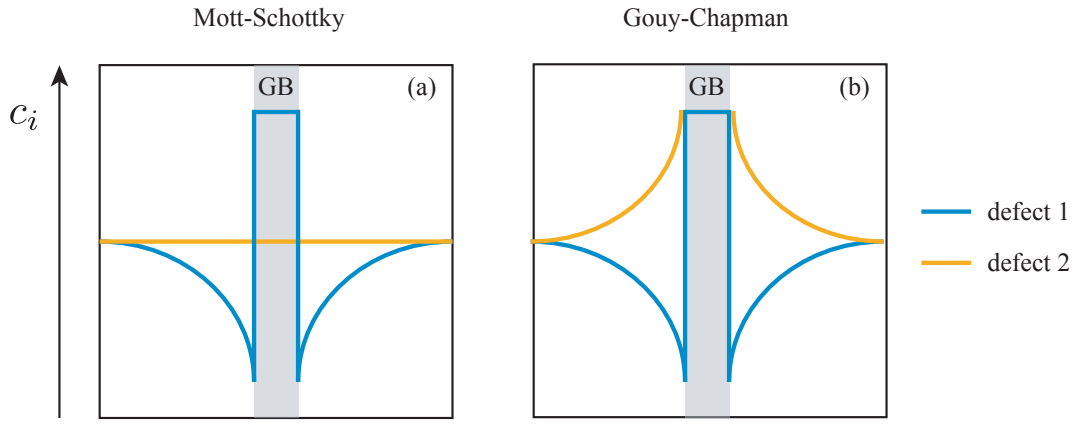

Figure 3.2: Schematic describing the defect distribution between Mott-Schottky approximation (a) and Gouy-Chapman approximation (b)

The approximation used has an effect on the defect distribution as shown in figure 3.2. We consider two cases, each with two defect species. In the Mott-Schottky model figure 3.2(a), defect 1 is free to equilibrate, and segregates to the grain boundary core. The concentration of defect 2, however, is held fixed at a uniform bulk value. In the Gouy-Chapman model 3.2(b) both defects are free to equilibrate. Due to electrostatic attractions, defect two will segregate to the space-charge regions. The enrichment of compensating defects in the space-charge region will affect the potential across the boundary, with the positive potential from the grain boundary core being shielded and decaying more rapidly into the

bulk.

3.2.4 Predicting the Space Charge Potential from the Mott-Schottky Model

As previously discussed, the space charge models discussed so far do not explicitly include information regarding the grain boundary core, which is only considered by defining the boundary conditions via the space charge potential. The space charge potential therefore defines the space charge profile and derived properties. Because the space charge potential has become so important from a theoretical perspective, one of the questions for experimental research has been to estimate the space charge potential from experimental data. One approach is to derive the space charge potential from experimental conductivity data, usually measured using impedance spectroscopy (discussed in appendix A) and converted into a space charge potential using the Mott-Schottky model.

As described in section 3.2.1, the defect concentration at a given lattice site is given by

$$c_{i,x} = c_\infty \exp\left(-\frac{zF\Phi_x}{kT}\right), \tag{3.15}$$

and the ionic conductivity in an homogenous system is given by

$$\sigma = cz\mu, \tag{3.16}$$

defined as conductance per unit length. Under Mott-Schottky conditions, with only one mobile defect species that has a constant valence and mobility, the grain boundary conductivity (ratio with respect to the bulk conductivity) becomes,

$$\sigma_{GB} = \frac{\sigma_x}{\sigma_\infty} = \frac{c_{i,x}}{c_\infty} = \exp\left(-\frac{zF\Phi_x}{kT}\right). \tag{3.17}$$

As $\sigma = \frac{1}{\rho}$, inverting the conductivity to get the grain boundary resistivity gives,

$$r_{GB} = \frac{\rho_x}{\rho_\infty} = \frac{c_\infty}{c_{i,x}} = \exp\left(\frac{zF\Phi_x}{kT}\right). \tag{3.18}$$

For an inhomogenous system, the net resistivity is obtained by integrating $\frac{1}{c_i}$ from $x_{\min}$ to $x_{\max}$ and dividing by length $x_{\min} - x_{\max}$. According to the brick layer model, the grain

boundary is between two adjacent space charge regions. The effective resistivity of a grain boundary can be approximated as the resistivity across the two space charge regions, and the grain boundary core,

$$\rho_{SC} = \frac{1}{2\delta_{SC}} \int_0^{2\delta_{SC}} \rho_x \mathrm{d}x, \tag{3.19}$$

therefore the grain boundary resistivity can be defined as

$$r_{GB} = \frac{\exp\left(zF\Phi_0/kT\right)}{2zF\Phi_0/kT}. \tag{3.20}$$

The expression detailed in equation 3.20, is known the Mott-Schottky model. From experimental conductivity data, the Mott-Schottky model can be used to calculate the space charge potential Φ_0, by rearranging equation 3.20 to make the space charge potential the subject,

$$\Phi_0^{MS} = -\mathrm{LambertW}(-1/2r_{\mathrm{GB}})(kT/zF). \tag{3.21}$$

Where the LambertW function is a set of functions of the inverse relation $f(x) = x\exp^a x$, where $x = \frac{\mathrm{LambertW}(z\ln a)}{\ln a}$. a and x are real numbers and z is an imaginary number.[162] The Mott-Schottky model assumes that the grain boundary region is negligibly thin, and that mobile charge carriers are fully depleted in the space charge region. This gives an analytical description of space charge behavior that can be completely characterised by the space charge potential.

3.2.5 Numerical Models

Because the Poisson–Boltzmann equation is a partial differential of second order, it is commonly solved numerically. Simple space charge models solve the Poisson-Boltzmann equation by defining the boundary conditions at the grain boundary core. Historically these models are "top-down" whereby the electrostatic potential is defined at the grain boundary core, although more recently "bottom up" models are being used more frequently, whereby the defect segregation energy is defined at the grain boundary core. The electrostatic potential is then calculated using a finite difference approximation (discussed in more detail in section 4.3.1), or equivalent, on a continuum from the grain boundary into the bulk.

'Top Down' Models

Standard space charge models solve the Poisson-Boltzmann equation by defining the space charge potential at the grain boundary core. The boundary conditions require that at the boundary the potential is the space charge potential, $\Phi(x = 0) = \Phi_0$ and at a large distance from the boundary, the potential should become zero, $\Phi(x \to \infty) = 0$. As the space charge potential is dependent on the core defect densities, the space charge potential cannot be expressed using materials constants analytically.[163] These space charge potentials are often taken directly from experimental measurements - using the Mott-Schottky model as defined above.[164–166] Alternatively, the space charge potential can described via the free energies of defect segregation as $\Delta G = nF\Phi$.[167] ΔG can be calculated through ab initio or classical calculations and once Φ_0 has been calculated it can be used as the input for the Poisson-Boltzmann solver.

'Bottom Up' Models

The electrochemical potentials used to describe the defect distributions are defined from the standard free enthalpy of defect segregation ΔE_{seg}, where $\Delta E_{\text{seg}} = \Delta E_{\text{core}} - \Delta E_{infty}$. These ΔE values can be calculated using ab initio or classical atomistic calculations and then can be used as the input to solve the Poisson-Boltzmann equation.[163] Similarly to the 'top down' approach, the boundary conditions require that at the boundary the segregation energy is initially defined in order to calculate the electrostatic potential over the region. The inputs for the calculation are $\Delta E_{\text{seg}}(x = 0) = \Delta E_{\text{seg,GB}}$ and $\Delta E_{\text{seg}}(x \to \infty) = 0$. 'Bottom up' models have become more prevalent as the data is collected fully computationally, and the assumptions made when interpreting a space charge potential from experimental data is avoided.

3.2.6 Extensions to Poisson Boltzmann Modelling

While the Poisson-Boltzmann model is a good approximation for modelling space-charge formation, it does make certain assumptions regarding the crystalline system. The first of which is that the ions exist as point charges within a dielectric continuum, with no structural changes between the grain boundary and the bulk. Secondly, the model assumes that the point defects exist in the dilute limit with no interactions other than electrostatics and finally the model assumes that defect mobility remains constant throughout the system. While this is not an exhaustive list of the assumptions made, it highlights the key limitations of Poisson-Boltzmann modelling in its most commonly used form.

"Fermi-Dirac–like" Statistics

While the Boltzmann relation is suitable for dilute limit liquids, in crystalline solids there are limits on site occupation due to the limited number of sites which can be occupied by a defect. In the case of solid electrolytes, replacing the ideal gas entropy with the configurational entropy for a non-interacting lattice gas by taking the electrochemical potential of a "Fermi-Dirac–like" distribution gives a more realistic expression for the defect distribution in boundary layers. This leads to a concentration term in the form,

$$c_{i,x} = \frac{c_{i,\infty} \exp\left(\frac{\Delta\mu_i^o - z_i F\Phi}{RT}\right)}{1 + c_{i,\infty}\left(\exp\left(\frac{\Delta\mu_i^o - z_i F\Phi}{RT}\right) - 1\right)} \tag{3.22}$$

which gives a more accurate description of the defect distributions in solid electrolytes. The full derivation for the "Fermi-Dirac–like" model is given in section 4.1.2.

Poisson-Cahn Model

Mebane and De Souza[168] have discussed how the Poisson-Boltzmann model assumes that point defects are dilute, non-interacting (except electrostatics) moieties and that space charge layers are assumed to be regions of constant defect mobilities, but with altered defect concentrations. At low defect concentrations, these are reasonable assumptions but as the concentration increases (approximately above 1% dopant concentration), defect–defect interactions must be taken into consideration. In the Poisson-Cahn study, they present a framework which, they claim, is able to model defect redistribution at boundaries over a range of defect concentrations from dilute to concentrated solid solutions. In their model, they replace the Boltzmann model with the Cahn-Hilliard theory of inhomogenous systems,[169] producing what they refer to as the "Poisson-Cahn theory".

Mebane and De Souza claim that following the Poisson-Cahn approach the condition for equilibrium is, as with the Poisson-Boltzmann approach, that the electrochemical potentials for all mobile defects are constant throughout the system and the electrostatic potential follows Poisson's equation. Concluding that the model conforms to the dilute Poisson-Boltzmann case for low dopant concentrations, as at low dopant concentrations n_a and n_v tend to zero and therefore $\mu \longrightarrow \mu_v + RT\ln\frac{n_v}{1-n_v} + zF\Phi$ which is the non-interacting case. Whilst the model appears to conform to the results of atomistic simulation in the concentrated case. While there seem to be advantages to using a Poisson-Cahn model, it cannot be used for a "bottom-up" model with all parameters derived from atomistic calculations.

In particular calculation of the concentration curvature terms, which is considered critical to the Poisson-Cahn approach, is not accessible through atomistic calculations and therefore the model relies on experimental data to agree with the comparative experimental data.

3.3 Atomistic Modelling

One approach to analyse space charge properties is to employ atomistic modelling. The main feature of atomistic modelling is that atoms are described explicitly, and their interactions are described either from first principles or from effective interatomic potentials. Once the interactions are described, atomistic molecular dynamics or Monte Carlo techniques can be used to sample different atomic configurations from a particular ensemble and examine the relationship between the crystal structure, defect distributions and ionic conductivities.[84–87] Many interatomic potential models exist that can be used to describe the interactions between the ions. The ions are allowed to redistribute over an appropriate time scale and at the point that thermodynamic equilibrium is achieved, the equilibrium defect distribution can be extracted. For molecular dynamics the atomic transport properties, such as the diffusion coefficient, activation energy and ionic conductivities can be extracted from the simulations using time dependent mean squared displacements. Atomistic techniques give a complete description of the time-average positions in 3D space, although they are computationally expensive and conceptually complex.

Static atomistic models can be used to calculate defect segregation energies. One potential model, that has been used through this work, is to use the Born model, where the ions interact via long range Coulombic terms and short range repulsive terms and the defect segregation energies are extracted and used in a “bottom-up” Poisson-Boltzmann model.

3.4 Integrated Atomistic and Continuum Modelling

Improving the physical accuracy of space charge models is of significance in understanding defect behaviour and grain boundary effects in solid electrolytes. One approach to improving the accuracy of Poisson-Boltzmann models, and allowing them to calculate predictive properties without experimental input, is to use combined atomistic-continuum modelling. In these integrated models the 1D Poisson-Boltzmann model is parameterised for specific systems using data derived directly from atomistic calculations.[170] One popular input parameter for the Poisson-Boltzmann model is to use defect segregation energies, calcu-

lated either using classical interatomic potentials or first principles. There have been a number of recent papers where input data obtained from atomistic calculations has been applied to a 1D Poisson-Boltzmann model to simulate space charges, discussed fully in chapter 5, however these different studies have implemented the theory using a variety of methods.[171–173] These methods often vary in terms of the spatial representation of the system. Most commonly space charge models assume that the crystal structure behaves as a continuum, although the definition of the grain boundary core is not clear.

The model presented in this work extends the previously presented integrated atomistic-continuum models into a novel, fully site explicit space charge model. Individual defect segregation energies are calculated at each crystalline lattice site from the grain boundary into the bulk material and are used as the input for the Poisson-Boltzmann model. This allows calculation of the local electrostatic potential and defect distribution at each explicit site, removing the need for a precise definition of the grain boundary core. Due to the varying complexity of the integrated models, it is important to present a comparative study of these space charge models to display how the definition of the grain boundary core and the inclusion of explicit lattice structure affects the calculated space charge properties of the system.

Chapter 4

Mathematical and Computational Models

4.1 Poisson-Boltzmann Equation

4.1.1 Boltzmann distribution

Defect distributions at boundary conditions are derived from the equality of electrochemical potentials at spatial equilibrium

$$\mu_i = \mu_\infty. \tag{4.1}$$

For a Boltzmann distribution, the electrochemical potential is given as

$$\mu_i = \mu_i^o + RT \ln c_{i,x} + z_i F \Phi_x, \tag{4.2}$$

where μ_i^o is the standard chemical potential, $RT \ln c_{i,x}$ is the free energy per mole due to configurational disorder, with the defect concentration $c_{i,x} = \frac{N_i}{N_{sites}}$. z_i is the charge of defect i, Φ_x is the electrostatic potential and F is the Faraday constant.

The equality of electrochemical potentials between the bulk and the boundary layer at spatial equilibrium,

$$\mu_{i,x}^o + RT \ln c_{i,x} + z_i F \Phi_x = \mu_{i,\infty}^o + RT \ln c_{i,\infty} + z_i F \Phi_\infty, \tag{4.3}$$

allows the Boltzmann relation to be derived:

$$RT \ln c_{i,x} - RT \ln c_{i,\infty} = -\left(\mu^o_{i,x} - \mu^o_{i,\infty}\right) - \left(z_i F \Phi_x - z_i F \Phi_\infty\right), \tag{4.4}$$

$$\ln\left(\frac{c_{i,x}}{c_{i,\infty}}\right) = -\frac{\mu^o_{i,x} - \mu^o_{i,\infty}}{RT} - \frac{z_i F(\Phi_x - \Phi_\infty)}{RT}, \tag{4.5}$$

$$\frac{c_{i,x}}{c_{i,\infty}} = \exp\left(\frac{-\left(\Delta\mu^o_i + z_i F \Delta\Phi_x\right)}{RT}\right), \tag{4.6}$$

$$c_{i,x} = c_{i,\infty} \exp\left(-\frac{\Delta\mu^o_i + z_i F \Delta\Phi_x}{RT}\right). \tag{4.7}$$

The Boltzmann relation is a thermodynamic principle which states that the ratio between two states is proportional to an exponential of the difference in potential energies, normalised by the thermal energy.

4.1.2 'Fermi-Dirac like' distribution

The Boltzmann relation is acceptable for dilute limit liquids, however crystalline solids have a limited number of sites which may or may not be occupied by a defect. In the case of solid electrolytes, taking the electrochemical potential of a 'Fermi-Dirac like' distribution gives a more realistic expression for the defect distribution in boundary layers.

Deriving the electrochemical potential

The electrochemical potential of a 'Fermi-Dirac like' distribution is

$$\mu = \mu^o_{i,x} + RT \ln\left(\frac{c_{i,x}}{1 - c_{i,x}}\right) + z_i F \Phi_x \tag{4.8}$$

Standard chemical potential The standard chemical potential μ^o_i is defined as *'how the Gibbs energy of a system changes when a substance is added to it'*.[174]

$$\mu^o_i = \left(\frac{\delta G}{\delta n}\right), \tag{4.9}$$

where G is the Gibbs energy of the system. If $\mu^o_i > 0.0$, the Gibbs energy increases as n

is increased. For a pure substance, the Gibbs energy $G = ng_i^o$, therefore,[174]

$$\mu_i^o = \left(\frac{\delta(ng_i^o)}{\delta n}\right) = g_i^o. \tag{4.10}$$

As

$$G = H - TS, \tag{4.11}$$

where H is the free enthalpy, T is the temperature in Kelvin and S is the entropy,

$$g_i^o = H_i^o + g_{\mathrm{vib}i}^o, \tag{4.12}$$

$$g_i^o = H_i^o + g_{\mathrm{vib}i}^o, \tag{4.13}$$

where $g_{\mathrm{vib}i}^o$ is the defect vibrational entropy and

$$H_i^o = U_i^o + pV, \tag{4.14}$$

where U_i^o is the internal energy change with the addition of defect i, p is the pressure and V is the volume, it can be concluded that the standard chemical potential of the system is defined as

$$\mu_i^o = g_i^o = U_i^o + p\Delta V_i^o + g_{\mathrm{vib}i}^o. \tag{4.15}$$

Electrostatics If the N particles have charge z and feel a mean electropotential Φ, the Gibbs free energy is

$$G = H - TS + z\Phi, \tag{4.16}$$

therefore, $z_i F \Phi_x$ in the electrochemical potential is the point defect electrostatic term.

Configurational disorder Any crystal in thermodynamic equilibrium at a finite temperature contains a finite number of point defects, because the introduction of new defects

significantly increases the number of possible configurations.[175] Boltzmann's equation is a probability equation relating the entropy S of an ideal gas to the quantity W, the number of real microstates corresponding to the gas' macrostate.

$$S = k \ln W, \tag{4.17}$$

where W is the ratio of the number of available sites N and the number of defective sites n. The distribution configuration can be achieved in W ways, where W is the weight of the configuration, given by

$$W = \left(\frac{N}{n}\right) = \frac{N!}{n!(N-n)!}. \tag{4.18}$$

It is more convenient to deal with the natural logarithm of W, where $\ln\left(\frac{x}{y}\right) = \ln x - \ln y$,

$$\ln W = \ln N! - \ln n! - \ln(N-n)!, \tag{4.19}$$

because it allows the simplification of the factorials using Stirling's approximation, $\ln x! \approx x \ln x - x$ for large x.

$$\ln W = N \ln N - N - n \ln n + n - (N-n) \ln(N-n) + (N-n), \tag{4.20}$$

which can be simplified to give the expression

$$\ln W = N \ln N - n \ln n - (N-n) \ln(N-n). \tag{4.21}$$

As $c = \frac{n}{N}$, n can be replaced by Nc,

$$\ln W = N \ln N - Nc \ln Nc - (N-n) \ln(N-n), \tag{4.22}$$

then the logarithms can be expanded,

$$Nc \ln Nc = Nc \ln N + Nc \ln c. \tag{4.23}$$

and as $N - c = N(1 - c)$,

$$(N - Nc)\ln(N - Nc) = N\ln N - Nc\ln N + N(1 - c)\ln(1 - c). \tag{4.24}$$

Therefore,

$$\ln W = N\ln N - Nc\ln N - Nc\ln c - N\ln N - Nc\ln N + N(1 - c)\ln(1 - c), \tag{4.25}$$

cancelling like terms gives

$$\ln W = -Nc\ln c + N(1 - c)\ln(1 - c), \tag{4.26}$$

and factorising out the N leaves

$$\ln W = -N(c\ln c + (1 - c)\ln(1 - c)). \tag{4.27}$$

An expression for the configurational entropy S is given as

$$S = -kN(c\ln c + (1 - c)\ln(1 - c)), \tag{4.28}$$

and the configurational entropy contribution to the defect electrochemical potential is $\frac{dS}{dc}$. Using the chain rule, $\frac{d}{dx}xlnx = \ln x + 1$ and $\frac{d}{dx}(1 - x)\ln(1 - x) = -\ln(1 - x) + 1$,

$$\frac{dS}{dc} = -kN(\ln c - 1 - \ln(c - 1) + 1) \tag{4.29}$$

which can be simplified to give the textbook expression for the free energy per mole due to configurational disorder,

$$\frac{dS}{dc} = -kN\ln\left(\frac{c}{1 - c}\right) = -R\ln\left(\frac{c}{1 - c}\right). \tag{4.30}$$

4.1.3 Deriving the 'Fermi-Dirac like' concentration term

Taking equality of the electrochemical potentials between the bulk and boundary layer at spatial equilibrium,

$$\mu = \mu_{i,x}^{o} + RT \ln\left(\frac{c_{i,x}}{1 - c_{i,x}}\right) + z_i F \Phi_x \tag{4.31}$$

the 'Fermi-Dirac like' concentration term can be derived. Like terms are collected,

$$RT \ln\left(\frac{c_{i,x}}{1 - c_{i,x}}\right) - RT \ln\left(\frac{c_{i,\infty}}{1 - c_{i,\infty}}\right) = \mu_{i,\infty}^{o} + z_i F \Phi_\infty - \mu_{i,x}^{o} - z_i F \Phi_i, \tag{4.32}$$

and both sides are divided through by RT,

$$\ln\left(\frac{\left(\frac{c_{i,x}}{1-c_{i,x}}\right)}{\left(\frac{c_{i,\infty}}{1-c_{i,\infty}}\right)}\right) = \frac{\mu_{i,x}^{o} - \mu_{i,\infty}^{o}}{RT} - \frac{z_i F \left(\Phi_\infty - \Phi_i\right)}{RT}. \tag{4.33}$$

The exponential of both sides is taken,

$$\frac{\left(\frac{c_{i,x}}{1-c_{i,x}}\right)}{\left(\frac{c_{i,\infty}}{1-c_{i,\infty}}\right)} = \exp\left(\frac{\Delta\mu_i^{o} - z_i F \Phi}{RT}\right), \tag{4.34}$$

and both sides are multiplied by $\frac{c_{i,\infty}}{1-c_{i,\infty}}$.

$$\frac{c_{i,x}}{1 - c_{i,x}} = \frac{c_{i,\infty} \exp\left(\frac{\Delta\mu_i^{o} - z_i F \Phi}{RT}\right)}{1 - c_{i,\infty}}, \tag{4.35}$$

Both sides are multiplied by $1 - c_{i,x}$,

$$c_{i,x} = (1 - c_{i,x}) \left(\frac{c_{i,\infty} \exp\left(\frac{\Delta\mu_i^{o} - z_i F \Phi}{RT}\right)}{1 - c_{i,\infty}}\right), \tag{4.36}$$

and the expression is expanded,

$$c_{i,x} = \frac{c_{i,\infty} \exp\left(\frac{\Delta\mu_i^{o} - z_i F \Phi}{RT}\right)}{1 - c_{i,\infty}} - c_{i,x} \left(\frac{c_{i,\infty} \exp\left(\frac{\Delta\mu_i^{o} - z_i F \Phi}{RT}\right)}{1 - c_{i,\infty}}\right). \tag{4.37}$$

Adding the minus term to both sides, and factorising for $c_{i,x}$ gives,

$$c_{i,x}\left(1+\frac{c_{i,\infty}\exp\left(\frac{\Delta\mu_i^o-z_iF\Phi}{RT}\right)}{1-c_{i,\infty}}\right)=\frac{c_{i,\infty}\exp\left(\frac{\Delta\mu_i^o-z_iF\Phi}{RT}\right)}{1-c_{i,\infty}}, \tag{4.38}$$

and dividing by the bottom term on the left hand side gives an expression for the defect concentration of defect i at position x,

$$c_{i,x}=\frac{\frac{c_{i,\infty}\exp\left(\frac{\Delta\mu_i^o-z_iF\Phi}{RT}\right)}{1-c_{i,\infty}}}{1+\left(\frac{c_{i,\infty}\exp\left(\frac{\Delta\mu_i^o-z_iF\Phi}{RT}\right)}{1-c_{i,\infty}}\right)}. \tag{4.39}$$

The expression for the defect concentration can be simplified by replacing the 1 with $\frac{1-c_{i,\infty}}{1-c_{i,\infty}}$,

$$c_{i,x}=\frac{\frac{c_{i,\infty}\exp\left(\frac{\Delta\mu_i^o-z_iF\Phi}{RT}\right)}{1-c_{i,\infty}}}{\frac{1-c_{i,\infty}}{1-c_{i,\infty}}+\left(\frac{c_{i,\infty}\exp\left(\frac{\Delta\mu_i^o-z_iF\Phi}{RT}\right)}{1-c_{i,\infty}}\right)} \tag{4.40}$$

cancelling through by $1-c_{i,\infty}$,

$$c_{i,x}=\frac{c_{i,\infty}\exp\left(\frac{\Delta\mu_i^o-z_iF\Phi}{RT}\right)}{1-c_{i,\infty}+c_{i,\infty}\exp\left(\frac{\Delta\mu_i^o-z_iF\Phi}{RT}\right)}, \tag{4.41}$$

and factorising for $c_{i,\infty}$ on the bottom term, to give the final expression for the 'Fermi-Dirac like' concentration.

$$c_{i,x}=\frac{c_{i,\infty}\exp\left(\frac{\Delta\mu_i^o-z_iF\Phi}{RT}\right)}{1+c_{i,\infty}\left(\exp\left(\frac{\Delta\mu_i^o-z_iF\Phi}{RT}\right)-1\right)} \tag{4.42}$$

4.1.4 Deriving the Poisson-Boltzmann equation

The charge density is proportional to the sum of defect concentrations given by

$$\rho=\sum_i c_iz_iF, \tag{4.43}$$

where ρ is the charge density. The electrostatic potential in turn depends on the charge density as described by Poisson's equation, which provides the complete electrical information and is obtained from Maxwell's equations.

$$\nabla^2\Phi = \frac{-\rho}{\epsilon\epsilon_0}, \tag{4.44}$$

where ϵ is the relative permittivity and ϵ_0 is the vacuum permittivity.

These relationships can then be combined to give the Poisson-Boltzmann equation,

$$\nabla^2\Phi = \frac{1}{\epsilon\epsilon_0}\sum_i \frac{c_\infty \exp\left(\frac{-z_i\Delta\Phi_x+\Delta\mu_i}{kT}\right)}{1+c_\infty\left(\exp\left(\frac{-z_i\Delta\Phi_x+\Delta\mu_i}{kT}\right)-1\right)} z_i F. \tag{4.45}$$

For solid electrolytes, the Poisson-Boltzmann equation is often solved by setting the boundary condition to the grain boundary potential. However, the standard chemical potential can be replaced by defect segregation energies (ΔE_i) due to the $p\Delta V_i^o + \mu_{\mathrm{vib}i}$ terms being considered as insignificant compared to the U_i^o term. ΔE_i can be obtained from atomistic calculations, and allows the grain boundary to be treated explicitly.

$$\nabla^2\Phi = \frac{1}{\epsilon\epsilon_0}\sum_i \frac{c_\infty \exp\left(\frac{-z_i\Delta\Phi_x+\Delta E_i}{kT}\right)}{1+c_\infty\left(\exp\left(\frac{-z_i\Delta\Phi_x+\Delta\ E_i}{kT}\right)-1\right)} z_i F. \tag{4.46}$$

ΔE_i is defined as the difference between the formation energy of a defect at a site and the formation energy of a defect in the bulk, normalised relative to the segregation energy of a defect in the bulk being equal to 0.0 eV.

4.2 Defect Segregation Energies

4.2.1 Grain Boundary Modelling

Using bulk crystal structures obtained from online databases, surfaces can be created by cleaving the bulk crystal. Cleavage of the bulk crystal in different planes will result in different surface terminations.

Grain boundaries are commonly created by conjoining two surfaces. To find the lowest energy grain boundary structure, the surfaces are allowed to relax and then they undergo energy minimisation. The energy minimisation technique commonly employed when form-

ing grain boundaries is static lattice energy minimisation. The ions are fixed to their sites and the surface positions relative to one another are altered until the lowest energy configuration is found. The forces are calculated using a potential model, as described in section 4.2.2.

4.2.2 Calculating Defect Segregation Energies

First principles

The Schrodinger equation First principles methods involve using fundamental physics to describe and predict the behaviour of electrons. A wave function Ψ, is a description detailing the quantum properties of an electron. Therefore the many-body, time-independent Schrodinger equation is of upmost importance,

$$\hat{H}\Psi = E\Psi, \tag{4.47}$$

where $\hat{H}$ is the Hamiltonian operator, Ψ is the many-body wave function, a set of eigenstates of the Hamiltonian and E is the energy of a n-particle system, the associated eigenvalue that satisfies the eigenvalue equation.

Two assumptions are made. Firstly, due to the electrons being much lighter than the atomic nuclei, it is assumed that electrons respond instantaneously to changes in surroundings and nuclei stationary.[176] This is the Born-Oppenheimer approximation, which allows electrons and nuclei to be treated separately. Secondly, only electronic forces and kinetic energy are considered, gravity and nuclear forces are neglected.[177]

The Hamiltonian operator can be constructed from the different types of interaction that occur within molecules and solids,

$$\hat{H} = \left[\frac{h^2}{2m} \sum_{i\ 1}^{N} \nabla_i^2 + \sum_{i\ 1}^{N} V(\mathbf{r}_i) + \sum_{i\ 1}^{N} \sum_{j<i} U(\mathbf{r}_i, \mathbf{r}_j) \right], \tag{4.48}$$

where m is the electron mass, the first term is the kinetic energy of each electron, the second term is the interaction energy between each electron and the collection of atomic nuclei and the third term is the interaction energy between different electrons.

Hartree-Fock method It is possible to approximate Ψ as a product of individual electron wavefunctions, known as the Hartree product,[176]

$$\Psi = \Psi_1(\mathbf{r})\Psi_2(\mathbf{r})...\Psi_N(\mathbf{r}). \tag{4.49}$$

This is a key approximation within the Hartree-Fock method. The 'mean field approximation', where the one-electron wavefunctions are treated as independent of one another, but all interacting with an average field. In order to treat the eigenvalue problem with conventional linear algebra, the one electron wavefunctions are treated as linear combinations of a restricted set of mathematical functions — the basis set.[177] Two further constraints are applied to the formation of an acceptable set of wavefunctions. The first is orthonormality, the combined description of normalisation, where the square of the wavefunction represents the electron density, the probability of finding the N electrons anywhere in space must be exactly unity, and orthogonality, where there is no net overlap for any two wavefunctions in a given system.[178] The second, anti-symmetry This constraint implements the Pauli exclusion principle; if two electrons are described with the same set of quantum numbers Ψ becomes zero, which fails to satisfy orthonormality. These are both motivated by fundamental physics.[177]

Density functional theory The problem with the Hartree-Fock method is in the mean field approximation neglecting electron correlation.[178] Density functional theory (DFT) is a phenomenally successful approach to finding solutions to the Schrodinger equation.[176] DFT is based on two fundamental mathematical theorems proved by Kohn and Hohenberg,[179] which state that the total energy, including both exchange and correlation energies, of an electron gas is a unique functional of the electron density. The minimum value of this functional yields the ground state energy, and the corresponding density is the exact single electron ground state density.[180] This proof was then implemented using the derivation of a set of equations by Kohn and Sham.

The density of electrons at a particular position in space ($n(r)$), can be written in terms of the individual electron wave functions as

$$n(\mathbf{r}) = 2\sum_i \Psi_i^*(\mathbf{r})\Psi_i(\mathbf{r}), \tag{4.50}$$

where the summation is the probability that an electron in an individual wave function is located at position $\mathbf{r}$.

The functional described by the Hohenberg-Kohn theorem can be written in terms of the

single-electron wave functions,

$$E[\Psi_i] = E_{\text{known}}[\Psi_i] + E_{\text{XC}}[\Psi_i], \tag{4.51}$$

where the functional has been split into a collection of terms that can be written in an analytical form, E_{known}, and the terms that cannot, E_{XC} - The exchange correlation functional. The known terms include four contributions, the electron kinetic energies, the Coulomb interactions between electrons and nuclei, the Coulomb interactions between pairs of electrons and the Coulomb interactions between pairs of nuclei,

$$E_{\text{known}}[\Psi_i] = \frac{h^2}{m}\sum_i \int \Psi_i^* \nabla^2 \Psi_i d^3r + \int V(\mathbf{r}) n(\mathbf{r}) d^3r + \frac{e^2}{2}\int\int \frac{n(\mathbf{r})n(\mathbf{r}')}{|\mathbf{r}\ \mathbf{r}'|} d^3r d^3r' + E_{\text{ion}}. \tag{4.52}$$

Kohn and Sham expressed electron density as a function of a set of equations, each involving a single electron, avoiding the summations inside the full Schrodinger equation,

$$\left[\frac{h^2}{2m}\nabla^2 + V(\mathbf{r}) + V_H(\mathbf{r}) + V_{\text{XC}}(\mathbf{r})\right]\Psi_i(\mathbf{r}) = \epsilon_i \Psi_i(\mathbf{r}). \tag{4.53}$$

V is the potential defining the interaction between an electron and the nuclei, the Hartree potential,

$$V_H(\mathbf{r}) = e^2 \int \frac{n(\mathbf{r}')}{\mathbf{r}\ |\mathbf{r}'|} d^3r', \tag{4.54}$$

which describes the Coulomb repulsion between the electron being considered and the total electron density, and

$$V_{\text{XC}}(\mathbf{r}) = \frac{\delta E_{\text{XC}}(r)}{\delta n(\mathbf{r})}, \tag{4.55}$$

the functional derivative of the exchange correlation energy. This leads to a self-consistent iterative method for solving the Kohn-Sham equations:

- Define an initial electron density.
- Solve Kohn-Sham equations to find single particle wave functions.

- Calculate electron density defined from single particle wave functions.
- Compare new electron density with original electron density. If they are the same, it is the ground state electron density. If not, update electron density and continue iteration.[176,181]

Exchange correlation functional E_{XC} is defined to include the quantum mechanical effects. Defining E_{XC} is extremely difficult for most systems and is not known. In the case of a uniform electron gas, E_{XC} can be derived exactly as $n(r)$ is constant. Therefore the exchange correlation potential can be set to the known exchange-correlation potential for the uniform electron gas,

$$V_{\mathrm{XC}}(\mathbf{r}) = V_{\mathrm{XC}}^{\text{electron gas}}[n(\mathbf{r})]. \tag{4.56}$$

This is known as the local density approximation (LDA), which allows complete definition of the Kohn-Sham equations but is not exact. There is a broad range of functionals which can be used to define E_{XC} which include varying degrees of physical information, providing varying degrees of accuracy.[176,181]

Calculating defect formation energies The theoretical background of DFT leads to the description of interesting properties. When modelling crystalline structures, the ground state structure must be accurate. The crystal structure is fed into a geometry optimisation algorithm in which the net forces acting on the atoms are minimised to find the lowest energy structure. The geometry is judged to be converged when forces acting on the atoms are minimised to below a certain convergence threshold[178]

A key quantity for predicting defect properties is the defect formation energy,

$$E_{\mathrm{d}}^{\mathrm{C}} = E_{\mathrm{T}}^{\mathrm{C}}(\text{defect}) - E_{\mathrm{T}}^{\mathrm{C}}(\text{no defect}), \tag{4.57}$$

where $E_{\mathrm{T}}^{\mathrm{C}}$(defect) and $E_{\mathrm{T}}^{\mathrm{C}}$(no defect) are the total energy of the supercell 'C' with and without the defect of charge z. The defect is formed by removing n_i atoms of chemical potential μ_i. ϵ_F is the Fermi level, measured from the valence band edge ϵ_v.[182]

The defect segregation energy is then taken as the difference between $E_{\mathrm{d}}^{\mathrm{C}}$ in the bulk and at site i.

Classical

Instead of the approach of density functional theory, whereby electrons are modelled explicitly, classical potential-based methods model the attractions and repulsions between atoms in simulation cell using parameterised analytical functions. Classical simulation is based upon the description of the lattice in terms of the Born ionic model, whereby the lattice is constructed from an arrangement of spherical charged ions and the lattice energy U can be calculated as the sum of the pair wise interactions between atoms i and j.[183]

$$U_{ij} = \sum_{ij} \frac{z_i z_j e}{r_{ij}} + \sum_{ij} \Phi_{ij}(r_{ij}) + \dots , \tag{4.58}$$

where the first term defines the long-range electrostatic interactions and the second term defines the short-range two-body interactions. r_{ij} is the distance of separation, z is the ion valence and Φ is the potential.

Long-range interactions The potential of the long-range interactions over pairs of atoms in an infinite lattice takes the form,

$$E = \frac{1}{4\pi\epsilon_0} \frac{1}{2} \sum_{n} \sum_{i=1}^{N} \sum_{j=1}^{N} {}' \frac{q_i q_j}{|r_{ij} + nL|} \tag{4.59}$$

where ϵ_0 is the vacuum permittivity, $r_i j$ is the interatomic separation, L is the lattice vectors representing the periodicity of the cell, and n is an integer used to generate the periodic images of the simulation cell. The factor $\frac{1}{2}$ is introduced to cancel double counting and $'$ is introduced to exclude the term $j = i$ if $n = 0$. The infinite sum converges slowly and conditionally depending on the order of summation.[184]

Ewald Summation Ewald summation was introduced in 1921 as a technique to sum the long-range interactions between atoms and all their infinite periodic images efficiently.[185] This method splits the potential into separate components which converge much quicker than the full expression. The components consist of a term in reciprocal space E_1, a term in real space E_2 and a self-interaction term E_3,

$$E = E_1 + E_2 + E_3. \tag{4.60}$$

The long range interactions are neutralised by surrounding each particle i, with charge

q by a spherical charge distribution of opposite sign, commonly using a Gaussian charge distribution,

$$\rho_i(r) = \frac{q_i \alpha^3}{\pi^{3/2}} \exp(-\alpha^2 r^2). \tag{4.61}$$

where r is the position, relative to the centre of distribution and parameter α controls the width of the Gaussian function. The electrostatic interactions between screened charges can be determined by direct summation in real space,[186]

$$E_2 = \frac{1}{2} \sum_{n} \sum_{i=1}^{N} \sum_{j=1}^{N} \frac{q_i q_j}{4\pi\epsilon_0} \frac{erfc(\alpha|\mathbf{r}_{ij} + \mathbf{n}|)}{|\mathbf{r}_{ij} + \mathbf{n}|}, \tag{4.62}$$

where $erfc$ is the complementary error function,

$$erfc(x) = \frac{2}{\sqrt{\pi}} \int_x^\infty \exp(-t^2) dt. \tag{4.63}$$

A second Gaussian charge distribution is added to the system to calculate the electrostatic interaction of q_i which is not screened. The contributions of this set of charge distributions to the electrostatic potential, E_1, are calculated by summing their Fourier transforms in reciprocal space,

$$E_1 = \frac{1}{2} \sum_{k \neq 0} \sum_{i=1}^{N} \sum_{j=1}^{N} \frac{1}{\pi\lambda^3} \frac{q_i q_j}{4\pi\epsilon_0} \frac{4\pi^2}{k^2} \exp\left(-\frac{k^2}{4\alpha^2}\right) \cos(\mathbf{k} \cdot \mathbf{r}_{ij}). \tag{4.64}$$

E_1 contains the self interaction between the Gaussian charge cloud, which requires it to be subtracted,

$$E_3 = -\frac{\alpha}{\sqrt{\pi}} \sum_{k=1}^{N} \frac{q_k^2}{4\pi\epsilon_0}. \tag{4.65}$$

The three components of the electrostatic interaction can then be summed to give the overall Coulombic interaction.

Parry Summation Ewald summation is used for systems with periodicity in three-dimensions. Parry summation is an adaptation of Ewald summation, which considers the crystal as a series of infinitely sized charged planes. The electrostatic interactions are

summed as vectors parallel and perpendicular to the plane, which requires that $k = 0$ must be evaluated as it can not be assumed that the sum of the charges on the plane is equal to zero.[186]

Short-range interactions The short-range forces that interact between the atoms in a system are described using simple parameterised analytical functions, consisting of repulsive and attractive terms. At very short distances the proximity of electron clouds between two species will cause the repulsive forces to dominate the interaction. However, as the species are separated, attractive Van der Waals forces become more significant.[186]

Lennard-Jones Potential The Lennard-Jones potential is a simple representation of the interatomic interaction model. Due to its computational simplicity, the Lennard-Jones potential is used extensively in computer simulations even though more accurate potentials exist.

$$U(r_{ij}) = 4\epsilon \left[\left(\frac{r_0}{r} \right)^{12} - \left(\frac{r_0}{r} \right)^{6} \right], \tag{4.66}$$

where ϵ is the depth of the potential well, r_0 is the separation at which the potential crosses zero.[174] The first term describes the Pauli repulsive forces due to overlapping electron orbitals, which dominate at short range, and the second term describes the attractive Van der Waals dispersion forces which dominate at longer separations.[187]

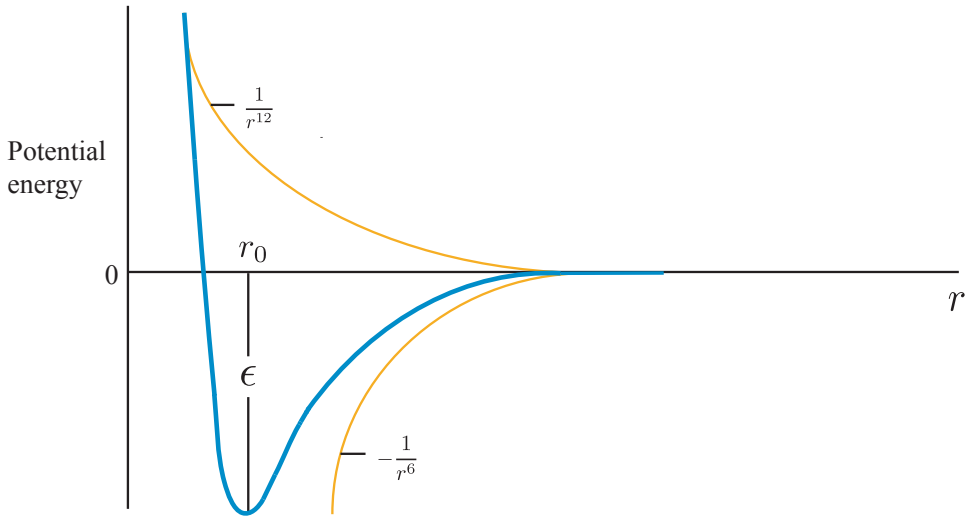

Figure 4.1: Schematic of the Lennard-Jones potential

Morse Potential Another simple and widely used representation of the interatomic interaction model used for covalently bonded interactions is the Morse potential.

$$U(r_{ij}) = \epsilon(1 - \exp -\beta(r - r_e))^2, \tag{4.67}$$

where r is the internuclear distance, r_e is the bond length, and β is related to the curvature of the slope of the potential energy,

$$\beta = \pi v_e \sqrt{\frac{2\mu}{\epsilon}}, \tag{4.68}$$

where v_e is the vibrational constant and μ is the reduced mass.

Calculating defect formation energies The classically derived defect segregation energies used in this work are calculated using METADISE, a computer program designed for modelling grain boundaries. METADISE focuses on two dimensional surfaces and therefore the long-range interactions are evaluated using Parry summation. The short-range interactions are evaluated using a combination of the Morse potential and the repulsive part of the Lennard-Jones potential.

Individual defect segregation energies are calculated by introducing a defect at a site, relaxing the structure and recalculating the lattice energy. In the same way as using density functional theory, the defect formation energy is taken as the difference between the lattice energy of the perfect crystal, and the lattice energy of the defective crystal,

$$E_{\mathrm{d}}^{\mathrm{C}} = E_{\mathrm{T}}^{\mathrm{C}}(\text{defect}) - E_{\mathrm{T}}^{\mathrm{C}}(\text{no defect}). \tag{4.69}$$

Advantages and disadvantages

First principles calculations offer high levels of accuracy, which increase further depending on the choice of exchange correlation functional, however the improved accuracy comes with a extremely high computational cost which limits the size of the simulation cell significantly. A prevalent issue with a limited simulation cell is having sufficient screening between a defect inserted at a site and the 'bulk-like' region. Classical calculations are relatively less accurate, and are only as accurate as the choice of potential model, but considerably computationally cheaper. The lower computational expense allows a significantly larger cell to be simulated, increasing confidence that the defects extend into the

'bulk-like' region, and all relevant interactions have been considered.

4.2.3 Grain Boundary Modelling

Periodic

To calculate the properties of macroscopic materials through explicit treatment of every electron in the system using density functional theory would be extremely computationally expensive and therefore not feasible. Crystalline solids are characterised by a repeating periodic arrangement of atoms, which allows the system to be modelled as a repeating infinite unit cell using periodic boundary conditions.

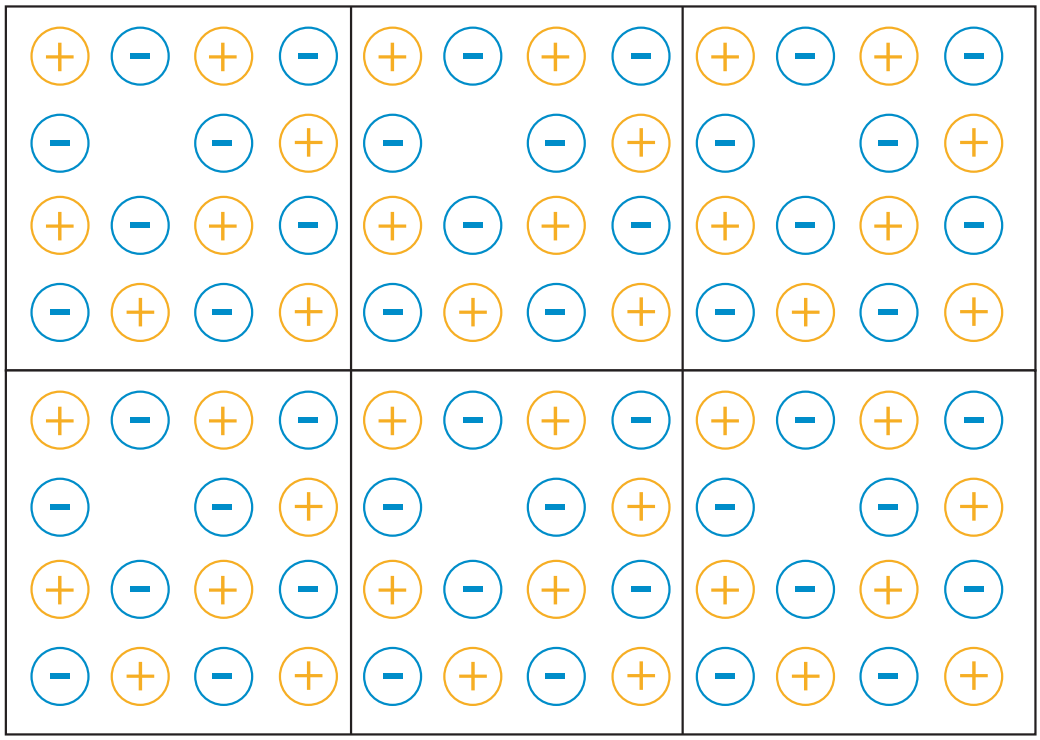

Figure 4.2: Example periodic boundary conditions shown as repeating unit cells of a crystal structure.

Due to the repeating nature of the structure of crystalline materials, any quantity of interest$X$, that depends on position r will be periodic,

$$X(r) = X(r + R), \tag{4.70}$$

where $R = nx + ny + nz$ with n an integer and x, y and z unit cell vectors. Bloch's theorum states that for any wave function that satisfies the Schrodinger equation, there

exists a wave vector K, such that translation by R is equivalent to multiplying the wave function by phase factor $\exp(iK \cdot R)$,

$$\Psi_K(r + R) = \Psi_K(r) \exp(iK \cdot L). \tag{4.71}$$

Non-periodic

The inclusion of a defect into a perfect lattice will cause a perturbation to the surrounding ions. The lattice can be described using the multi-region Mott-Littleton approach.[188] The lattice is partitioned into concentric spherical regions with a defect in the center.

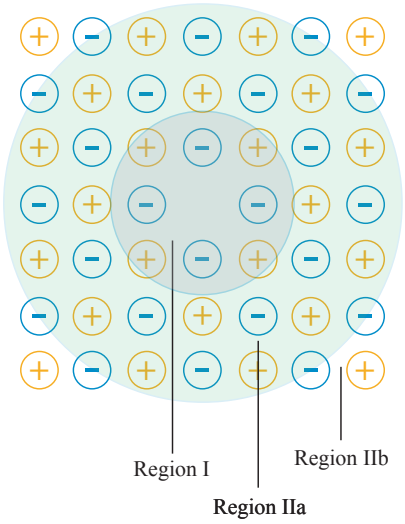

Figure 4.3: Schematic of how the ions in different regions are treated when implementing a Mott-Littleton approach

The region of ions directly surrounding the defect, in region I, are treated explicitly and their positions are adjusted by direct calculation of their interatomic potentials. Region II exists beyond region I and is divided into two further subregions. In region IIa the ions are displaced using the Mott-Littleton approximation, which considers the region as a polarised dielectric continuum,[189]

$$P = \frac{q}{4\pi r}\left(1 - \frac{1}{\epsilon}\right). \tag{4.72}$$

Where P is the crystal polarisation. The ions in region IIb are fixed and assumed to be sufficiently screened as to be completely unaffected by the presence of the defect.[190]

While this approach is most commonly used as a method for calculating defect forma-

tion energies, it can be applied to the modelling of a grain boundary, as implemented in METADISE. Each crystal structure each side of the grain boundary is taken as a block, which is divided into the regions I and II. In region I the ions are allowed to relax to their equilibrium positions and are treated explicitly. In region IIb, the ions are treated with the Mott-Littleton approximation and in region IIb the ions are fixed. The energies for the blocks are calculated as a sum of all the interactions with all of the regions.[191]

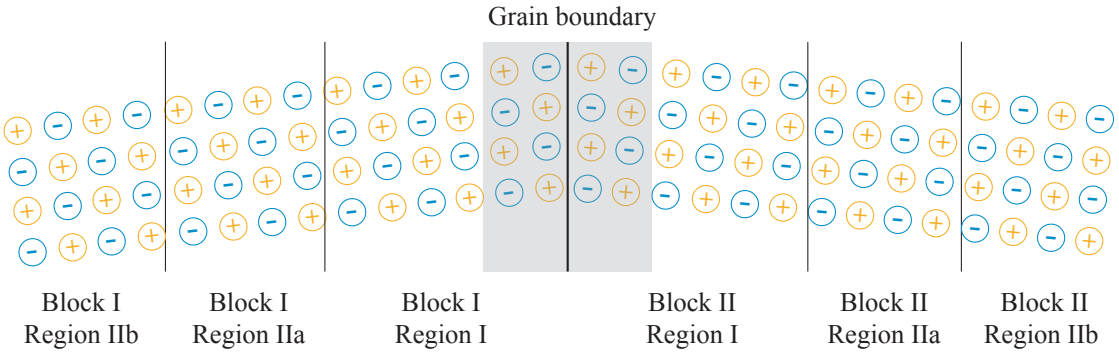

Figure 4.4: Schematic of how the ions in different regions surrounding a grain boundary are treated when implementing a Mott-Littleton approach

Advantages and disadvantages

The use of periodic boundary conditions is conceptually simple; after translation R, the properties of an ion are repeated. However, the size of the unit cell must be considered. The unit cells must be large enough that the distance between the ion of interest are sufficiently separated as to not have any influence over one another, increasing the computational expense of the simulation. Non-periodic Mott-Littleton modelling is more difficult to implement, but the computationally cheap nature of the simulations allow the calculation cell to extend well into the bulk. Grain boundaries could be modelled using a combination of first principles and classical models, such as QM/MM (quantum mechanics / molecular mechanics). Theoretically, using a technique such as QM/MM would allow a small region in close proximity to the grain boundary to be treated explicitly using density functional theory, followed by a region treated explicitly using classical interatomic potentials and beyond this, a region treated as a polarised dielectric continuum.

4.3 Solving the Poisson-Boltzmann equation

In this work, the Poisson-Boltzmann second order partial differential equation is solved using a second order finite difference approximation.

4.3.1 Finite difference approximation

Regular grid

The principle of finite difference methods consists of approximating the differential operator by replacing the derivatives in the equation using difference quotients. The difference quotient for function f is

$$\frac{f_{x+h} - f_x}{h} \tag{4.73}$$

The partial derivatives in the partial differential equation are approximated from neighbouring values using Taylor's theorem. Equation 4.74 shows the leading terms of the Taylor expansion used to expand the second order derivative in the Poisson equation.

$$f_x = f_{x-1} + f'_{x-1} \cdot \Delta x + \frac{f''_{x-1} \cdot \Delta x^2}{2!} + ... \tag{4.74}$$

On a regular grid we approximate f'_{x-1} as $\frac{f_{x+1} - f_{x-1}}{2\Delta x}$ Equation 4.74 becomes:

$$f_x = f_{x-1} + \frac{f_{x+1} - f_{x-1}}{2\Delta x} \cdot \Delta x + \frac{f''_{x-1} \cdot \Delta x^2}{2} \tag{4.75}$$

Substituting Φ in as f, using site i instead of position x yields equation 4.76:

$$\Phi_i = \Phi_{i-1} + \frac{\Phi_{i+1} - \Phi_{i-1}}{2\Delta x} + \frac{-\rho \cdot \Delta x^2}{2} \tag{4.76}$$

As ρ_i is the negative second derivative of Φ_i as described by the Poisson equation:

$$\nabla^2 \Phi_i = -\rho_i = \frac{\frac{\Phi_{i+2} - \Phi_i}{2\Delta x} - \frac{\Phi_i - \Phi_{i-2}}{2\Delta x}}{2\Delta x} \tag{4.77}$$

If we use $x \pm \frac{1}{2}$ instead of $x \pm 1$ the equation simplifies to:

$$\nabla^2 \Phi_i = -\rho_i = \frac{\Phi_{i-1} - 2\Phi_i + \Phi_{i+1}}{\Delta x^2} \tag{4.78}$$

To find the solution of the discretised Poisson-Boltzmann equation, equation 4.78 must be satisfied at all points on the grid. Therefore, these equations become a system of linear

algebraic equations solved using matrix inversion. Matrix inversion is known as the process of finding matrix b which satisfies the equation of an invertible matrix A.

$$\mathbf{b} = A \cdot \mathbf{x} \tag{4.79}$$

In this case, to solve the Poisson equation:

$$A = \Phi_{i-1} - 2\Phi_i + \Phi_{i+1} \tag{4.80}$$

and

$$\mathbf{b} = -\rho \Delta x^2 \tag{4.81}$$

Irregular grid

The sites described are the one-dimensional projection of defects in a crystal lattice onto a grid. In real crystals, lattice sites are not necessarily equally spaced and therefore the finite difference equations must be defined to take into account different Δx spacings.

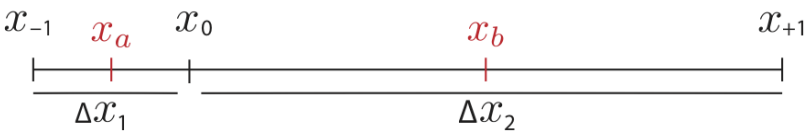

Figure 4.5: Schematic of implementing a finite difference approximation on an irregular grid and how each Δx value is taken from the grid.

For an irregularly space grid, the first derivatives are given as,

$$f'_{x,a} = \frac{f_{x0} - f_{x-1}}{\Delta x_1}, \tag{4.82}$$

$$f'_{x,b} = \frac{f_{x1} - f_{x0}}{\Delta x_2}, \tag{4.83}$$

and the second derivative is given as

$$f_0'' = \frac{f'_{x,b} - f'_{x,a}}{\frac{1}{2}(\Delta x_1 + \Delta x_2)}. \tag{4.84}$$

This can be expanded using the full expression for $f'_{x,a}$, and rearranged,

$$f_0'' = \frac{2(\Delta x_2(f_{x0} - f_{x-1}) - \Delta x_1(f_{x+1} - f_{x0}))}{\Delta x_1 \Delta x_2(\Delta x_1 + \Delta x_2)}. \tag{4.85}$$

Taking the second derivative finite difference at every point in $[x_0, x_2]$ then gives the following expression.

$$f_0'' = \frac{-2}{\Delta x_1 \Delta x_2(\Delta x_1 + \Delta x_2)}.[\Delta x_2 f_{x-1} - (\Delta x_1 + \Delta x_2)f_0 + \Delta x_1 f_{x+1}] \tag{4.86}$$

To solve the Poisson-Boltzmann equation, the function at each position is the electrostatic potential and the second derivative is solved to calculate the charge density at each position. Substituting Φ and ρ yields the equation

$$-\rho = \frac{-2}{\Delta x_1 \Delta x_2(\Delta x_1 + \Delta x_2)}.[\Delta x_2 \Phi_{x-1} - (\Delta x_1 + \Delta x_2)\Phi_0 + \Delta x_1 \Phi_{x+1}] \tag{4.87}$$

To find the solution of the discretised Poisson-Boltzmann equation, the above expression must be satisfied at all points on the grid. Therefore, these equations become a system of linear algebraic equations solved using matrix inversion. Matrix inversion is known as the process of finding matrix b which satisfies the equation of an invertible matrix A.

Taking prefactor (p) as:

$$p = \frac{-2}{\Delta x_1 \Delta x_2(\Delta x_1 + \Delta x_2)} \tag{4.88}$$

A as:

$$A = \Delta x_2 \Phi_{x-1} - (\Delta x_1 + \Delta x_2)\Phi_0 + \Delta x_1 \Phi_{x+1} \tag{4.89}$$

and b as:

$$b = -\rho \tag{4.90}$$

The Poisson-Boltzmann equation can be solved.

The invertible matrix A becomes:

$$A = \begin{pmatrix} (\Delta x_i + \Delta x_{i+1}) & \Delta x_{i+1} & 0 & 0 & 0 \\ \Delta x_i & (\Delta x_i + \Delta x_{i+1}) & \Delta x_{i+1} & 0 & 0 \\ 0 & \Delta x_i & (\Delta x_i + \Delta x_{i+1}) & \Delta x_{i+1} & 0 \\ 0 & 0 & \Delta x_i & (\Delta x_i + \Delta x_{i+1}) & \Delta x_{i+1} \\ 0 & 0 & 0 & \Delta x_i & (\Delta x_i + \Delta x_{i+1}) \end{pmatrix}$$

To account for the prefactor, a new matrix L is constructed. L is created by transposing matrix A, multiplying it by the prefactor and then transposing the matrix again.

$$L = (A^T.p)^T \tag{4.91}$$

Vector b is created from values of ρ

$$b = \begin{pmatrix} \rho_1 \\ \rho_2 \\ \rho_3 \\ \rho_4 \\ \rho_5 \end{pmatrix}$$

$\Phi = L^{-1}b$ is solved using "'numpy.linalg.solve"' which gives Φ_{new}. This process is iterated until a preset convergence limit between is met.

To control numerical stability in reaching the convergence limit, a damping factor is used to reduce the jump in values of Φ between iterations.

$$\Phi_{i+1} = \alpha\Phi_{i+1} + (1.0 - \alpha)\Phi_i \tag{4.92}$$

4.3.2 Calculating grain boundary resistivities and activation

When considering the resistivity profile at grain boundaries, the direction of measurement is naturally important. Measurement perpendicular to the grain boundary is often highly ionically resistive, whereas measurement parallel to the grain boundary is often highly ionically conductive. If the crystal is considered as a continuum, the resistivity is obtained by integrating over the distance L_{x}. For the case of perpendicular resistivies,

$$r^{\perp} = \int_0^{L_{\mathrm{x}}} \sigma_{\mathrm{x}}^{-1} d\mathrm{x}, \tag{4.93}$$

and in the case of parallel resistivity,

$$r^{\parallel} = \frac{1}{\int_0^{L_{\mathrm{x}}} \sigma_{\mathrm{x}} d\mathrm{x}}, \tag{4.94}$$

where σ is the conductivity. When the crystal is considered explicitly, the resistivity can be calculated by direct summation over the sites. The perpendicular and parallel grain boundary resistivity can be evaluated using the defect distributions calculated from the Poisson-Boltzmann equation. Taking the resistivity ρ as

$$\rho = \frac{1}{\sigma} = \frac{1}{c\mu z}, \tag{4.95}$$

where c is the defect concentration, μ is the mobility and z is the defect charge.

Parallel resistivity

Treating each site as a resistor in parallel, the parallel grain boundary resistivity can be calculated by inverting the ratio of the conductivity at the grain boundary sites, compared to the conductivity in the bulk.

$$\sigma_{GB}^{\parallel} = \frac{\sum_{\mathrm{x}} \sigma_{i,\mathrm{x}}}{\sigma_{i,\infty}} = \frac{\sum_{\mathrm{x}} (c_{i,\mathrm{x}} \mu_i z_i / \Delta \mathrm{x}_i)}{(c_{i,\infty} \mu_i z_i / \Delta \mathrm{x}_{\infty})}, \tag{4.96}$$

Assuming constant mobility for the mobile defect across the space charge regions, the grain boundary resistivity can be simplified,

$$\sigma_{GB}^{\parallel} = \sum_{\mathrm{x}} \left(\frac{c_{i,\mathrm{x}}}{\Delta \mathrm{x}_i} \right) \times \left(\frac{\Delta \mathrm{x}_{\infty}}{c_{i,\infty}} \right), \tag{4.97}$$

and the parallel grain boundary resistivity,

$$r_{GB}^{\parallel} = \frac{1}{\sigma_{GB}^{\parallel}}. \tag{4.98}$$

Perpendicular resistivity

Treating each site as a resistor in series, the perpendicular grain boundary resistivity can be calculated by taking the ratio of the sum of the resistivity at the grain boundary sites, compared to the resistivity in the bulk,

$$r_{GB}^{\perp} = \frac{\sum_{\mathrm{x}} \rho_{i,\mathrm{x}}}{\rho_{i,\infty}} = \frac{\sum_{\mathrm{x}} \frac{1}{\sigma_{i,\mathrm{x}}}}{\frac{1}{\sigma_{i,\infty}}} \tag{4.99}$$

$$r_{GB}^{\perp} = \frac{\sum_{\mathrm{x}} (\Delta \mathrm{x}_i / c_{i,\mathrm{x}} \mu_i z_i)}{(\Delta \mathrm{x}_\infty / c_{i,\infty} \mu_i z_i)} \tag{4.100}$$

Assuming constant mobility for the mobile defect across the space charge regions, the grain boundary resistivity can be simplified,

$$r_{GB}^{\perp} = \left(\frac{c_{\infty,\mathrm{x}}}{\Delta \mathrm{x}_\infty} \right) \times \sum_{\mathrm{x}} \left(\frac{\Delta \mathrm{x}_i}{c_{i,\mathrm{x}}} \right). \tag{4.101}$$

Resistivity scaling term

For particles on a lattice, that only interact through volume exclusion, the mobility exhibits a 'blocking' term,[192]

$$\mu = \mu'(1 - x_i), \tag{4.102}$$

where x_i is the defect mole fraction. The inclusion of the 'blocking' term results in the mobility no longer being considered a constant and therefore the resistivity ratio must be considered in the unsimplified form shown in equation 4.100.

Activation energy

The calculated grain boundary resistivity can be used to calculate the grain boundary contribution to an ionic conductivity activation energy. In a bulk material, the ionic conductivity increases with temperature, numerically differentiating the logarithmic resistance with respect to the temperature gives a linear Arrhenius plot with a slope of $\frac{E_{act}}{k}$.[193] Grain boundaries are often a source of additional resistance in a system and therefore when a grain boundary is introduced, the change in conductivity with respect to temperature also changes. The activation energy discussed here is the effect on the microscopic energy

barrier for a single defect to jump one site with the addition of a grain boundary, given by,

$$E_{\text{act}} = \frac{\mathrm{d} \ln r_{\text{GB}}}{\mathrm{d} \frac{1}{kT}}. \tag{4.103}$$

Chapter 5

Comparison of 1D Poisson-Boltzmann models

5.1 Background

5.1.1 Theoretical Space Charge Models

As discussed in chapter 4, there are various methods and models used for calculating space charge properties in solid electrolytes. The most common of which is to use continuum modelling (where point defects are assumed to exist in a continuum dielectric and modelled using a regular grid, i.e. "coarse-graining" any atomic scale structure for the system being modelled) and to solve the Poisson-Boltzmann equation using fixed boundary conditions in the bulk and defining an input parameter at grain boundary core. These models provide conceptually simple and computationally cheap methods for analysing the space charge properties. Alternatively the space charge properties are calculated using atomistic methods such as molecular dynamics or Monte-Carlo techniques to examine the relationship between the crystal structure, defect distributions and ionic conductivities.[84–87] While direct atomistic methods might be expected to be more reliable, they are conceptually more complex, computationally expensive and have the problem of simulating large enough systems in a true equilibrium. Integrated atomistic–continuum models are becoming more prevalent, whereby the Poisson-Boltzmann model is parameterised using data derived from atomistic calculations, but these models are implemented using different methods by different studies. These methods vary based on how the system is presented spatially. Most models assume the crystal structure behaves as a continuum,

whereas the Poisson-Boltzmann solver used in this work can take into account explicit defect positions. The definition of the grain boundary core is also presented differently in various models, as there is no explicit computational definition for the region that should be considered at the grain boundary core. The different core representations lead to potentially less accurate solutions of the space-charge properties due to the full effect of the grain boundary not being considered in the space-charge model. It is therefore important to understand how these different representations of the system affect the calculated space charge properties.

5.1.2 Definition of the grain boundary core

The grain boundary core is represented in varying ways in different space charge models. The typical approach is to treat the grain boundary core as a single layer with either a fixed space charge potential (implicit core), or with a defined defect segregation energy (explicit core). The grain boundary typically extends over a number of lattice spacings in the crystal structure, and therefore there is scope to extend the input data to give a more physical representation of the grain boundary core. This chapter gives a comparison of explicit core space charge models where the grain boundary core is associated with defect segregation energies, used as the Poisson-Boltzmann input parameter to calculate the space-charge properties.

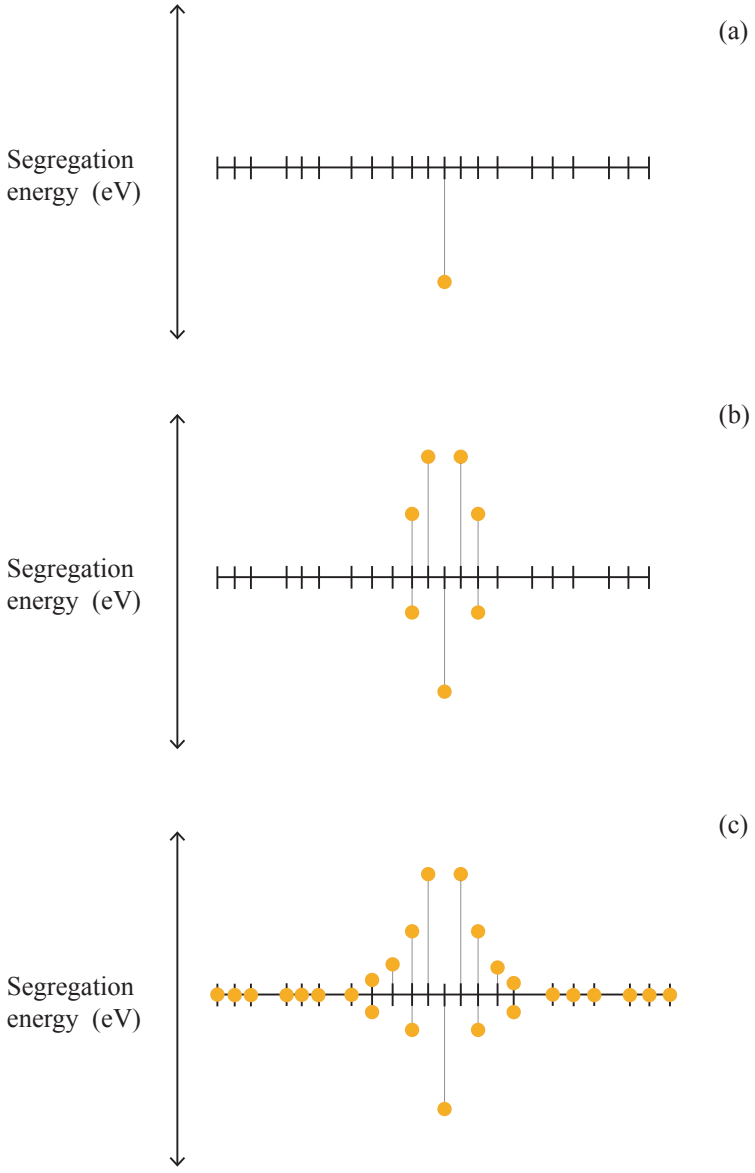

Figure 5.1: Example explicit core models, with segregation energies defined. (a) depicts the single core values, (b) depicts layered core values and (c) depicts all site values.

Single core value

The most conceptually simple explicit core space charge model defines the grain boundary core using a single defect segregation energy,[164–166] which is used to calculate the potential at the grain boundary core and the electrostatic potential profile into the bulk. All other defect sites in the crystal are assumed to have a segregation energy of 0.0 eV. This approach assumes that the grain boundary core is negligibly thin and does not account for any structural distortion in the grain boundary compared to the crystal bulk.

Layered core values

A more advanced space charge model, termed the "layer-by-layer" approach by Wahnstrom and co-workers[172] considers the grain boundary core as a set of layers. For a given layer, there may be more than one inequivalent defect position, and so defects might have more than one segregation energy at that x coordinate. The "layer-by-layer" approach averages over these in each layer. The grain boundary core is defined as the region where the segregation energies are "significant" and similarly to the single value model, the segregation energies outside of this region are fixed to 0.0 eV.

All site values

Further detail can be incorporated into the model by removing the assumption that the system behaves as a continuum by modelling on a regular grid. This model includes all defect segregation energies calculated from the grain boundary core into the bulk at explicit defect positions. This method avoids the arbitrary distinction between the grain boundary core and space-charge regions. The structural inconsistencies and defect segregation data is included at every site from the grain boundary through to the bulk, where the defect segregation energies naturally decay to value 0.0 eV with increasing distance from the grain boundary, as shown in figure 5.2.[88]

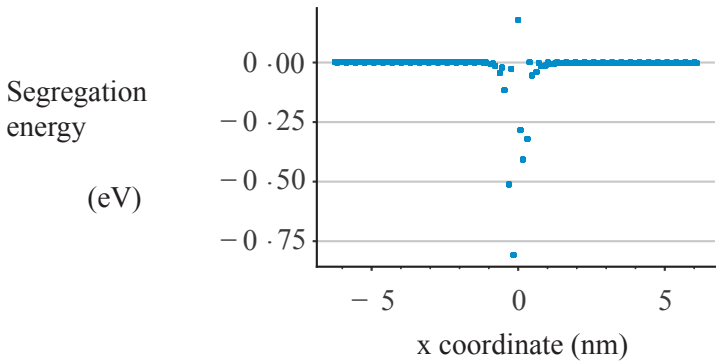

Figure 5.2: Segregation energies for the (111) grain boundary in Gd-doped CeO_2, calculated using classical interatomic potentials.

5.2 Modelling

At the present time, there is no existing study of how the choice of model, including whether the model is continuum or site explicit and how the grain boundary core is defined effects the calculated space charge properties. The Poisson-Boltzmann model implemented by PYSCSES code and used in all the work presented in this thesis offers the ability to model space charge formation using either a continuum or a site explicit basis and include any definition of the explicit core model, including modelling the grain boundary core as either a single point, a region of "significant" defect segregation energies, or not have a defined grain boundary core region at all, instead using calculated defect segregation energies at all defect positions.

5.2.1 Continuum grain boundary models

Grain boundaries can be modelled using a continuum approach, whereby the system is treated as a continuum dielectric and the Poisson-Boltzmann equation is solved on a regular grid. To implement a continuum approach to modelling grain boundaries, the Poisson-Boltzmann solver used in this work takes a minimum and maximum value for the calculation region and divides it into equally spaced sites based on a user-defined number of points, from the explicit core model defined the potential can then be calculated at each of the grid points. If the user wants to include segregation energies at all sites, but model these as a continuum, the defect segregation energies defined at explicit defect positions from atomistic calculations can be interpolated onto the regular grid allowing each defect to be present at each grid point as a continuum and allowing the Poisson-

Boltzmann equation to be solved using a finite difference approximation at each of the regularly spaced grid points.

5.2.2 Site explicit grain boundary models

To implement a site explicit approach to modelling grain boundaries, the explicit defect positions and defect segregation energies calculated from atomistic calculations at each site in the crystal structure are projected on to a 1D grid, as shown in figure 5.3 and then used as the input for the model. This allows the Poisson-Boltzmann equation to be solved at each site using a finite difference approximation on an irregular grid (discussed in more detail in section 4.3.1), and prevents defects from being located at sites that they would not occupy in the real crystalline structure.

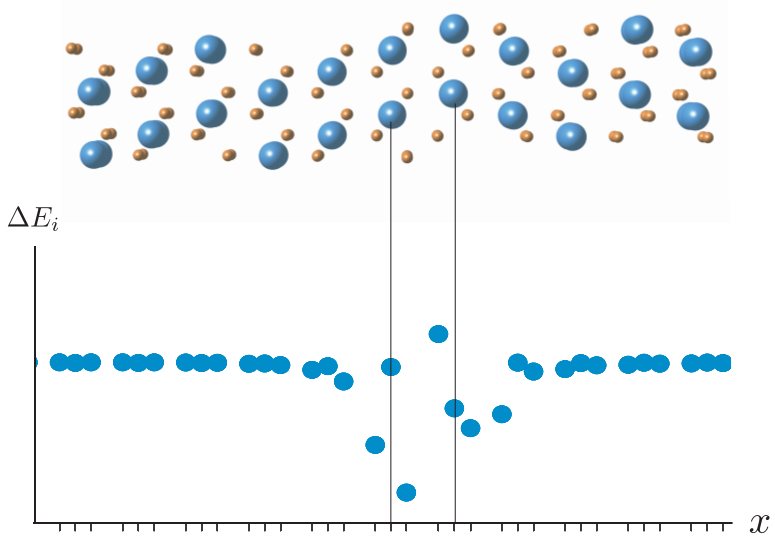

Figure 5.3: Segregation energies for the (111) grain boundary in Gd-doped CeO_2 are mapped onto a one-dimensional grid to be used as the input for PYSCSES.

5.2.3 Definition of the grain boundary core

As previously discussed, in the literature, there are two commonly used explicit core definitions, a single core value or layered core values. The third model used in the comparison includes all lattice site points and defect segregation energies, although PYSCSES is the first solver to implement that condition. These three models are implemented in PYSCSES to generate the results in this thesis. To implement a single core value, the defect segregation energy at a defect position of 0.0 nm (where the two surfaces have been joined to create a grain boundary during the atomistic calculations) is taken and the defect segregation energies at all other sites are fixed to 0.0 eV. To implement a layered core, the

defect segregation energies are analysed and those close to the grain boundary core, are included in the calculation and the defects segregation energies at sites outside of this region are fixed to 0.0 eV. For a layered core, there is no standard definition for how many layers to include in the core, and where to consider the boundary between "core" and "bulk" layers. For the analysis, we have considered "thermally significant" segregation energies as defining the core, i.e. layers with segregation energies $|E_{seg}| > kT$. Finally to implement a model using all site values, the data remains unaltered and the Poisson-Boltzmann equation is solved including segregation energies at every site.

5.3 Comparison of models

The ability to vary the model and definition of the grain boundary core allows a comparative study of the calculated space charge properties and how the results vary with the choice of model. Other significant parameters that can be incorporated into the model include Mott-Schottky and Gouy-Chapman approximations, whereby certain defects are considered immobile, or all defects are considered mobile respectively and inclusion of the charge for the non-defective species at each site. For this comparison of different explicit core grain boundary models, we have considered the (111) grain boundary in Gd-doped CeO_2, with a dopant concentration of 20% at a temperature of 1000 °C. We use Gd-doped CeO_2 as a model system for testing the effects of the different explicit site models exclusively in this chapter, the effects of space charge formation in the material will be discussed in chapter 6. As pure CeO_2 is aliovalently doped with Gd, the Gd substitutes the Ce ions creating a substitutional Gd defect with a net -1 charge. For every two Ce ions substituted, an oxygen vacancy ($V_O^{\bullet\bullet}$ is formed with a net +2 charge, maintaining charge neutrality. Figures 5.4 and 5.5 show the electrostatic potential and defect mole fraction profiles across the space charge region for all of the possible combinations of model and approximation implemented in PYSCSES.

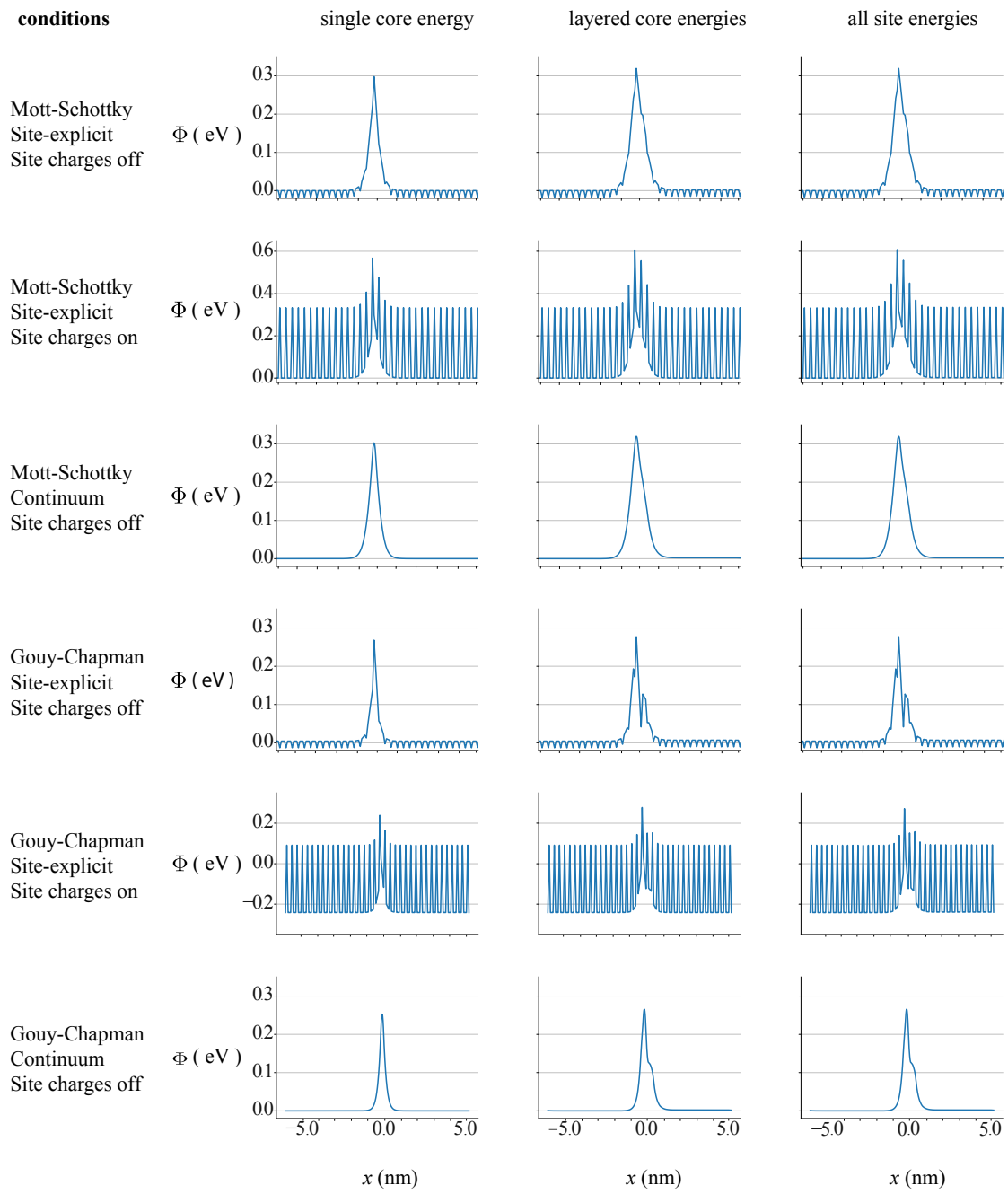

Figure 5.4: The electrostatic potential profile given for each of the combinations of modelling techniques over the grain boundary region.

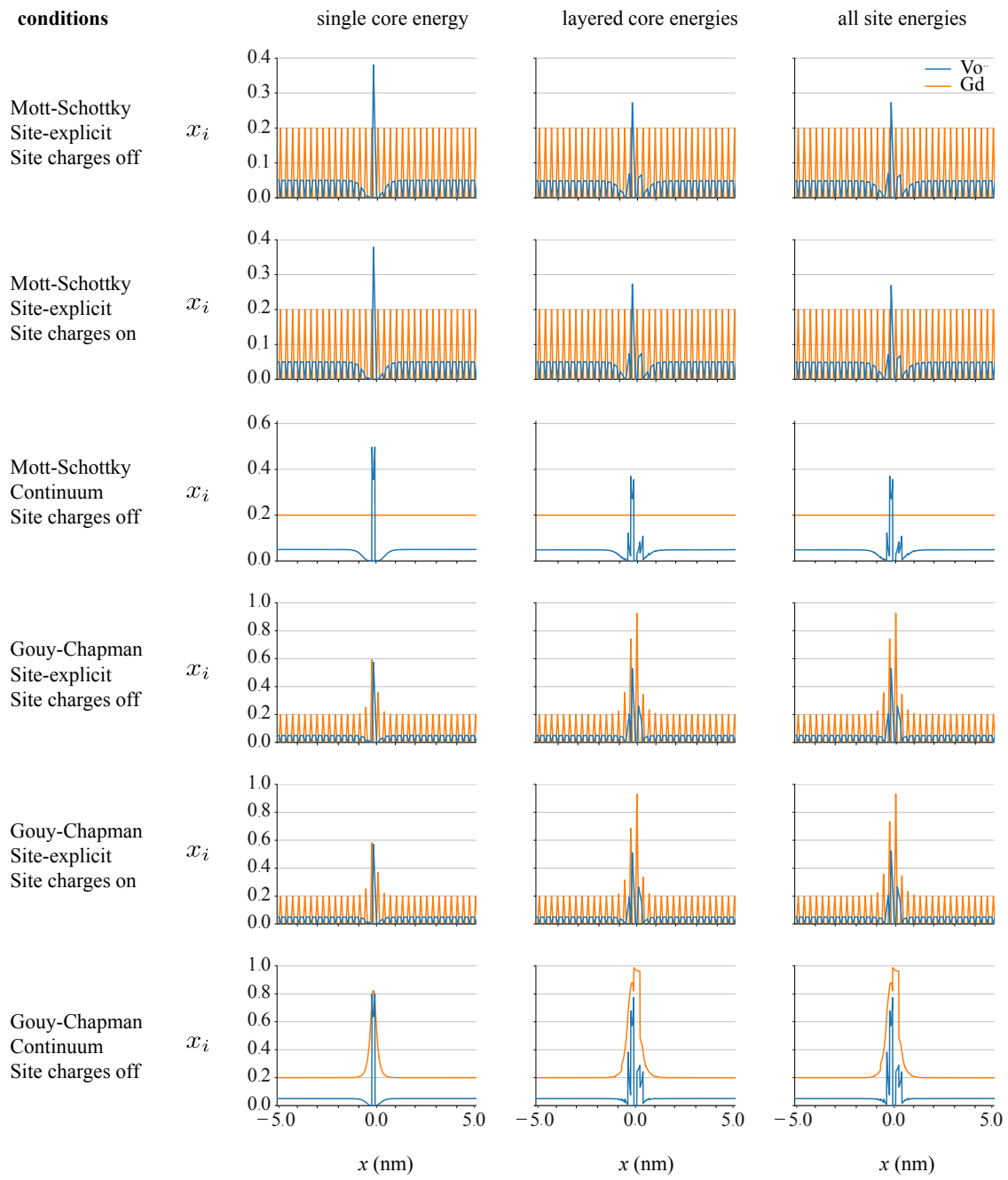

Figure 5.5: The defect distribution given for each of the combinations of modelling techniques over the grain boundary region.

5.3.1 Three main explicit core models

The two main explicit core models found in the literature include the use of a continuum model with a single core segregation energy and a continuum model with a core described using layered segregation energies. The third explicit core model discussed is a novel site explicit model using all segregation energies implemented using PYSCSES. For gadolinium doped ceria, at typical operating temperatures and conditions it is usually assumed that intrinsic dopant ions are immobile and thus a Mott-Schottky condition has been used (although Gouy-Chapman conditions are considered in section 5.3.2), and there is not a significant effect when including the charge of the non-defective species at each site (shown in section 5.3.3). This narrows the full combination data down to three conditions that can be exclusively compared.

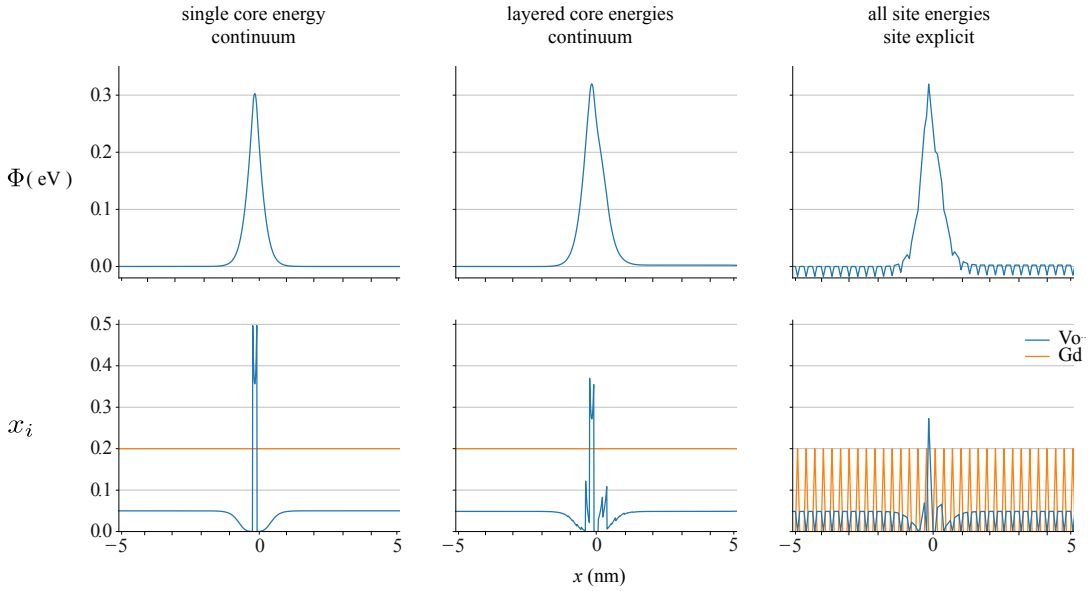

Figure 5.6: The electrostatic potential profile and defect distribution profile over the grain boundary region for the three most prevalent space charge models, a single point grain boundary, a layered grain boundary and a non-defined grain boundary.

Figure 5.6 shows the potential and defect distributions for the three main space charge models, continuum with a single core segregation energy, continuum with layered core segregation energies, and site explicit with all segregation energies. It can be seen from the potential profiles that there is not a significant change in the calculated space charge potential (the electrostatic potential at the grain boundary core) between the models, with space charge potential values of 0.303 eV, 0.320 eV and 0.319 eV, respectively. Within the analytical Mott-Schottky model (discussed in section 3.2.4, the space charge properties

are entirely defined by the space charge potential, which would suggest that properties such as the defect distribution would be the same in all three cases. However, it can be observed from the defect distribution profiles that there is a significant variation in the defect concentrations, particularly in the grain boundary core. For the continuum model with a single core segregation energy, the $V_O^{\bullet\bullet}$ mole fraction in the core is 0.479, for the continuum model with layered core segregation energies, the $V_O^{\bullet\bullet}$ mole fraction in the core is 0.378 and for the site explicit model using all segregation energies the $V_O^{\bullet\bullet}$ mole fraction in the core is 0.274. Therefore we observe a 42.7% reduction in the concentration of oxygen vacancies which segregate to the grain boundary core between the models.

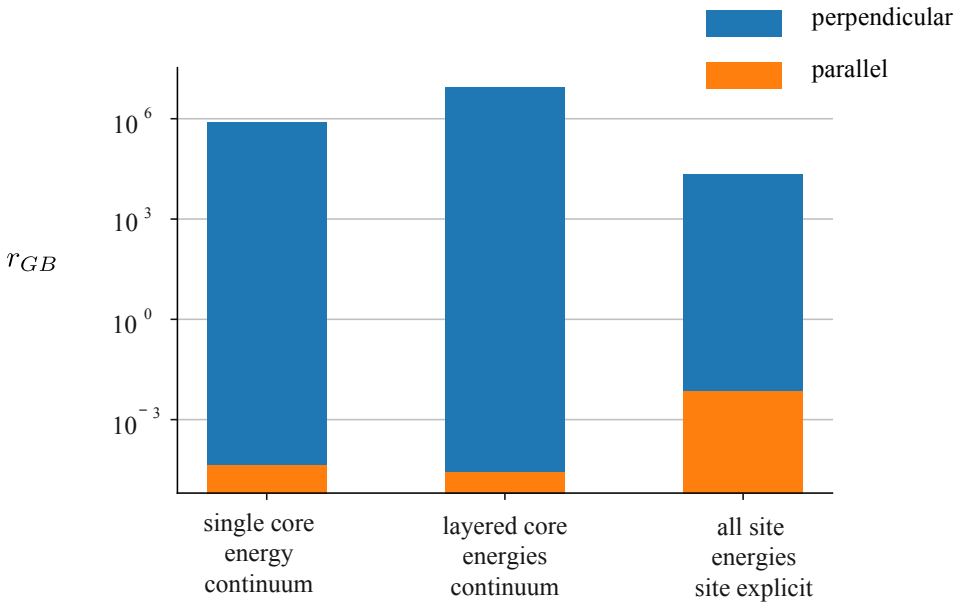

Figure 5.7: The calculated resistivity ratio for the grain boundary region for the three most prevalent space charge models, a single point grain boundary, a layered grain boundary and a non-defined grain boundary.

The defect concentrations obtained through solving the Poisson-Boltzmann equation can be used to calculate the resistivity (discussed in more detail in section 4.3.2),

$$\rho_{i,x} = \frac{1}{\sigma_{i,x}} = \frac{1}{c_{i,x}\mu_i z_i}, \tag{5.1}$$

and the resistivity ratio relative to the bulk system (the grain boundary resistivity), $r_{\mathrm{GB}} = \frac{\rho_{i,x}}{\rho_{i,\infty}}$.

As the grain boundary resistivity is dependant on the defect concentration, the large variation in defect concentration results in a large variation in the calculated grain boundary resistivity. Shown in figure 5.7, the continuum model with a single core segregation energy exhibits a perpendicular resistivity ratio of 7.9×10^5, and a parallel resistivity ratio of 4.4×10^{-5} the continuum model with layered core segregation energies exhibits a resistivity ratio of 8.9×10^6 and a parallel resistivity ratio of 2.7×10^{-5}, and the site explicit model using all segregation energies exhibits a perpendicular resistivity ratio of 2.1×10^4 and a parallel resistivity ratio of 7.2×10^{-3}.

The perpendicular grain boundary resistivity can be used to calculate the grain boundary contribution to an ionic conductivity activation energy by calculating r_{GB} across a range of temperatures and then using the Arrhenius relationship,

$$E_{\mathrm{act}} = \frac{\mathrm{d} \ln r_{\mathrm{GB}}}{\mathrm{d}\left(\frac{1}{kT}\right)}. \tag{5.2}$$

Shown in 5.8, the continuum model with a single core segregation energy shows a calculated ionic conductivity activation energy of 0.581 eV, the continuum model with layered core segregation energies shows a calculated ionic conductivity activation energy of 0.808 eV and the site explicit model with all segregation energies shows a ionic conductivity of 0.730 eV.

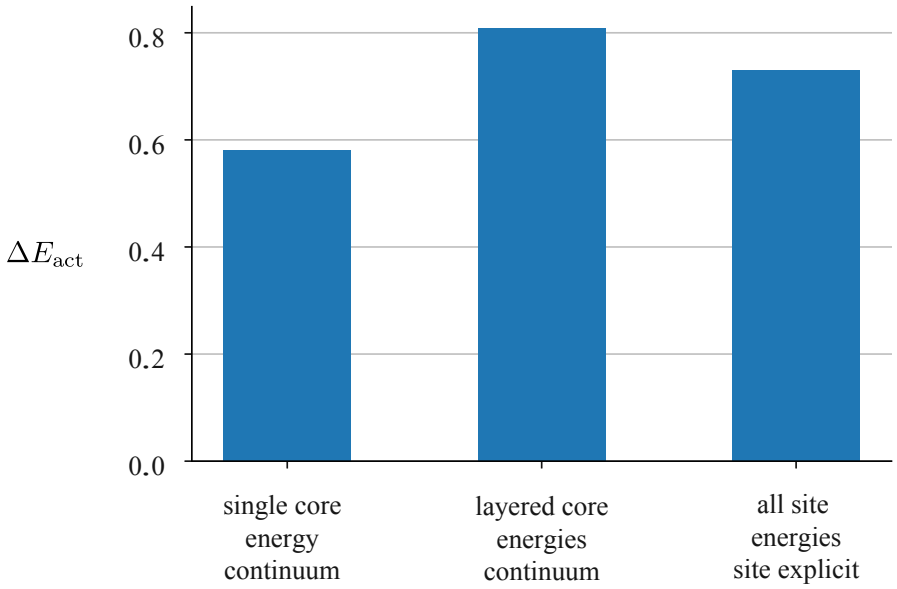

Figure 5.8: The calculated activation energy for the grain boundary region for the three most prevalent space charge models, a single point grain boundary, a layered grain boundary and a non-defined grain boundary.

The explicit definition of the grain boundary core is not well defined for parameterising space charge models, and therefore it is important to consider the large effect in calculated space charge properties between the explicit site models. In conventional analytical models, the space charge potential determines the space charge properties of the system, so one would expect that as the space charge potential insignificantly differs between the models, the variation in other space charge properties would be largely unaffected. However, the comparison of the space charge properties show a large variation in the oxygen vacancy mole fraction and subsequently the grain boundary resistivities and activation energies. This large variation in key parameters of solid electrolyte performance between the commonly used single layer explicit site model and the novel site explicit model is significant to understanding defect behaviour at grain boundaries in solid electrolytes and suggests that space charge properties are potentially over, or underestimated depending on the type of defect segregation. More accurate analysis of the defect behaviour and subsequently space charge properties is imperative to solid electrolyte design as an overestimation in grain boundary resistivity could result in a promising material being dismissed.

5.3.2 Mott-Schottky vs. Gouy-Chapman approximations

As discussed in section 3.2.3, defects present in a system can be allowed to redistribute to their equilibrium positions or fixed to their bulk concentrations. If only one defect is considered is allowed to redistribute and the others are fixed to their bulk concentrations, the model implements a Mott-Schottky approximation, and if all of the defect species are allowed to redistribute, the model implements a Gouy-Chapman approximation, these approximation expressions are used as shorthand for the redistribution conditions described. To compare the differences between these two cases, PYSCSES has the ability to recalculate all the defect mole fractions on each iteration of the solver, effectively allowing all defects to redistribute to their equilibrium positions, or to fix certain defined defect species to their bulk defect mole fractions (or any given mole fraction) on each iteration of the solver updating only the defect mole fractions of the defects allowed to redistribute. In gadolinium doped ceria, it is typically assumed that under standard operating temperatures, the gadolinium defects are not able to redistribute through the structure, therefore it is common to assume a Mott-Schottky approximation. If both defect species are free to redistribute, it would be expected that the gadolinium defects would redistribute to the space charge regions adjacent to the grain boundary core, due to electrostatic interactions. This should increase the screening of the charged grain boundary core into the bulk, reducing the space charge potential and narrowing the space charge region.

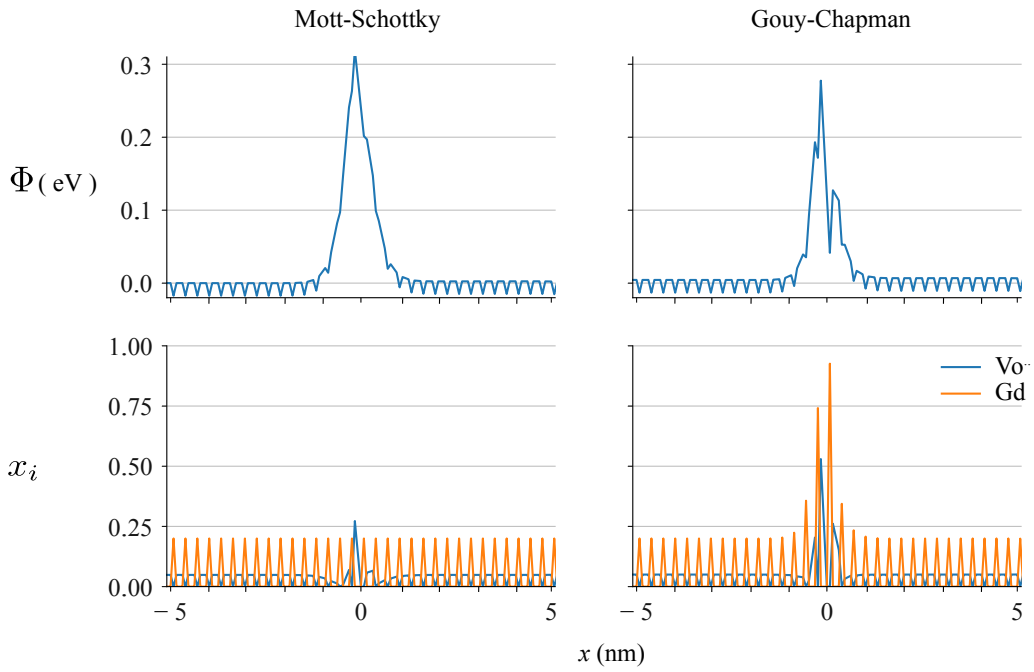

Figure 5.9: A comparison of the calculated electrostatic potential and defect distribution profile when running the calculation under Mott-Schottky and Gouy-Chapman conditions, using the site explicit core model for the (111) grain boundary orientation of Gd-doped CeO_2 at 1000 K and 20 % Gd concentration.

It can be seen from figure 5.9 that the space charge profile exhibits the expected behaviour when Gd defects are able to redistribute through the structure. The gadolinium ions redistribute to the regions adjacent to the grain boundary core due to the electrostatic interactions between the positively charged grain boundary core and the net -1 charged gadolinium ions. This results in an increased occupancy of oxygen vacancies in the grain boundary core from 0.274, to 0.531 and a reduction in the space charge potential from 0.319 eV under Mott-Schottky conditions, to 0.285 eV under Gouy-Chapman conditions due to the additional charge screening.

5.3.3 Inclusion of site charges

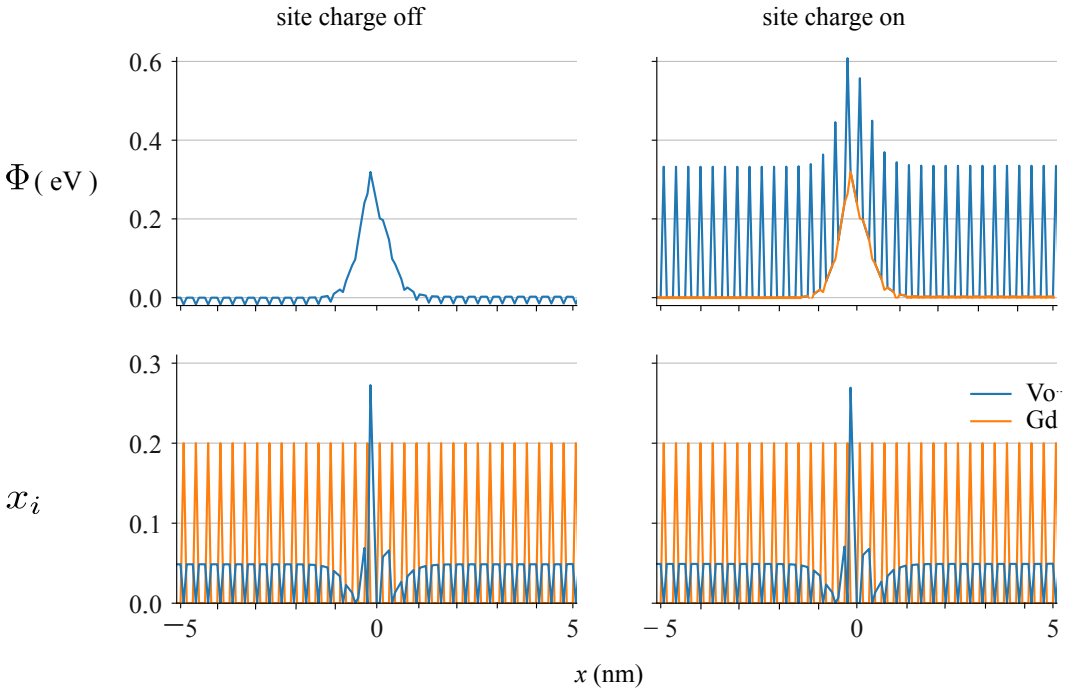

Figure 5.10: A comparison of the calculated space charge properties when running the simulation including the site charge of the non-defective species, using the site explicit core model for the (111) grain boundary orientation of Gd-doped CeO_2 at 1000 K and 20 % Gd concentration.

Normal Poisson-Boltzmann type models just consider the relative charge of the defects, with the charge of the reference sites averaged out to zero. This is not the case in real materials, where the charges of atoms mean even a perfect crystal may not have a perfectly flat electrostatic potential profile. This is handled in PYSCSES by calculating the overall charge at each site as $Q_x = q_a + x_{i,x} z_i e$, where Q is the overall site charge at position x, q is the relative charge of ion a, x_i is the mole fraction of defect i and z is the relative charge of defect i. Figure 5.10 compares the electrostatic potential and defect mole fractions calculated with and without the charge of the reference sites. It becomes evident that the space charge properties are largely unaffected when the charge of the non-defective species at each site are incorporated. While there are considerable oscillations in the potential profile when the site charge is included, the space charge potential is calculated as 0.319 eV and 0.320 eV for excluding or including the site charge respectively. The oxygen vacancy mole fraction is calculated at 0.274 and 0.269 respectively.

5.4 Conclusions

The space charge properties have been compared for varying space charge models, including continuum vs. site explicit, different definitions of the grain boundary core, Mott-Schottky and Gouy-Chapman analysis and inclusion of the charge for the non-defective species at each site. The results indicate that the choice of model can strongly affect the results from the space charge calculations. The results between site explicit and continuum models show that this distinction does not have a large impact on the calculated space charge potential, although the site explicit data does allow oscillations in the potential profile due to the explicit crystalline structure. The oxygen vacancy mole fraction however is reduced significantly in the site explicit case compared to the continuum model. The choice of grain boundary core definition also does not have a large effect on the calculated space charge potential, but the oxygen vacancy mole fraction varies significantly between the different explicit cores. This large variation is oxygen vacancy concentration at the grain boundary core leads to a large variation in the grain boundary resistivities observed suggesting that the choice of explicit grain boundary is significant and that the segregation energy at sites outside of the thermally significant segregation energies should be considered. The space charge potential is affected as expected with Mott-Schottky and Gouy-Chapman conditions with the space charge potential profile being reduced and narrowed in the Gouy-Chapman case due to the increased electrostatic shielding from the redistributed gadolinium ions and it was found that including charge for non-defective species at each site does not affect the calculated space charge properties. The effect of the choice of model on the calculated defect mole fractions are significant due to the relationship between defect mole fraction and ionic conductivity. A large variation in defect mole fraction corresponds to a large variation in ionic conductivities depending on the choice of model. As ionic conductivity is the most important property for solid electrolytes used in electrochemical devices, it can be argued that it is important to use the model which incorporates segregation energy data at atomically resolved defect positions as this additional information gives more reliable space charge properties.

Chapter 6

Gd doped CeO_2

6.1 Background

6.1.1 CeO_2 as a solid oxide fuel cell material

There has been much interest in oxide materials that can serve as solid oxide ion electrolytes for application to solid oxide fuel cells. The important criteria for this application is a high ionic conductivity in the form of oxygen vacancy migration and a negligible electronic conductivity.[194] CeO_2 (ceria) is a versatile and widespread material used in solid state oxygen transport due to the ease of formation of oxygen vacancies.[195] Much like the commonly used solid oxide fuel cell material zirconia (ZrO_2), ceria is an oxide ion conductor with a fluorite structure. Ceria varies from zirconia in that it undergoes variations in stoichiometry at increased temperatures in a reducing atmosphere,[194] and has a potentially higher ionic conductivity.[196] While pure ceria has a negligible concentration of mobile charge carriers, the concentration of oxygen vacancies, and thus the properties of the material, can be increased by doping the material aliovalently.

6.1.2 Doping CeO_2

Doping of materials is a common technique to increase the concentration of mobile charge carriers in a system. Doping can be isovalent, whereby an ion in the system is substituted with an ion of the same charge, or aliovalent whereby an ion in the system is substituted with an ion of differing charge. Ceria is typically aliovalently doped using a trivalent cation such as gadolinium or yttrium substituted on a cerium site.

$$2\,Ce_{Ce}^{\times} + 4\,O_{O}^{\times} + 2\,Gd \rightleftharpoons 2\,Gd_{Ce}' + 3\,O_{O}^{\times} + V_{O}^{\bullet\bullet} + 2\,Ce$$

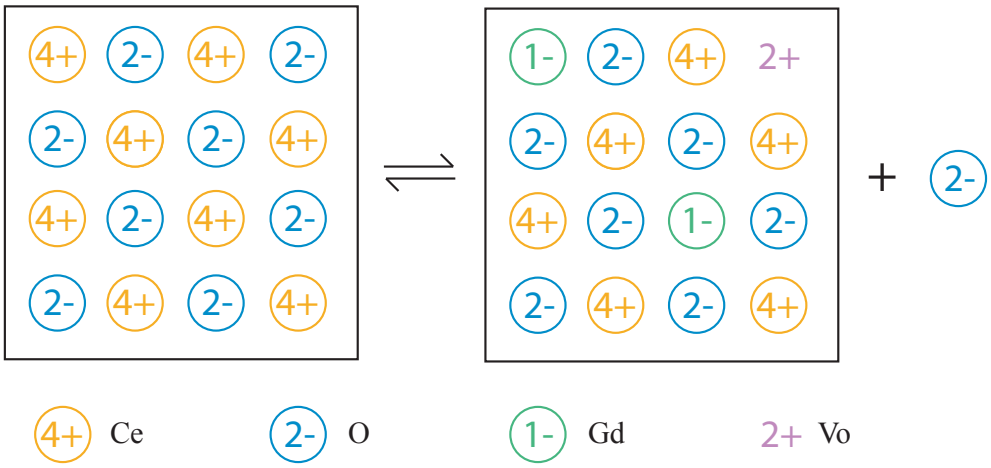

Figure 6.1: The formation of defect pairs in CeO_2 when it undergoes aliovalent doping through the addition of Gd.

As depicted in figure 6.1, this produces a defective site with a net -1 charge. For every two cerium ions replaced with a trivalent cation, an oxygen vacancy is formed maintaining charge neutrality in the system.

Gd-doped CeO_2 is a solid electrolyte that has been the focus of many studies in recent years, due to the higher ionic conductivity compared to the pure phase. Experimental samples of Gd-doped CeO_2 are polycrystalline with grain boundaries separating the different crystalline regions. Understanding the grain boundary defect behaviour in Gd-doped CeO_2 is important to enable optimisation of the material for use in solid oxide fuel cells.

6.1.3 Experimental studies

Experimental analyses of Gd-doped ceria typically focus on fine-tuning the properties of the material, by controlling the point defects in the bulk. Methods for controlling the point defects typically involve varying synthesis conditions when the material is produced, including, but not limited to, variation in temperature, variation in dopant ion concentration and variation in the atmosphere. Sintering temperature is also expected to affect the ionic conductivity of ceria by affecting the distribution of defects.

Gd-doped ceria powders are commonly synthesised using a precipitation method, decomposing $Ce(NO_3)_3\,6\,H_2O$ and $Gd(NO_3)_3\,6\,H_2O$ in an ammonia solution, separated using centrifugation and annealed to decompose traces of ammonium salts.[195,197,198] The powders are then pressed into cylindrical pellets and sintered, resulting in a polycrystalline

sample which can undergo analysis. The sintering temperature of the synthesis procedure can be controlled as a potential route to controlling the defect behaviour. Lower sintering temperatures reduce the size of the individual grains in a sample, reducing the inter-grain boundary distance. The effect of varying inter-grain boundary distance on ionic conductivity is discussed in more detail in chapter 7.

Effect of temperature

The variation in sintering temperature has also been linked to a variation in the electrostatic potential and defect distribution over the grain boundary region. It has been theorised that a higher sintering temperature leads to a redistribution of the gadolinium defects to the regions adjacent to the grain boundary core. At low sintering temperatures, the mobility of the dopant ions can be considered negligible and it can be assumed that there is a uniform dopant distribution across the grain boundary region. Anselmi-Tamburini *et al.*[199] discuss that the low sintering temperature results in a reduced space charge potential, and an eliminated "blocking effect" (typical values of the increase in activation energy due to oxygen vacancies becoming "trapped" due to more favourable segregation energies) for charge carriers in the grain boundary core. Similarly, Bae *et al.* suggested that the use of a high sintering temperature leads to a considerably lower ionic conductivity due to the segregation of dopant ions to the space charge regions, intensifying the space charge effect. In this work Bae *et al.* investigated the effect of the sintering temperature on the ionic conductivity of 20% gadolinium doped ceria. One sample was sintered at 1373 K, and the conductivity measured at 773 K compared to another sample sintered and measured at 773 K. It was found that the sample sintered at 1373 K exhibited a significantly lower ionic conductivity attributed to a greater space charge potential. Overall, higher operating temperature resulted in a higher ionic conductivity due to the mobile charge carriers having more energy to overcome the activation energy for diffusion. This theory is well known with the aim of research into solid electrolytes being to reduce the necessary operating temperature. The effect of an increased sintering temperature consistently exhibits a reduction in the ionic conductivity of the material.

Effect of dopant concentration

The effect of dopant concentrations on space charge properties and ionic conductivities in doped ceria has also been extensively studied experimentally. Avila-Paredes *et al.* produced samples of gadolinium doped ceria at 1, 3, 5, 10, 15 and 20 % dopant concentration

and calculated ionic conductivities using impedance spectroscopy. The results showed that the specific grain boundary conductivity increases rapidly with increasing Gd content and the plateaus at concentrations above 15 %, with a total conductivity close to the bulk conductivity. The calculated grain boundary activation energy ($E_{\mathrm{a,(GB)}}$) was found to decrease from 1.61 eV at 1% Gd to 0.90 eV at 10 % Gd and then begin to increase slightly to 0.93 eV and 1.01 eV at 15 % and 20 % Gd respectively. These authors discuss how the increase in ionic conductivity can almost exclusively be attributed to the reduction in the potential 'barrier' formed at the grain boundaries, which diminishes the blocking effect and decreases the space charge width.

Perez-Coll *et al.* have disagrees with the statement that higher Gd concentrations increase the ionic conductivity in gadolinium doped ceria. In this study, samples were prepared at 5, 10, 20, 30 and 40 % Gd content, and ionic conductivities were calculated using impedance spectroscopy. The results showed that the conductivity in the bulk decreased with increasing Gd content at low temperatures, while the grain boundary conductivity experienced very little variation. These authors speculated that the decrease in ionic conductivity is due to increased interactions between the dopant ions and the mobile oxygen vacancies. However Perez-Coll *et al.* agree that the grain boundary blocking effect is diminished with increasing Gd content. The discrepancy in the suggestions made by Perez-Coll *et al.* and Avila-Parades *et al.* may be explained by the percentage dopant concentrations used in the studies. Perez-Coll *et al.* used significantly greater dopant concentrations than those that Avila-Parades *et al.* argued causes a plateau in the grain boundary conductivity.

Yan *et al.* carried out similar analyses on yttrium doped ceria, creating samples with 10, 15 20 and 25 % Y content. The measured results from the analyses showed that the single grain boundary resistivities decreased, and then increased with increasing dopant content. Yan *et al.* predicted that the variation in grain boundary resistivity was due to increasing dopant content lowering the Schottky barrier height, but also suggested that dopant cations associate with the mobile oxygen vacancies in the structure, resulting in a higher activation energy for oxygen diffusion.

Overall, the results for experimental analysis of dopant concentrations agree that doping pure ceria with a trivalent cation increases the concentration of mobile charge carriers in the system, which slightly counteracts the effect of vacancy segregation to the grain boundary core, reducing the Schottky barrier height. The optimum value for dopant

content is consistently between 10 % and 20 % beyond which the ionic conductivity begins to decrease, due to association between the dopant ions and mobile charge carriers.

6.1.4 Theoretical studies

Theoretical analyses of grain boundary effects in gadolinium doped ceria have consistently predicted that there is an accumulation of oxygen vacancies in the grain boundary core and the formation of space charge in the adjacent regions, and under the condition of sufficient cation mobility the accumulation of acceptor dopants in the space charge zone.[72] Often grain boundary effects and space charge formation are modelled using an analytical Poisson-Boltzmann models, such as the Mott-Schottky and Gouy-Chapman approximations,[147] or a numerical Poisson-Boltzmann model with an experimentally defined space charge potential defining the boundary condition at the grain boundary core.[164] In these previous studies it has been observed that the accumulation of oxygen vacancies at the grain boundary core and resultant formation of space charge regions results in a decreased ionic conductivity in the sample.

Work carried out by Van Laetherm[200] *et al.* implemented a finite element simulation method as a robust and flexible way to calculate bulk and grain boundary conductivities. This method used partial differential equations, similar to how PYSCSES evaluates space charge properties, but on a continuum. From their simulations, Van Laetherm *et al.* find an increased resistivity due to the presence of grain boundaries, however state that their model does not contain enough detail for comparison with direct measurement.

An extension to the Poisson-Boltzmann model (as described earlier in this thesis) was presented by Mebane and De Souza[168] for modelling space charge effects in acceptor doped ceria. They implemented a self-developed Poisson-Cahn approach and their result conform with the wider literature, that the effect of space charge regions negatively impacts the ionic conductivity of the material.

The Poisson-Cahn approach requires parameters that are not accessible through atomistic calculations, but instead rely on experimental data. PYSCSES allows direct computation of site explicit systems, and is an extension of the standard theoretical work that implement Poisson-Boltzmann models, while being conceptually simpler than the Poisson-Cahn approach.

6.2 Effect of grain boundary orientation

Typical space charge analysis considers the explicit grain boundary structure to be insignificant. In experimental analyses, a sample is prepared and the space charge potential is calculated from the measured resistivity data, often obtained using impedance spectroscopy using the Mott-Schottky model (discussed in section 3.2.4). Because a single effective space-charge potential is obtained from this analysis, it is assumed that there is some 'average' behaviour for all grain boundaries present in the sample. However, grain boundaries with different crystallographic orientations have distinctly different structures, and it might be expected that these exhibit different grain boundary behaviour. Although this has been hypothesised, there is no existing comparison of space-charge properties for different grain boundaries in $Gd-CeO_2$.

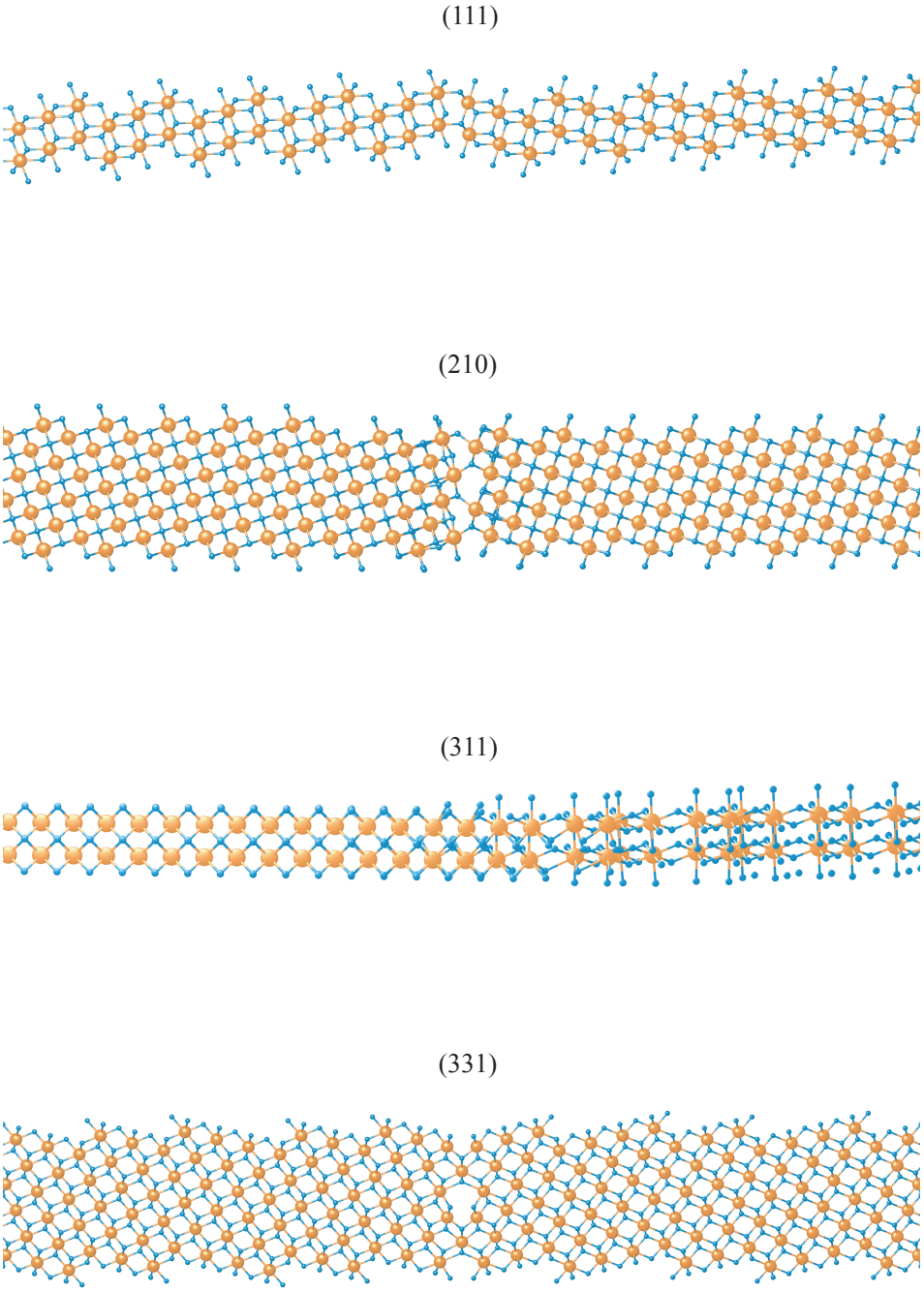

Figure 6.2: The atomistically calculated structurally different grain boundary structures in CeO_2. Shown are the lowest energy structures formed using METADISE, the (111), (210), (311) and (331) orientations.

The PYSCSES code calculates the space charge properties using explicit defect segregation energies and explicit atomistic positions, which allows consideration of the atomic structure

of the grain boundary. Four structurally different grain boundaries with (111), (210), (311) and (331) orientations have been analysed.

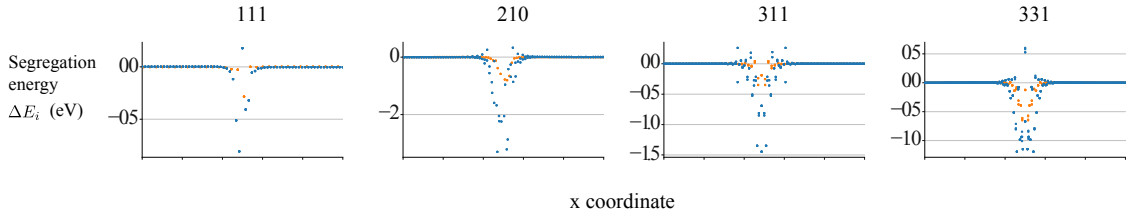

Figure 6.3: The atomistically calculated defect segregation energies for the (111), (210), (311) and (331) grain boundary orientations in Gd-doped CeO_2.

The defect segregation energies and atomistic positions have been calculated using METADISE (described in more detail in section 4.2.2), and input into PYSCSES to calculate the space charge properties.

6.2.1 Space charge properties

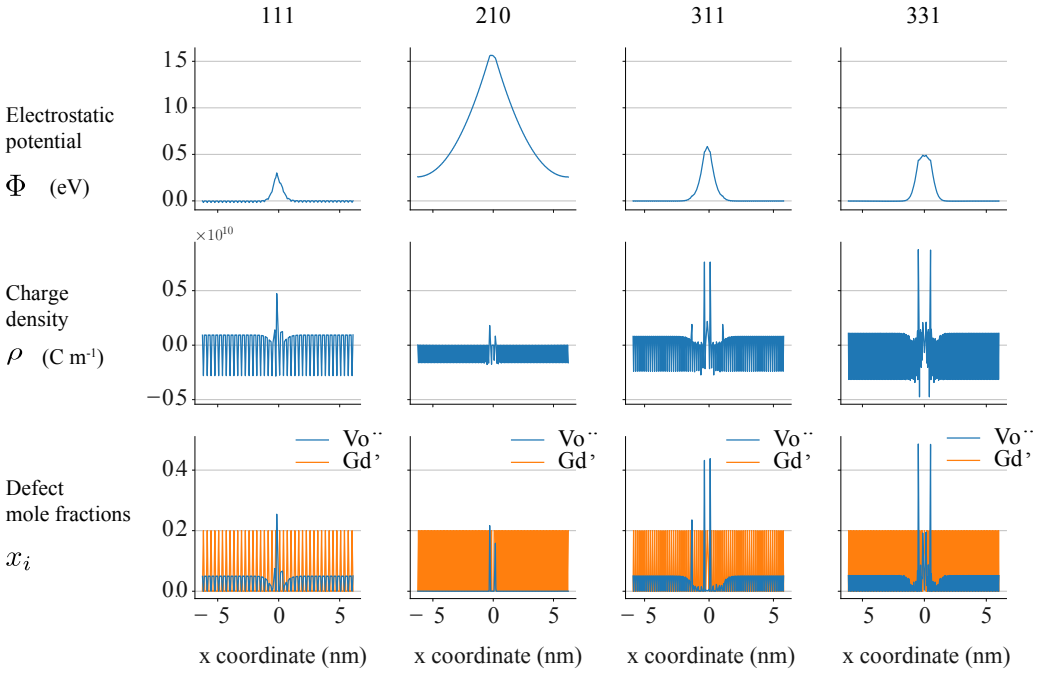

Figure 6.4: Calculated electrostatic potential, charge density and defect distribution profiles for the (111), (210), (311) and (331) grain boundary orientations in Gd–CeO_2 at 1000 K with a dopant concentration of 20 %

Figure 6.4 shows the calculated electrostatic potential, charge density and defect mole fractions over the grain boundary and space charge regions for the four structurally different

Gd-doped CeO_2 grain boundaries at 1000 K, with a gadolinium dopant concentration of 20 %.. It can be seen from figure 6.4 that the space charge properties vary significantly with grain boundary orientation. This is potentially due to the variation in structural disorder experienced in the grain boundary regions. Variation in structural disorder is proportional to the variation in the chemical potential difference between the grain boundary and the bulk. A variation in chemical potential in turn causes a variation in the defect segregation energies, which effects the migration of defects through the grain boundary region. As the magnitude of the defect segregation energies increases, more defects will segregate to the grain boundary and the space charge effects will be enhanced. For each of the grain boundary orientations, the defect segregation energies are negative at the grain boundary core, and therefore defect segregation to the grain boundary core is favourable. This defect segregation can be seen in the space charge property profiles in figure 6.4. The electrostatic potential varies between 0.3 eV for the (111) grain boundary to 0.6 eV for the (311) grain boundary, and there is a distinct charge and accumulation of defects at the grain boundary core, and depletion of defects in the regions adjacent.

It can be noted that the (210) grain boundary has a space charge potential of 1.6 eV. There are issues with the magnitude of the defect segregation energy at the grain boundary core for the (210) grain boundary, whereby it is of such large magnitude that in all simulations the grain boundary core becomes fully saturated by defects, a phenomenon that would be nonphysical in the real system and change the structure of the grain boundary fundamentally. Interactions between point defects in crystals are known to be complex, involving a combination of long range attractive and repulsive forces caused by strain fields and electrostatic effects, and shorter range forces due to local bond relaxation. These interactions determine rates of defect formation, aggregation and dissociation. In a real Gd-doped CeO_2 system, these defect interactions would prevent a situation whereby each site in the grain boundary core is occupied by defects. It can be hypothesised that the introduction of more complex defect-defect interaction terms in the model would allow systems with such high grain boundary defect segregation energies, such as the (210) grain boundary in Gd-doped CeO_2, to be modelled correctly. Alternatively, the structure of the (210) grain boundary may have been produced in error as a low energy grain boundary structure.

6.2.2 Resistivities

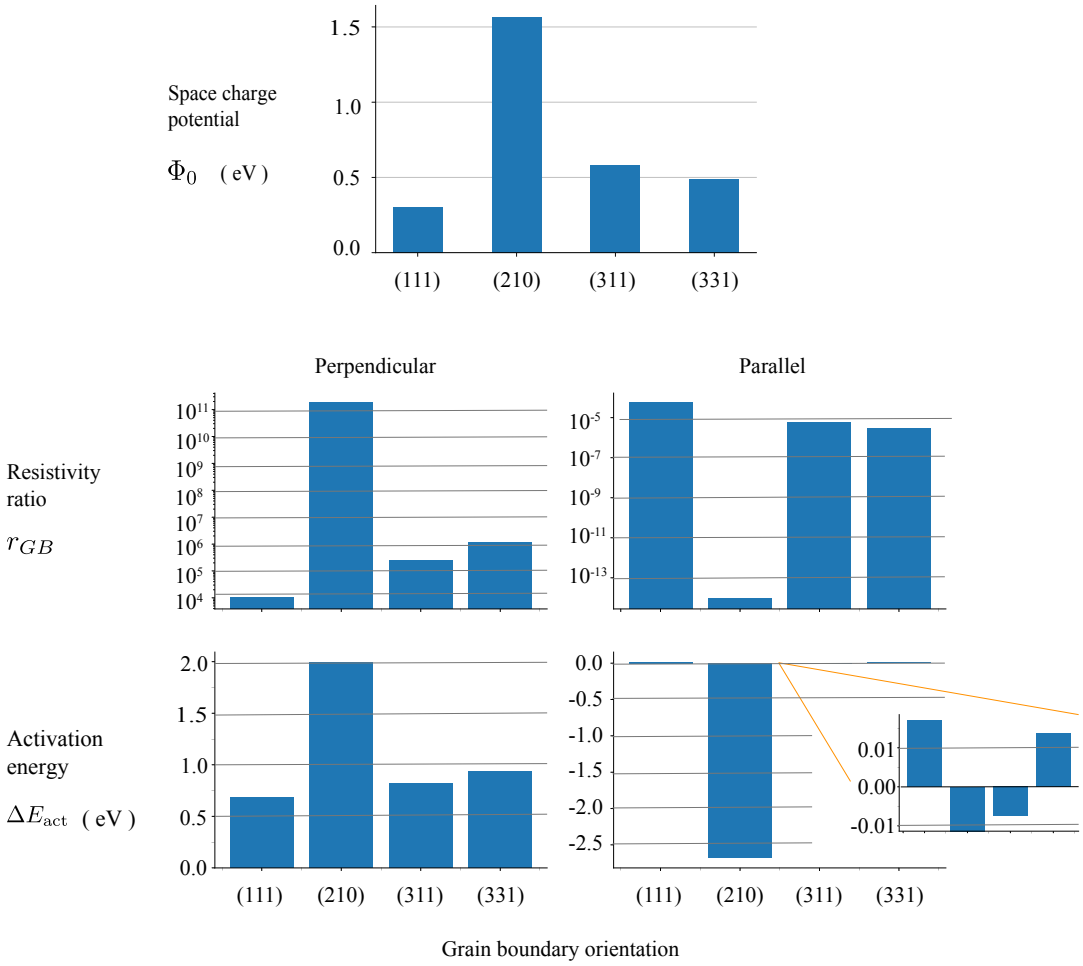

Figure 6.5: Calculated space charge potentials, perpendicular and parallel grain boundary resistivities and perpendicular and parallel activation energies for the (111), (210), (311) and (331) grain boundary orientations in $Gd-CeO_2$.

6.3 Effect of temperature

As discussed in section 6.1.3, the temperature affects the space charge properties and exhibited ionic conductivities of solid electrolytes. To study the effect of temperature, the space-charge calculations were performed at a range of temperatures between 773.15K and 1273.15K to calculate the space charge properties, such as defect distributions and electrostatic potentials, along with grain boundary resistivities for each of the four structurally different grain boundaries. This particular temperature range was chosen because they are the values most commonly found in the literature with 1273.15K as the "current" operating temperature and 773.15K as the "goal" operating temperature for solid oxide

fuel cells.

6.3.1 Space-charge potential

Figure 6.6 shows the calculated electrostatic potential at the grain boundary core over the temperature range 773.15 K to 1273.15 K. It can be seen that there is a slight decrease in the space charge potential as temperature is increased. This decrease in space charge potential is due to oxygen vacancies having the additional energy to overcome the "trapping" of the grain boundary core, resulting in a lower concentration of oxygen vacancies at that point. The lower oxygen vacancy concentration lowers the charge density at the grain boundary core and in turn lowers the space charge potential.

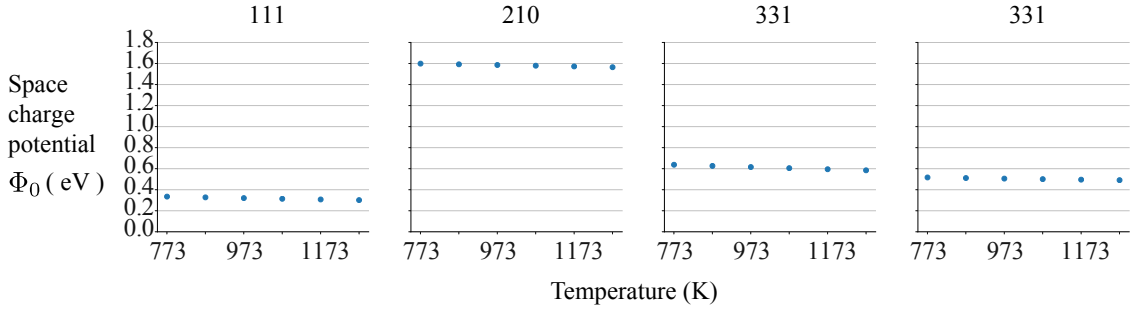

Figure 6.6: Calculated space charge potentials as a function of temperature for the (111), (210), (311) and (331) grain boundary orientations in $Gd-CeO_2$.

6.3.2 Resistivities

The perpendicular grain boundary resistivity ratio decreases with increasing temperature as shown in figure 6.7. The change in perpendicular resistivity ratio over the temperature range varies from 2 orders of magnitude for the (311) grain boundary to 4 orders of magnitude for the (210) grain boundary. The perpendicular activation energy also decreases as temperature is increased.

The parallel grain boundary resistivity ratio decreases with increasing temperature as shown in figure 6.8. The change in parallel resistivity ratio over the temperature range varies from no change in order of magnitude for the (111) and (331) grain boundaries to 6 orders of magnitude for the (210) grain boundary. The grain boundary activation energy once again decreases with increasing temperature.

As with the space charge potential, the grain boundary resistivities decrease with increasing temperature because there is a lower concentration of oxygen vacancies at the grain boundary core at higher temperatures, reducing the effective charge of the grain boundary

and reducing the depletion of oxygen vacancies in the space charge region. As the resistivity is inversely proportionate to mobile charge carrier concentrations, naturally as the depletion is reduced in the space charge region, the resistivity is lower. The lower grain boundary resistivity then reduces the grain boundary activation energy.

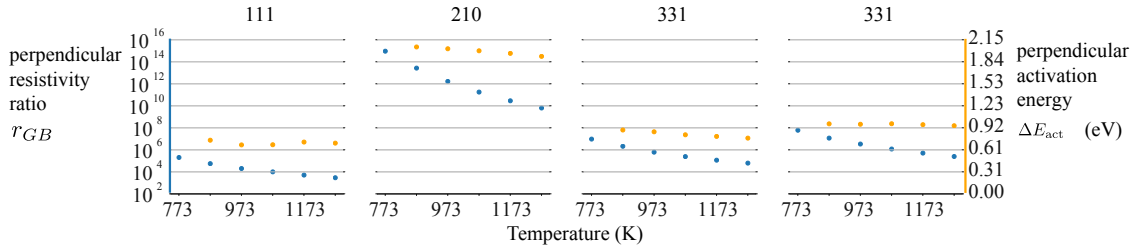

Figure 6.7: Calculated perpendicular grain boundary resistivities and activation energies as a function of temperature for the (111), (210), (311) and (331) grain boundary orientations in $Gd-CeO_2$.

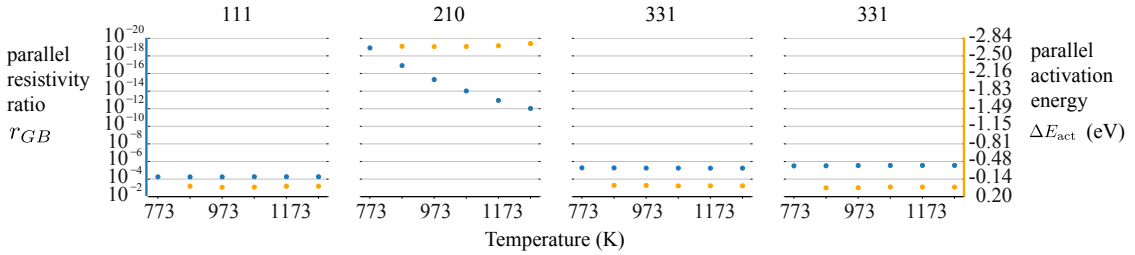

Figure 6.8: Calculated parallel grain boundary resistivities and activation energies as a function of temperature for the (111), (210), (311) and (331) grain boundary orientations in $Gd-CeO_2$.

6.3.3 Effect of sintering temperature

As described in the introduction to this chapter, experimental studies on the effect of varying sintering temperature for polycrystalline Gd-doped CeO_2 have suggested that changing the sintering temperature changes the experimentally measured grain boundary resistivity. At typical intermediate-temperature solid oxide fuel cell operating temperatures, Gd_{Ce} is not expected to be mobile on an experimental timescale, so Gd_{Ce} distributions are fixed. Under sintering conditions however, the temperature is much higher and therefore Gd_{Ce} is expected to be more mobile and may redistribute. These high temperature Gd_{Ce} profiles will then be "frozen in" when the system is cooled to operating temperatures.

The ability to "fix" dopant ions to their bulk defect distributions given in PYSCSES allowed these observations to be measured theoretically. This effect is implemented by

using two sequential space charge calculations. In the first, both defects species are able to redistribute at a high temperature (1273.15 K) and in the second, the Gd_{Ce} defect concentrations are fixed and the calculation in run allowing only $V_O^{\bullet\bullet}$ to redistribute. The temperatures used for this calculation were chosen based on the work carried out by Bae *et al.*, investigating the effect of sintering temperature experimentally.

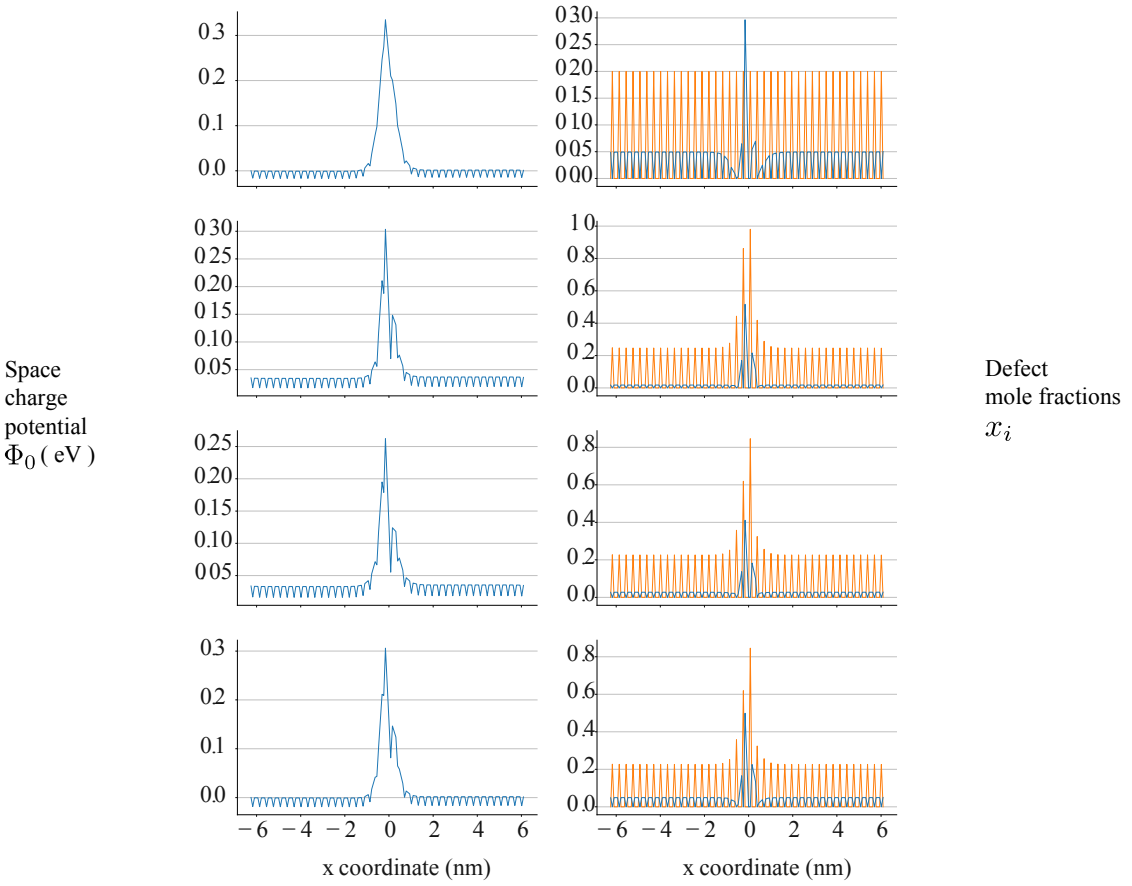

Figure 6.9: Calculated space charge potential and defect mole fractions as a function of sintering conditions for the (111) grain boundary orientation in $Gd-CeO_2$.

Figure 6.9 (a) shows the electrostatic potential and defect distributions at 773.15 K with the gadolinium ions fixed to their bulk defect distribution and exhibits a space charge potential of 0.34 eV. Figure 6.9 (b) shows the electrostatic potential and defect distributions at 773.15 K with all of the defects able to redistribute to their equilibrium positions and exhibits a space charge potential of 0.30 eV. Figure 6.9 (c) shows the electrostatic potential and defect distributions at 1273.15 K with all of the defects able to redistribute to their equilibrium positions and exhibits a space charge potential of 0.26 eV. Finally figure 6.9 (d) shows the electrostatic potential and defect distributions at 773.15 K with the gadolinium ions fixed to the redistribute profile calculated at 1273.15 K and exhibits a space charge potential of 0.31 eV. From figures 6.9 (a) and (d), we can compare the

effect of a sample being sintered and operated at 773.15 K and a sample being sintered at 1273.15 K and operated at 773.15 K. The electrostatic potential profile is lowered from 0.34 eV to 0.30 eV which is an 11.8 % reduction in the space charge potential due to the redistribution of defects at the higher sintering temperature, as predicted by Bae *et al.*

The same analysis of sintering temperature has also been computed for the (311) and (331) grain boundaries as shown in figure 6.10. The same for conditions of 773.15 K with Gd fixed to bulk, 773.15 K with all defects able to redistribute, 1273.15 K with all defects able to redistribute and 773.15 K with Gd fixed to the 1273.15 K distribution has been computed and can be seen in figure 6.10. To focus specifically on the effect of sintering temperature, only the first and last conditions are explicitly compared.

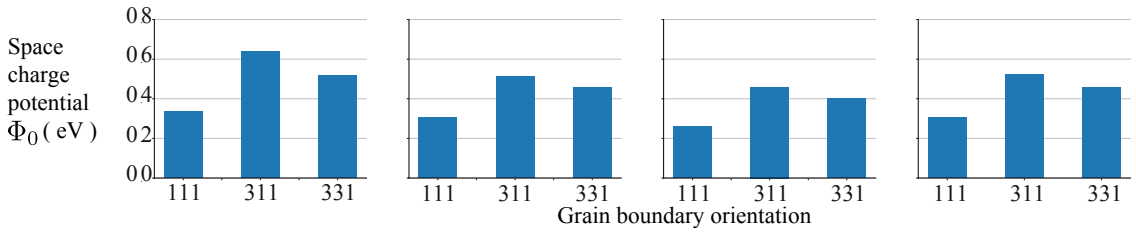

Figure 6.10: Calculated space charge potential as a function of sintering conditions for the (111), (311) and (331) grain boundary orientation in Gd$-CeO_2$.

The results in figure 6.10 show that sintering at high temperature and cooling to an intermediate operating temperature causes the space charge potential to be reduced relative to sintering at an intermediate operating temperature for all three grain boundary orientations. This is attributed to segregation of Gd_{Ce} to the space charge regions at high temperature as proposed by Bae *et al.*. This segregation of dopant ions decreases the net charge density in the grain boundary core, and weakens the space-charge formation effect. A smaller depletion region is formed, leading to a smaller grain boundary resistance.

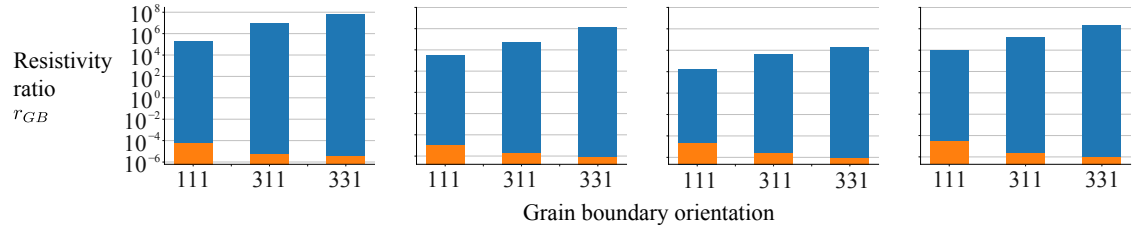

Figure 6.11: Calculated parallel and perpendicular resistivities as a function of sintering conditions for the (111), (311) and (331) grain boundary orientations in Gd$-CeO_2$.

Figure 6.11 shows the calculated parallel and perpendicular grain boundary resistivities for the (111), (311) and (331) grain boundaries. The results show that sintering at high

temperature results in a reduction in both parallel and perpendicular grain boundary resistivity compared to sintering at an intermediate temperature. This reduction is up to 2 orders of magnitude for the perpendicular resistivity. As discussed for the space charge potential, this is attributed to the redistribution of Gd_{Ce} to the space charge regions, reducing the space charge effect. The effective charge at the grain boundary core is weakened resulting in less oxygen vacancy depletion in the space charge regions. As resistivity is inversely proportionate to the concentration, the reduced depletion leads to a reduced grain boundary resistivity.

6.4 Effect of dopant mole fraction

As discussed in the introduction to this section, experimental analyses suggest that the dopant concentration can have a large impact on the space charge properties and ionic conductivities in Gd-doped CeO_2. PYSCSES has been used to calculate the space charge properties, such as electrostatic potentials and grain boundary resistivities for each of the four structurally different grain boundaries at 4 %, 8%, 12%, 16% and 20% gadolinium content.

6.4.1 Space-charge potential

Figure 6.12 shows the calculated space charge potential as a function of percentage oxygen vacancy mole fraction for the (111), (210), (311) and (331) grain boundaries. It can be seen that the space charge potential increases slightly with increasing defect mole fraction. Experimental analysis of space charge potential often predict a decrease in the space charge potential with increasing defect mole fraction, as they find a decrease in the grain boundary resistivity and attribute that to a decreased potential barrier at the grain boundary core. These results suggest that for Gd-doped CeO_2, the space charge potential is largely unaffected by increasing defect concentration and therefore the increased resistivity observed may have a different cause.

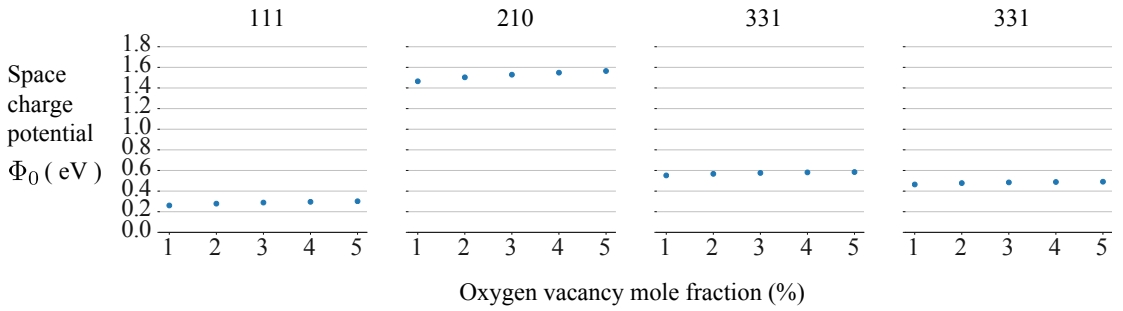

Figure 6.12: Calculated space charge potentials as a function of oxygen vacancy mole fraction for the (111), (210), (311) and (331) grain boundary orientations in $Gd-CeO_2$.

6.4.2 Resistivities

The perpendicular grain boundary resistivity ratio decreases with increasing oxygen vacancy concentration as shown in figure 6.13. The change in perpendicular resistivity ratio over the percentage defect mole fraction range varies up to an order of magnitude. The perpendicular activation energy also decreases as defect mole fraction is increased.

Alternatively, the parallel grain boundary resistivity ratio increases with increasing oxygen vacancy concentration as shown in figure 6.14. The change in parallel resistivity ratio over the percentage defect mole fraction range varies very slightly, and the grain boundary core remains highly conductive parallel to the grain boundary. The grain boundary activation energy once again decreases with increasing temperature.

The trend in relationship between defect mole fractions and resistivity is as expected due to the relationship between conductivity and concentration ($\sigma = c\mu z$). Experimentally, the decrease in resistivity is attributed to a reduction in the grain boundary "blocking effect", with the "potential barrier" being reduced due to an increased oxygen vacancy concentration. The results presented here show that there is a very slight increase in the space charge potential with increased oxygen vacancy concentration, but the overall grain boundary resistivity is decreased because there is a relative decrease in the oxygen vacancy depletion in the space charge region, simply because there are more oxygen vacancies available in the system.

It is has been found experimentally that there reached a maximum defect concentration before the ionic conductivity begins to decrease again due to defect-defect interactions becoming significant. The results given here show only the initial increase in ionic conductivity due to increase dopant concentration, but not the subsequent decrease due to the increased defect-defect interactions. To model this is beyond the scope of PYSCSES at

this time, as this model is able to predict the change in behaviour at low-to-moderate defect concentrations, but not at higher concentrations. Therefore, the results support the hypothesis that interactions beyond point-charge electrostatics are required to describe high defect concentrations correctly.

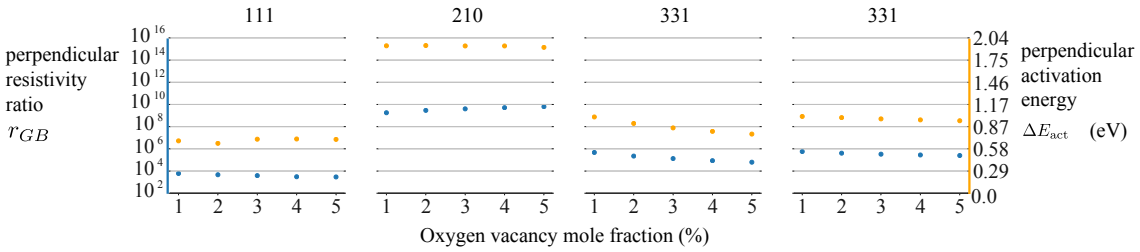

Figure 6.13: Calculated perpendicular grain boundary resistivities and activation energies as a function of oxygen vacancy mole fraction for the (111), (210), (311) and (331) grain boundary orientations in Gd−CeO_2.

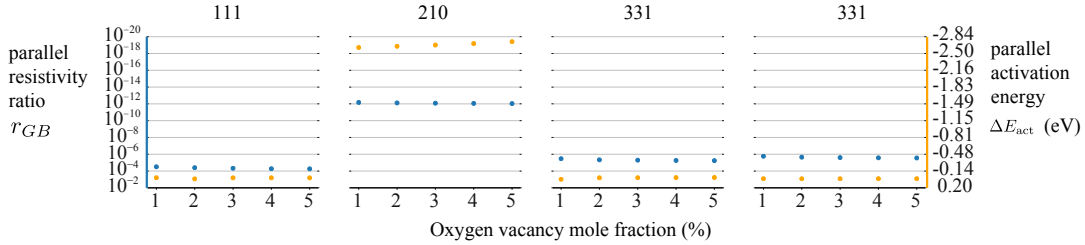

Figure 6.14: Calculated parallel grain boundary resistivities and activation energies as a function of oxygen vacancy mole fraction for the (111), (210), (311) and (331) grain boundary orientations in Gd−CeO_2.

6.5 Comparison between space-charge potential approximations

As discussed in detail in section 3.2.4, in the Mott-Schottky model, the space charge potential (the electrostatic potential at the grain boundary core) completely characterises the space-charge profile and activation energy. Because of this, experimental studies often report "space charge potentials" that have been obtained by parameterising the Mott-Schottky model from the experimental data. However, the Mott-Schottky model contains a number of assumptions that may not hold true in the real system, leading to potential errors in the estimated space charge potential.

Figure 6.15 shows the space charge potential calculated using the Poisson-Boltzmann solver and the Mott-Schottky model for each of the three Gd−CeO_2 grain boundary orientations.

The Mott-Schottky model consistently overestimates the magnitude of the space charge potential compared to the Poisson-Boltzmann solver, with values of 0.61 eV compared to 0.30 eV for the (111) grain boundary, values of 0.79 eV compared to 0.58 eV for the (311) grain boundary and values of 0.87 eV compared to 0.49 eV for the (331) grain boundary.

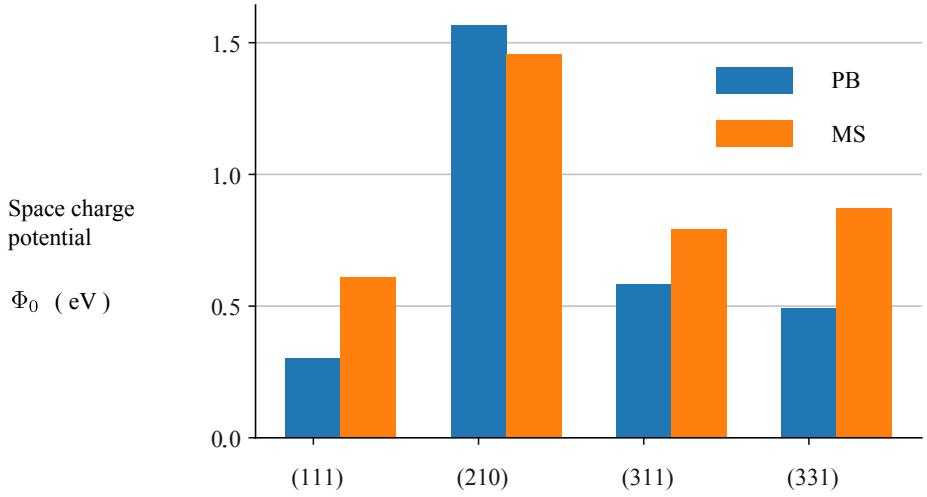

Figure 6.15: Calculated space charge potentials using both the Poisson-Boltzmann and Mott-Schottky methods for the (111), (210), (311) and (331) grain boundary orientations in $Gd-CeO_2$.

The (210) grain boundary exhibits anomalous behavior in this data set, as it appears that the Mott-Schottky model is underestimating the space charge potential compared to the Poisson-Boltzmann model. This can be attributed to the extremely high defect segregation energy calculated for the grain boundary core, which leads to complete saturation of oxygen vacancies in the core. In the real system, complete saturation of oxygen vacancies in the grain boundary core would be nonphysical and result in a breakdown of the grain boundary structure.

The overestimation of the space charge potential using the Mott-Schottky approximation compared to the Poisson-Boltzmann solver is attributed to the assumptions made within the model. As previously discussed, the Mott-Schottky model assumes a grain boundary region that is negligibly thin, with complete depletion of charge carriers in the space charge regions. In practice, the grain boundary region has a variable thickness and charge carriers are not fully depleted in the space charge region, which results in a lower space charge potential than predicted from the simple Mott-Schottky analysis.

6.6 Conclusions

Throughout the years Gd – CeO_2 has been extensively studied as a model solid oxide fuel cell material, due to it's relatively high ionic conductivity. Research into Gd – CeO_2 has continued with an aim to reduce the required operating temperature to an ambient level while maintaining device performance in solid oxide fuel cells. It has been recorded for some time that the presence of grain boundaries in Gd – CeO_2 negatively impact the ionic conductivity due to grain boundary blocking effects and the formation of space charge regions. In this chapter, the effect of the explicit structure of grain boundaries in Gd – CeO_2 has been explored. Historical works often treat grain boundary resistivities as an average over the grain boundaries present in the system but with the implementation of the site-explicit Poisson-Boltzmann solver, the explicit lattice structure of the grain boundary can be taken into consideration.

It was found the the grain boundary orientation has a large impact on the extent of defect redistribution and the calculated space charge properties such as electrostatic potential and grain boundary resistivities. The effect of operating temperature, sintering temperature and dopant concentration were varied and the results consistently follow what would be expected for a physical system.

While space charge formation has been extensively studied for Gd – CeO_2 systems, due to the large variation in properties between differing grain boundary orientations it can be argued that it is important to model space charge formation including information about the explicit lattice structure. Also, due to the large effect on macroscopic material properties, it is always import to consider the possibility of space charge formation in the design of any solid state electrochemical device.

Chapter 7

Nanoionics

7.1 Background

7.1.1 Nanocrystalline Solid Electrolytes

Nanostructured crystalline solid electrolytes are distinguished from conventional polycrystalline solid electrolytes by their relatively small grain sizes.[201] These nanocrystalline solid electrolytes (also known as nanoionic solid electrolytes) display a wide functional diversity and exhibit either different or enhanced properties compared to microcrystalline or bulk materials.[202] The variation in properties is often attributed to having a large number of interfaces which are so closely spaced that the distance between them becomes smaller than the critical length for certain phenomena, and thus the influence of surfaces and interfaces on the properties becomes significant. In other words, it cannot be taken for granted that the influence of the interface decays into the bulk, as the next interface may be perceptible.[203] Thermodynamics throughout the material may be governed by interfaces and therefore the finite size of the space charge regions must be taken into account in nanoionic materials. The benefit of narrowly spaced interfaces that act as fast ion pathways lies in the potential for enhanced effective ionic conductivity and the possibility of rapid bulk storage due to a reduction in the effective diffusion length.[203]

Maier has discussed how "nanoionic" effects, associated with small particle size, can be classified as "trivial", when near-interface regions do not overlap, and the interfacial contribution to the material properties scales linearly with interface density, and "true" when near-interface regions overlap (meaning there is no longer a "bulk" region of the system) and interfacial effects become non-linear.[204,205] True size effects are of fundamental im-

portance for understanding defect behaviour in nanocrystalline solid electrolytes.[72]

7.1.2 Theoretical Analysis of Nanoionics

The Nanoionic Effect

In nanoionic systems, the Debye length (λ - is strictly defined for the Gouy-Chapman model, but is often used as an approximate length scale for space charge effects) is significantly greater than the distance between interfaces. Therefore, a true size effect is the overlap of space charge regions between interfaces,[206] resulting in the sample being charged throughout and wholly influenced by the boundary phase.[72] In the case where space charge regions consist of an accumulation of charge carriers, it would be expected that the overlap in space charge regions would result in a further increase in the overall ionic conductivity, due to the absence of 'non-contributing' bulk regions. In the case of depletion, a reduction in the overall ionic conductivity would be expected.[206] This is attributed to the defect density at the center of the grain no longer reverting back to the bulk concentration c_∞.[207] The nanoionic effect predicts that not only does the concentration not revert back to the bulk concentration, but the variation is enhanced by an additional 'nano-size factor' (g), given by,

$$g = (4\lambda/d)[(c_x - c_\infty)/c_x]^{\frac{1}{2}}, \tag{7.1}$$

where c_x is the mobile charge carrier concentration in the first layer adjacent to the grain boundary core and d is the interboundary distance.[208] This effect is depicted in figure 7.1, which shows an enhanced decrease in charge carrier concentration due to the overlapping of space charge regions.

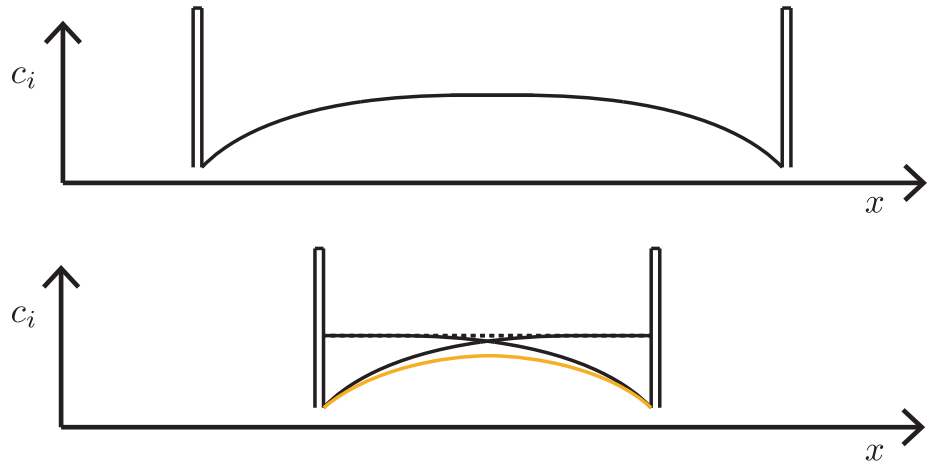

Figure 7.1: Schematic depicted the nanoionic effect in overlapping space charge regions

As previously discussed, the ionic conductivity of a charged species is proportional to the product of the concentration and mobility. Often the ionic conductivity is controlled by doping the solid electrolytes to increase charge carrier concentration, which can lead to problems with material stability, reactivity and defect interactions. A hypothetical method for enhancing the ionic conductivity is to use the nanoionic effect, allowing the modification of defect concentrations and mobilities.[209]

Many theoretical analyses of space charge effects in nanoionic materials treat the grain boundary effects using an analytical Poisson-Boltzmann description. However the chemical potential of a species measures the increase in total free energy if the concentration is altered. Maier has suggested a correction can be included if the concentration gradients are so steep in the interfacial regions that the local properties depend on them.[203]

$$\mu = \mu^o_{i,x} + RT \ln \left(\frac{c_{i,x}}{1 - c_{i,x}} \right) + RT \ln \gamma + z_i F \Phi_x, \tag{7.2}$$

where the activity coefficient γ corrects for energetic or entropic excess effects in non-dilute systems,[210] as in the region where depletion effects are enhanced between the grain boundary cores in nanoionic systems.

Maier[205] has theoretically studied space charge formation in nanosized CeO_2 and discussed the lowered formation energies for oxygen vacancies in the grain boundary core, and significant depletion effects in the space charge regions, resulting in an increased electron concentration. Therefore in nanosized systems, where the depletion effect is enhanced, a

significant n-type conductivity is expected in the space charge regions and the ionic conductivity should be restricted by the overlapping perpendicular space charge layers. This enhancement of electronic conductivity in nanoionic CeO_2 has also been reported in other works.[197]

7.1.3 Experimental Analysis of Nanoionics

In experimental synthesis of nanocrystalline solid electrolytes, the grain size is often controlled by altering the sintering temperature used when the sample is produced. A lower sintering temperature usually produces smaller grains, and thus decreases the inter-grain boundary distance. The grain size in nanocrystalline materials is usually observed using electron microscopy, followed by the determination of the ionic conductivity of the solid electrolytes using the impedance spectroscopy alongside the brick layer model. The brick layer model is discussed in more detail in appendix A.2. Further space charge analysis is often carried out following the Mott-Schottky analytical model described in section 3.2.4.

Acceptor doped ceria (CeO_2) has been extensively studied[198,199,211–216] to compare the properties between microcrystalline and nanocrystalline structures. It has been found that nanocrystalline acceptor doped ceria has an increased ionic conductivity of several orders of magnitude relative to samples with much larger grain sizes. This increased conductivity has been attributed to the smaller grain size causing a reduction in the blocking effect at grain boundaries, which would allow the grain boundary resistivity to decrease to nearer the bulk resistivity value. It is also theorised that the reduction in the grain boundary resistivity is due to a reduction in the space charge potential which is often assumed to determine the activation energy for grain boundary diffusion.[165] A reduction in the space charge potential would in that case result in a lower activation energy allowing more ionic diffusion across the grain boundary. Bellino *et al.*[214] have published data that supports this theory and report an increase in total ionic conductivity of one order of magnitude in nanostructured ceria solid electrolytes compared to the conductivity of conventional microcrystalline materials.

Anselmi-Tamburini *et al.*[199] have theorised that the reduced potential observed in nanocrystalline acceptor doped-CeO_2 is caused by the low sintering temperature used in the synthesis of the samples. They argue that at the lower temperatures, the mobility of the dopant ions will be significantly decreased and therefore it can be assumed that there is a uniform dopant distribution across the grain boundary, counteracting the grain boundary potential and eliminating the blocking effect. The effect of the sintering and annealing

temperatures on the mobility of the dopant ions in ceria has recently been experimentally investigated.[217] These authors noted that once the samples have been sintered at a low temperature, there was not necessarily a large increase in grain size with annealing at a higher temperature (an annealing temperature of 1100°C gave a reduction in grain boundary density of 27.3%[217]). However they suggested that using a high annealing temperature resulted in considerable segregation of dopants to the space charge region. Bae *et al.* reported that a sample produced using an annealing temperature of ≈700°C had the highest conductivity, due to its enhanced crystallinity, followed by samples which had not undergone any thermal annealing. Samples annealed at 900°C and 1100°C had considerably lower conductivities which was attributed to the segregation of dopant ions to the region near the grain boundary core intensifying the space charge effect. Therefore it was suggested that a lower temperature fabrication method would increase the probability of having a uniform dopant concentration across a sample, suppressing the space charge potential and thus increasing the ionic conductivity.

7.2 Effect of inter-boundary separation

7.2.1 Modelling

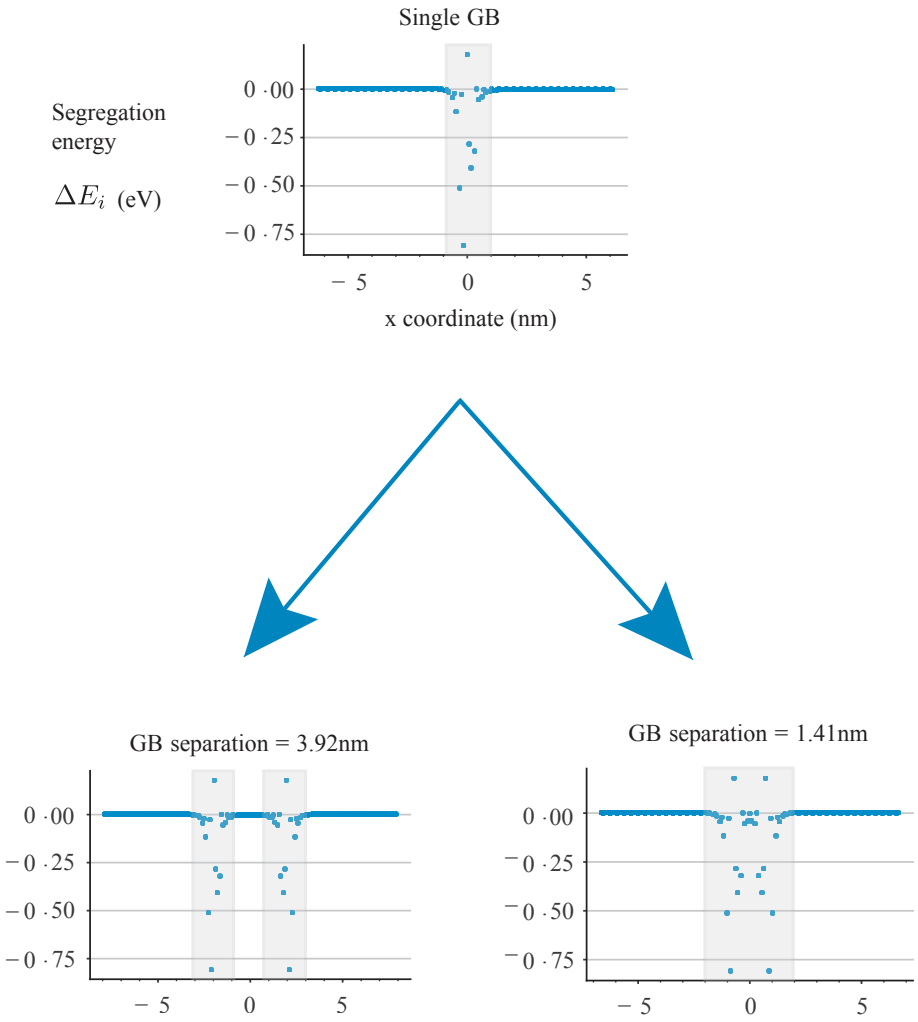

Figure 7.2: Schematic showing how segregation energies calculated for a single grain boundary are reflected and combined to produce a segregation energy profile for a pair of grain boundaries at different separations.

The dual grain boundary systems are created by taking the same input data as for the work in the previous chapter for the (111) grain boundary in Gd-doped CeO_2 and mirrored on sites moving closer to the grain boundary.

The two mirrored sets of segregation energies are then conjoined to give a set of systems with two grain boundaries, with varying inter-boundary distances. The inter-boundary

distance is decreased until the separation is in the nano-regime where the space charge regions are expected to overlap. The limit for how close the grain boundaries could be placed together was dictated by avoiding overlap of non-zero segregation energies as at this point the defect segregation energy values would be affected and therefore not exist at the same value.

Once the dual grain boundary segregation energy data has been created, it can be used as the input for the Poisson-Boltzmann solver to calculate the electrostatic potential, defect distributions and oxygen vacancy depletion profiles over the dual grain boundary system. Oxygen vacancy depletion is calculated as

$$D_i^s = 1 - \frac{c_i}{c_\infty}, \tag{7.3}$$

and is used to quantify the nanoionic effect. If the nanoionic effect is significant, it would be expected that there is a additional oxygen vacancy depletion with the dual grain boundary system when compared to twice the oxygen vacancy depletion.

7.2.2 Calculated space charge properties

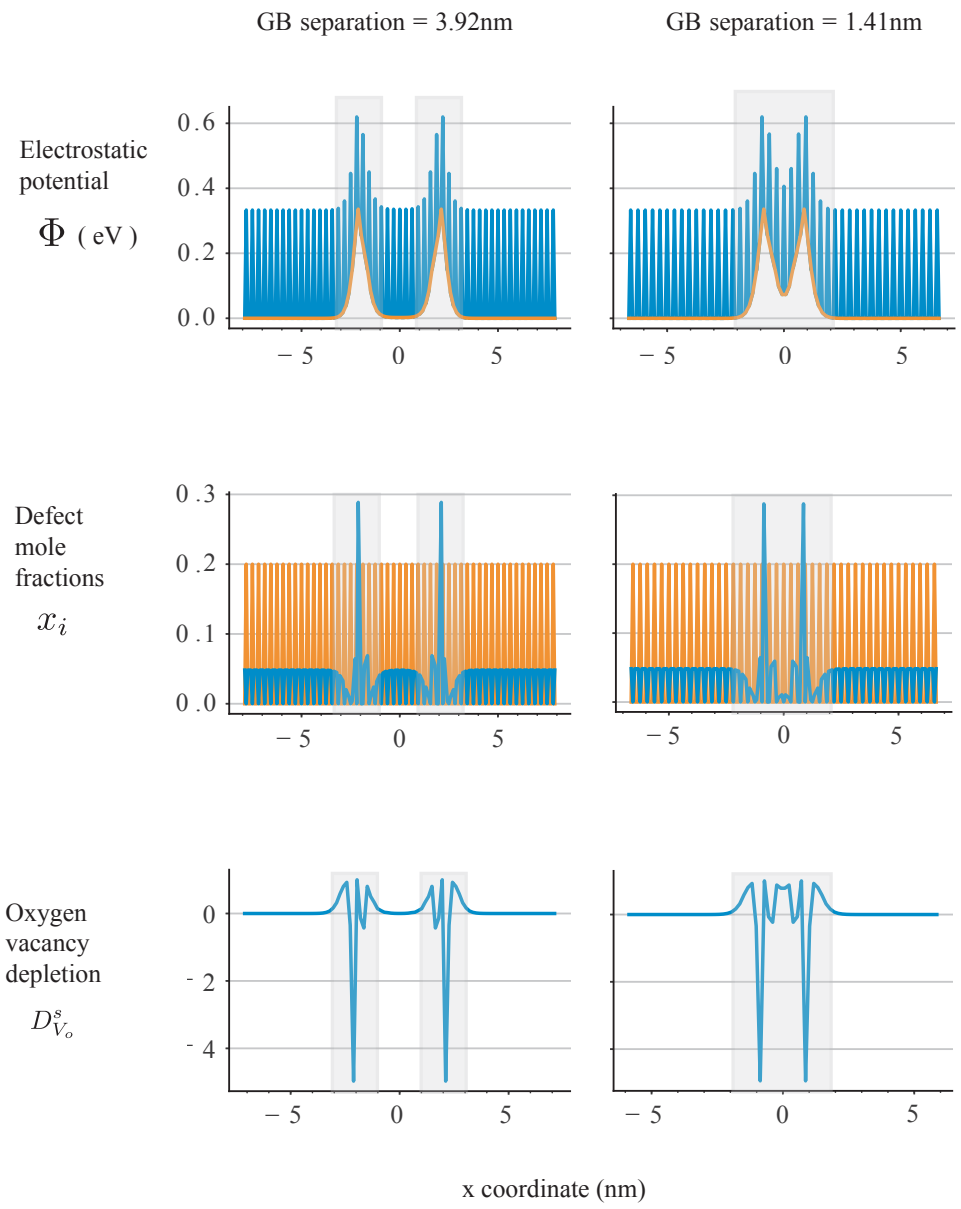

Figure 7.3: Calculated electrostatic potential, charge density and oxygen vacancy depletion profiles for two grain boundary separations.

Figure 7.3 shows the electrostatic potential, defect mole fractions and depletion factor over the dual grain boundary systems at separations of 3.92 nm and 1.41 nm. It can be seen that as the inter-boundary distance is decreased from 3.92 nm to 1.41 nm the space charge regions begin to overlap. The electrostatic potential no longer returns to a bulk electrostatic potential of 0.0 eV between the grain boundary cores as the region between

the grain boundary cores remains charged throughout. This results in a region between the grain boundary cores that does not return to 'bulk-like' which affects the distribution of mobile oxygen vacancies between the grain boundaries. In this region, the oxygen vacancy depletion is enhanced. Due to the relationship between charge carrier concentrations and ionic conductivity it is expected that the enhanced depletion of oxygen vacancies will result in a negative impact on the ionic conductivity of the system. Calculations of the effective resistivity of the dual grain boundaries as a function of separation are described in the next section.

7.2.3 Depletion factor and resistivity ratio

Figure 7.4 displays the calculated electrostatic potential, oxygen vacancy depletion at the midpoint between the grain boundary cores, and the resistivity ratio of the system at a range of different grain boundary separations between 1 nm and 4 nm, and compares this to a system with only a single grain boundary. As the grain boundaries are brought closer together, the electrostatic potential at the midpoint between the grain boundaries increases from 0.0 eV at 3.92 nm to 0.14 eV at 1.41 nm, as the region becomes less 'bulk-like'. As the electrostatic potential increases between the grain boundaries, the depletion of oxygen vacancies also increases, from no (0.0) depletion at 3.92 nm to complete (1.0) depletion at 1.41 nm. This complete depletion of oxygen vacancies results in an increase of the grain boundary resistivity ratio, from 1.4×10^6 to 1.6×10^6, as predicted from nanoionic theory.

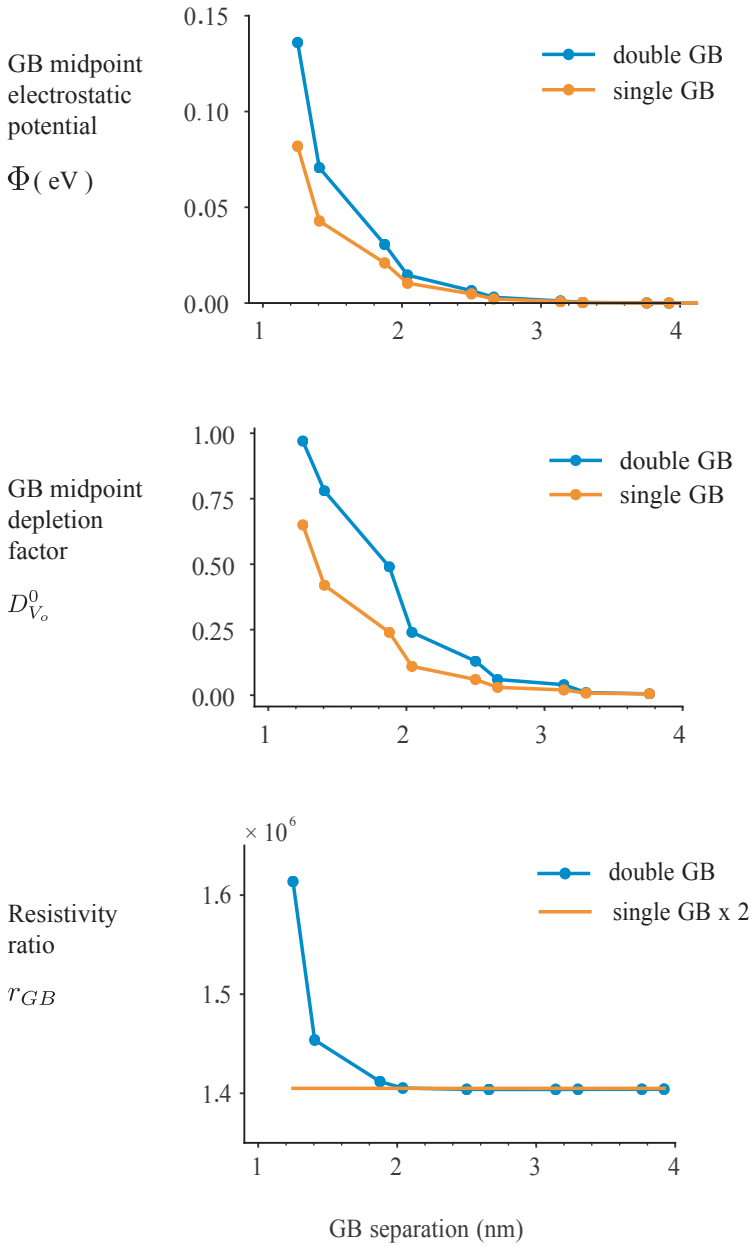

Figure 7.4: Calculated space charge potential, oxygen vacancy depletion factor and grain boundary resistivity ratio for a range of grain boundary separations.

To quantify the strength of the nanoionic effect, the oxygen vacancy depletion factor at the midpoint between the grain boundaries in the dual grain boundary system are compared to twice the oxygen vacancy depletion of a single grain boundary.

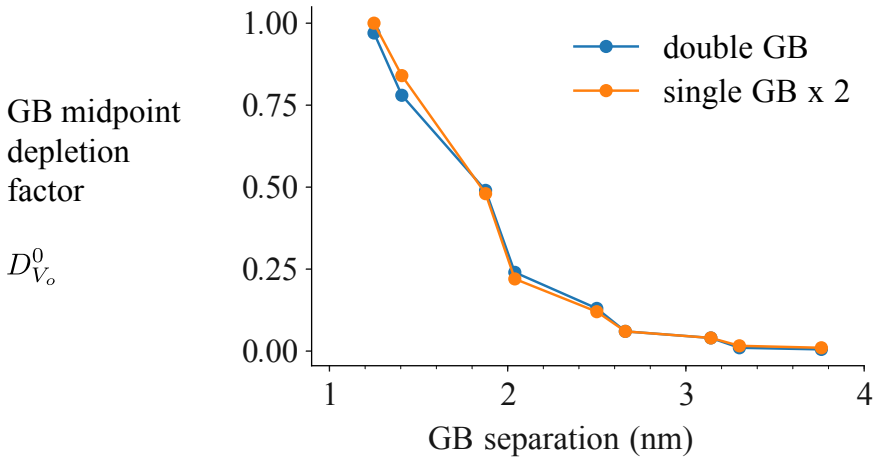

Figure 7.5: Calculated depletion factor for dual grain boundary systems compared to the effect for a single grain boundary system multiplied by 2

Figure 7.5 shows the comparison between the depletion factor for the dual grain boundary system and twice a single grain boundary system and it can be seen that there is no significant difference between the values. This suggests that there is no additional depletion between the grain boundary cores as predicted by the "nanoionic effect", and that the increase in resistivity as grain boundaries separations are increased is because the concentration of oxygen vacancies remain depleted throughout the structure.

7.3 Conclusions

Nanoionics have proved of interest to solid state ionic research for a number of decades due to the wide functionality and enhanced properties compared to microcrystalline or bulk phase materials. The 'true' and 'trivial' nanoionic effects are of importance for understanding defect behaviour in nanosized solid electrolytes. In this chapter, the 'true' nanoionic effects, including local electrostatic potential and charge carrier depletion and the 'trivial' nanoionic effects such as the ionic conductivity of the system have been investigated. Theoretical literature predicts an enhanced decrease in charge carrier concentration due to the overlapping of space charge regions which is in agreement with the results calculated from the site explicit Poisson-Boltzmann solver used throughout this project. On the other hand, experimental analyses in nanoionic $Gd-CeO_2$ observe an increase in ionic conductivity as the grain size within the system is decreased. Some experimentalists argue that the increased ionic conductivity is due to the overlapping space charge regions reducing the potential barrier for diffusion across the grain boundary, although it is also

argued that the discrepancy between theoretical and experimental analyses is due to the synthesis conditions used when preparing the samples. This could include the use of low sintering temperatures when preparing nanocrystalline samples, impacting the distribution of dopant ions and therefore the space charge effects observed.

Overall, the space charge properties were modelled for nanocrystalline Gd-doped CeO_2, and while the results agree with the theoretical assumptions that the resistivity should increase with decreasing grain boundary separation, they disagree that there is an additional depletion of oxygen vacancies due to the nanoionic effect.

Chapter 8

Li_3OCl

8.1 Background

Lithium ion batteries were first introduced by Sony in 1990, and since have revolutionised the portable electronics industry.[87] They have found wide applications in technologically important areas because of their high energy density, power capacity, charge–discharge rate, and long cycling lifetime.[218] Lithium ion batteries are the subject of continued scientific research, with the aim to improve their properties and characteristics.[219] Traditional lithium ion batteries have critical safety issues due to the use of highly flammable organic liquid electrolytes or polymer electrolytes which have low thermal stability which can cause fire accidents and explosions.[220] All solid state batteries, whereby the flammable liquid electrolyte is replaced by a solid electrolyte, have attracted great attention due to their improved safety and increased energy density. There are many possible candidates for solid electrolytes for battery applications including sodium super ionic conductors (NASICON), lithium super ionic conductors (LISICON), lithium phosphorus oxynitride (LiPON), garnets, perovskites, and anti-perovskites such as Li_3OCl.

8.1.1 Li_3OCl as a solid state battery material

Anti-perovskite type solid electrolytes were first introduced by Zhao and Daemen[221] in 2012, and have been receiving increasing attention since. These anti-perovskites were designed based on changing the perovskite system of $A^+B^{2+}X_3^-$, where A is a monovalent metallic cation, B is a divalent metallic cation and X is a halide, by electronically inverting the system to $A^-B^{2-}X_3^+$, where A is a halogen, B is an oxygen and X is lithium.

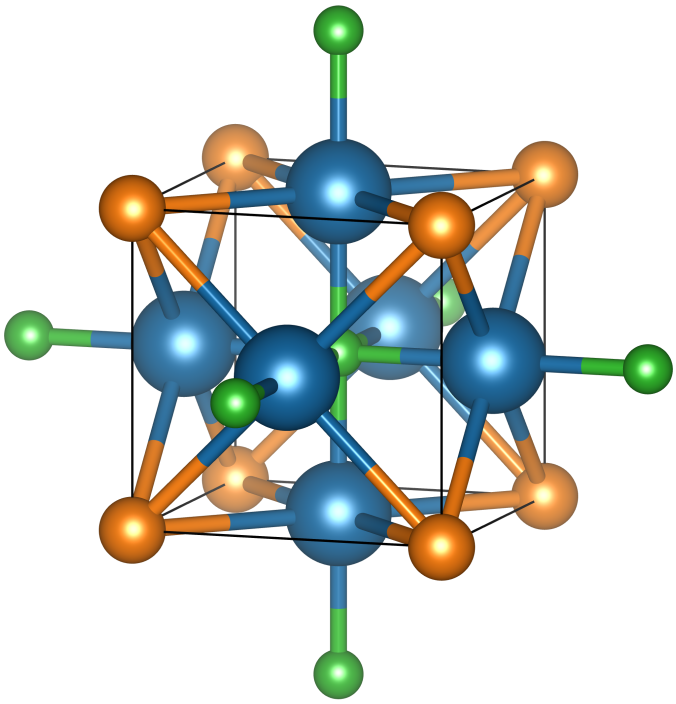

Figure 8.1: Li_3OCl unit cell structure with Li in blue, Cl in orange and O in green.

Li_3OCl showed a typical perovskite structure and exhibited an ionic conductivity of 1.94×10^{-3} S cm^{-1}, making it a promising candidate for use as a solid electrolyte in electrochemical devices. Despite the promising nature of Li-rich anti-perovskites, the defect behaviour is still not well understood.

8.1.2 Experimental studies

Throughout the experimental studies published, there have been conflicting reports of ionic conductivities in Li_3OCl, varying from 1×10^{-3} to 1×10^{-7} S cm^{-1}. Zhao and Daemen first presented lithium-rich anti-perovskites as a novel class of solid electrolytes.[221] The synthesised these anti-perovskites using a self 'developed and efficient' synthesis route, and they used electrochemical impedance spectroscopy to analyse the samples. Zhao and Daemen reported exceptionally high ionic conductivities of 0.85×10^{-3} S cm^{-1} and activation energies of 0.2 eV to 0.3 eV, for the end-member Li_3OCl anti-perovskite at room

temperature. Following this Lü and co-workers began looking into Li_3OCl thin films[222] and measured ionic conductivities of 8.9×10^{-6} S cm^{-1} and calculated activation energies through an Arrhenius relationship of 0.36 eV. While this is lower than the conductivity reported by Zhao and Daemen the result was still much higher than that of the ceramic bulk Li_3OCl which had been reported at 5.8×10^{-7} S cm^{-1}. This increase in ionic conductivity relative to bulk Li_3OCl was attributed to the intimate grain boundary resistances proposed to be significant in bulk Li_3OCl being reduced in the thin film samples. Lü and co-workers continued researching thin films and reported ionic conductivities of 2.0×10^{-4} S cm^{-1},[223] which is a considerable enhancement compared to the bulk phase. The wide range in published ionic conductivities reported in Li_3OCl has been attributed to the presence of grain boundaries present in the prepared samples, although the impact of grain boundaries on ionic conductivity in Li_3OCl is not well understood, as it is hard to resolve from experimental studies. Therefore further research into the explicit effects of grain boundaries in lithium rich anti-perovskites would be advantageous.

8.1.3 Theoretical studies

There are few significant theoretical papers published studying grain boundary effects in Li_3OCl. The first paper conceptualising the potential for space charge formation in Li_3OCl was published in 2017 by Stegmaier and coworkers.[224] They used density functional theory to calculate the relationship between Li vacancy formation and cell potential, and the formation of a double layer at the solid electrolyte-electrode interface. The first theoretical study to explicitly consider grain boundaries, instead of surfaces and interfaces was published by Dawson *et al.*[87] in 2018. In this study molecular dynamics simulations were used to quantify the effect of grain boundary resistance on the Li conductivity for four structurally different Li_3OCl grain boundaries. They calculate lithium ion hopping activation energies and resolve that there is a higher activation energy (ranging between 0.40 eV and 0.56 eV) at the grain boundary compared to the bulk (0.29 eV). From these findings they conclude that it is important to address ion redistribution, defect segregation and space charge effects occurring in Li_3OCl due to the presence of grain boundaries. The second theoretical paper studying grain boundary effects in Li_3OCl was published by Chen *et al.* also in 2018,[225] and agrees with the findings of Dawson *et al.*. Chen *et al* used nudged elastic band ab initio molecular dynamics and found the lithium ion hopping activation ranged from 0.40 eV to 0.60 eV at the grain boundary, compared to 0.34 eV in the bulk. This study only looks at changes in diffusion and potential energy barriers in

the core region. The authors agree that it is important to further study the effect of grain boundaries and space charge formation in lithium antiperovskites.

8.2 The effect of grain boundaries on space charge in Li_3OCl

Due to the various proposals that the presence of grain boundaries cause a lowered ionic conductivity in these solid electrolytes, it is important to understand the grain boundary behaviour in solid electrolytes for use in Li ion batteries. Previous studies have only considered the effect of the grain boundary core, not the affect of the associated space charge formation. The extent to which space charge formation is significant in these materials is therefore unknown. To investigate space-charge formation at grain boundaries in Li_3OCl, we performed combined atomistic-continuum calculations on three Li_3OCl grain boundaries. We used the grain boundary structures generated by Dawson *et al.* for their previous molecular dynamics study, and calculated lithium vacancy segregation energies using DFT. The exchange-correlation functional was evaluated using the generalised gradient approximation (GGA) as implemented in VASP. The projector augmented wave theory, together with a well-converged energy cutoff of 520 eV, was used to describe the wave functions, which were sampled on a Γ-centred 4×4×1 k-point mesh. With these settings, DFT energies and atomic forces were converged to within 1×10^{-6} meV/cell and 1×10^{-2} eV/Å, respectively.

These defect segregation energies (shown in figure 8.2) and grain boundary structures were used to calculate the equilibrium lithium vacancy and chlorine vacancy defect distributions, electrostatic potential and ionic conductivities, at a temperature of 298K and a bulk lithium vacancy mole fraction of 10 %, using the full site explicit model within PYSCSES.

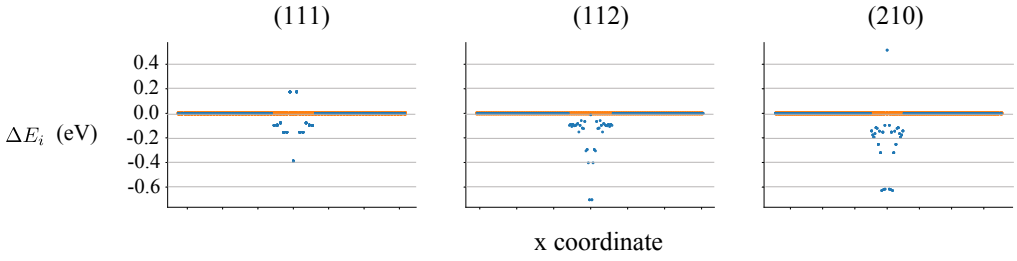

Figure 8.2: Calculated defect segregation energies for Li (blue) and Cl (orange) for the (111), (112) and (210) grain boundary orientations in Li_3OCl.

Space charge effects, while widely researched in regards to solid oxide fuel cell materials, are not often considered in solid state battery materials, although the effects may be significant

to the material performance. The explicit calculation of space charge properties in Li-ion solid electrolytes, including Li_3OCl, have not been attempted prior to the work carried out in this chapter.

8.2.1 Space charge properties

Figure 8.4 shows the electrostatic potential, charge density and defect mole fractions across the space charge region for the (111), (112) and (210) grain boundaries in Li_3OCl. These results predict that there is a significant defect redistribution to the grain boundary, and an associated space-charge formation for each of the structures. As with the gadolinium doped ceria case presented in chapter 6, the effect of the grain boundary orientation is important to understanding space charge phenomena in solid electrolytes because experimental samples are expected to exhibit grain boundaries with a range of different orientations. The calculated space charge properties vary significantly with grain boundary orientation. The (111) grain boundary has a calculated space charge potential of -0.26eV and a grain boundary lithium vacancy mole fraction of 0.28, the (112) grain boundary has a calculated space charge potential of -0.57eV and a grain boundary lithium vacancy mole fraction of 0.42 and the (210) grain boundary has a space charge potential of -0.45eV and a grain boundary lithium vacancy mole fraction of 0.58.

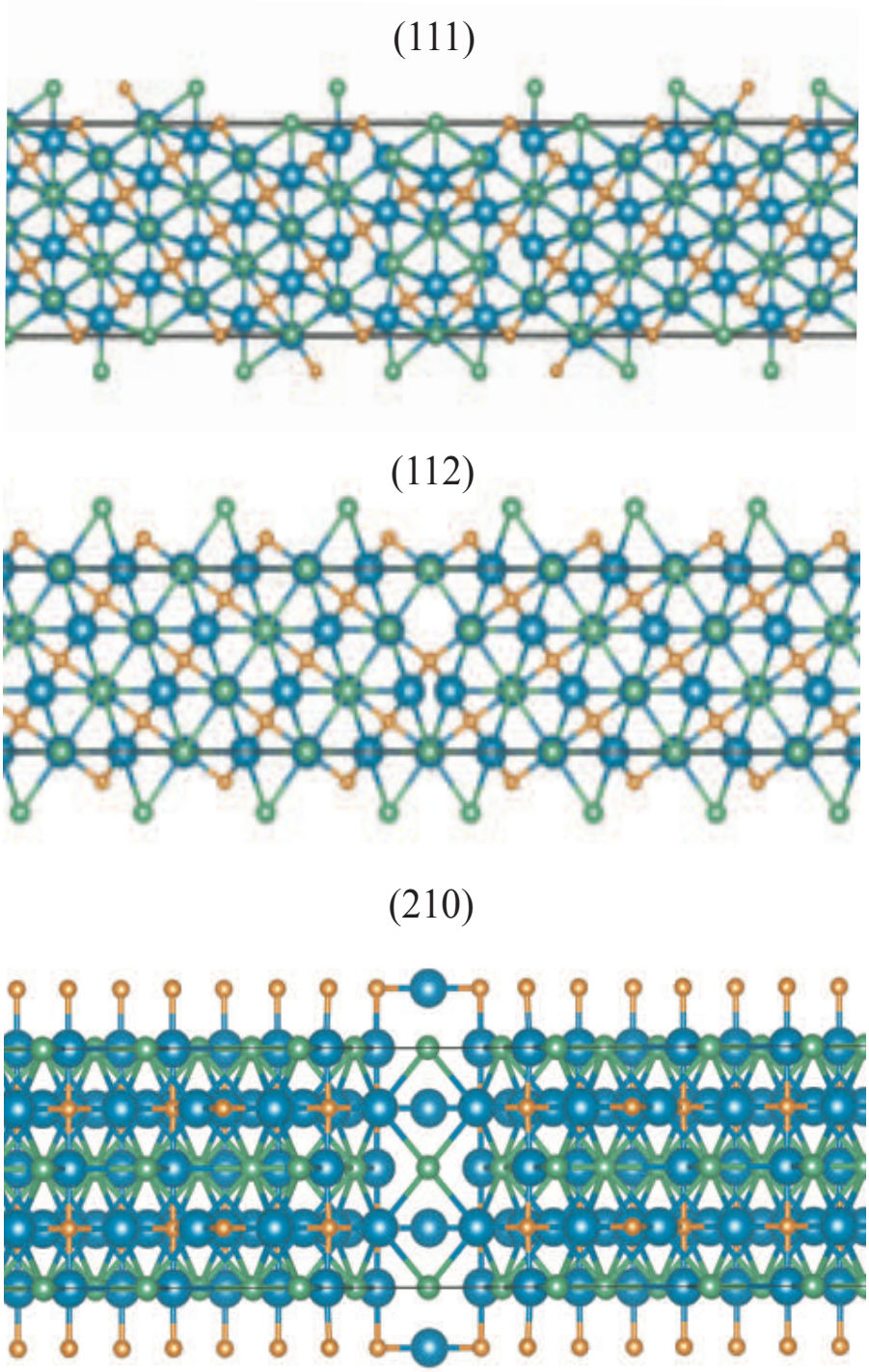

Figure 8.3: Grain boundary structures for the (111), (112) and (210) grain boundary orientations in Li_3OCl.

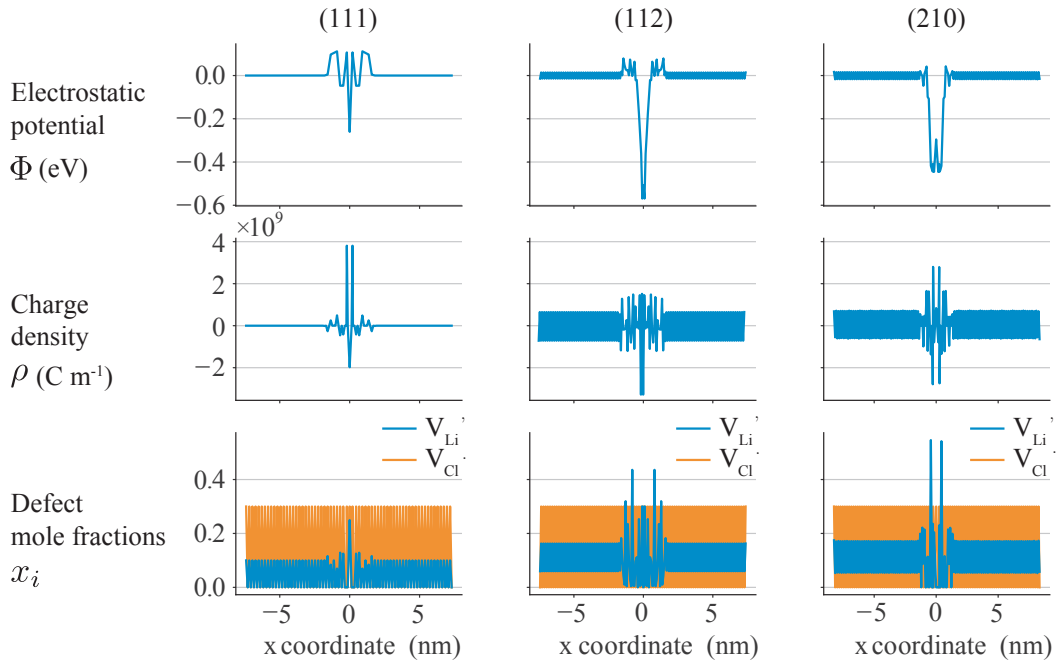

Figure 8.4: Calculated space charge properties for the (111), (112) and (210) grain boundary orientations in Li_3OCl.

8.2.2 Resistivities

Due to the relationship between conductivity and concentration ($\sigma = c\mu z$), variation in the defect distributions between structures can lead to a significant variation in grain boundary resistivities. Figure 8.5b shows the variation in grain boundary resistivity for the (111), (112) and (210) grain boundary structures. It can be seen that the grain boundary resistivity ratio varies significantly depending on grain boundary orientation. The resistivity is 1.1×10^4 for the (111) grain boundary, to 5.6×10^{12} for the (112) grain boundary and 2.0×10^{18} for the (210) grain boundary. This variation is 14 orders of magnitude different between the (111) and (112) grain boundaries, which suggests that the grain boundary orientation has a large impact on the materials ionic conductivity.

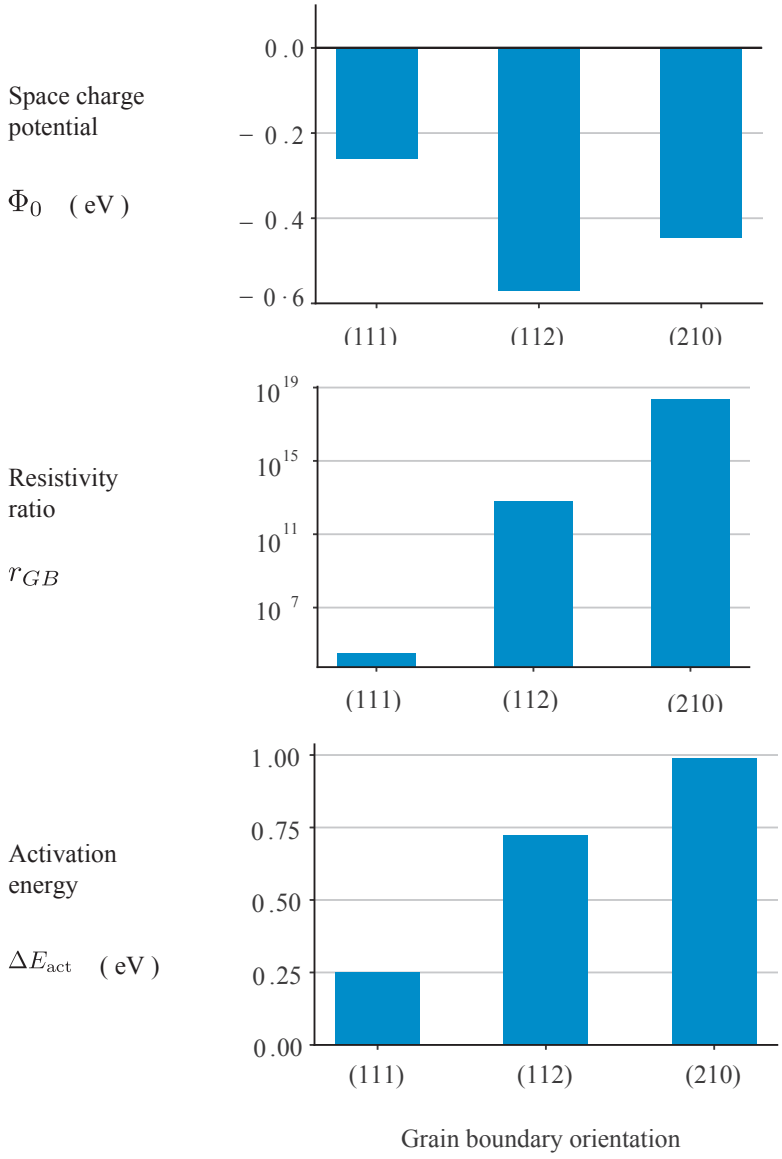

Figure 8.5: Calculated space charge potentials, grain boundary resistivities and activation energies for the (111), (112) and (210) grain boundary orientations in Li_3OCl.

In the analytical Mott-Schottky model, the predicted resistivity ratio only depends on the potential at the grain boundary core, ignoring the details of the defect distribution through the space charge region. Our approach takes into account the full defect distribution in the space charge regions. It can be seen in figure 8.5 that the calculated resistivity ratio is not only dependent on the space charge potential, as the (112) grain boundary has the greatest space charge potential, whereas the (210) grain boundary exhibits the greatest grain boundary resistivity. The large variation in the resistivity ratio can be understood

by examining the calculated defect concentration profiles for the three grain boundaries. The width of the lithium vacancy depletion and thus, the space charge region is greater for the (210) grain boundary, so there is an overall larger depletion of mobile charge carriers in the regions adjacent to the grain boundary core than the (112) orientation, resulting in this increased grain boundary resistivity. In addition to the grain boundary resistivity, the grain boundary activation energy can also be calculated for each grain boundary by applying an Arrhenius relationship and it can be seen in figure 8.5 that the activation energy follows the same trend as the grain boundary resistivity, varying significantly with orientation. The (111) grain boundary which has the lowest grain boundary activation energy of 0.20 eV, through to the (112) grain boundary has an activation energy of 0.72 eV and the (210) grain boundary has the greatest grain boundary activation energy of 0.99 eV. These results show a variation in activation energy of 0.79 eV between the (111) and (210) grain boundary structures, which is significant.

8.3 Effect of temperature

As previously discussed, the temperature affects the space charge properties and exhibited ionic conductivities of solid electrolytes. In this section, the effect of temperature on the defect distributions, electrostatic potentials and grain boundary resistivities is investigated for each of the three structurally different grain boundaries at a range of temperatures between 773.15 K and 1273.15 K.

8.3.1 Space charge properties as a function of temperature

Figure 8.6 shows the calculated electrostatic potentials and Debye lengths over the temperature range 223 K to 1273 K. It can be seen that as the temperature of the system increases, the space charge potential decreases. Similarly to the $Gd-CeO_2$ system, This decrease in space charge potential is due to lithium vacancies having the additional energy to overcome the "trapping" of the grain boundary core, resulting in a lower concentration of lithium vacancies at that point. The lower lithium vacancy concentration lowers the charge density at the grain boundary core and in turn lowers the space charge potential.

The Debye length (characteristic width of the space charge region) increases with increasing temperature. This is because as the temperature of the system is increased, the thermodynamic driving force for lithium segregation to the grain boundary core varies with E_{seg}/kT, resulting in less lithium vacancies in the grain boundary core. The lithium

vacancies become more diffuse and the space charge region extends further. While there is a significant variation in the Debye length over the temperature range for the three grain boundary orientations, the difference between the Debye length for three orientations is negligible over the Li mole fraction range.

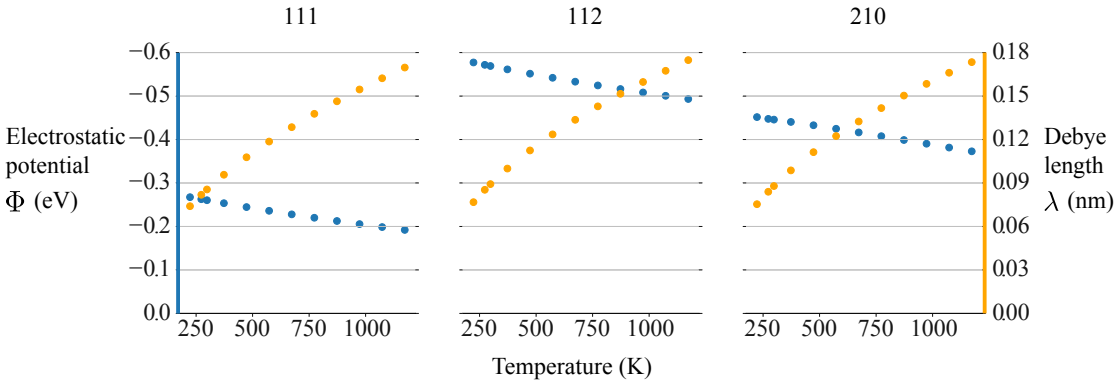

Figure 8.6: Calculated space charge potentials and Debye lengths as a function of temperature for the (111), (112) and (210) grain boundary orientations in Li_3OCl.

8.3.2 Effect of temperature on grain boundary resistivities

Figure 8.7 shows the grain boundary resistivity and activation energy for the (111), (112) and (210) grain boundaries at a temperature range of 223 K to 1273 K. It can be seen that as the temperature is increased the grain boundary resistivity decreases. As with the space charge potential, the grain boundary resistivities decrease with increasing temperature because there is a lower concentration of lithium vacancies at the grain boundary core at higher temperatures, reducing the effective charge of the grain boundary and reducing the depletion of lithium vacancies in the space charge region. As the resistivity is inversely proportionate to mobile charge carrier concentrations, as the depletion is reduced in the space charge region, the resistivity is reduced. The lower grain boundary resistivity then reduces the grain boundary activation energy.

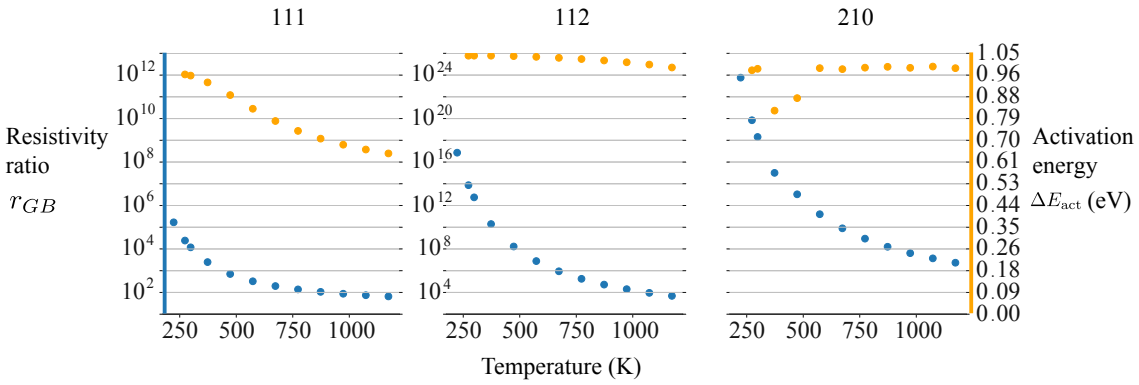

Figure 8.7: Calculated grain boundary resistivities and grain boundary activation energies as a function of temperature for the (111), (112) and (210) grain boundary orientations in Li_3OCl.

8.4 Effect of mole fractions

As previously discussed, the dopant concentration can have a large impact on the space charge properties and ionic conductivities in Li_3OCl, therefore the Poisson Boltzmann solver has been used to calculate the space charge properties, such as defect distributions and electrostatic potentials along with grain boundary resistivities for each of the three structurally different grain boundaries at a range of lithium vacancy content between 1 % and 10 %.

8.4.1 Space charge properties as a function of defect mole fraction

Figure 8.8 shows the electrostatic potential and Debye length as a function of defect mole fraction. It can be seen that as the percentage of defects in the system increases, the space charge potential remains fairly constant. This negligible variation in potential is due to the concentration of defects being consistently increase over the entire system, resulting in the same relative difference in Li vacancy concentration between the bulk and the grain boundary core. In this example, Mott-Schottky conditions are assumed, with the Cl vacancies unable to redistribute, mirroring the proposed behaviour of the real system. If the Cl vacancies were considered mobile, there may have been a more significant variation in space charge potential with increasing concentration of defects. Alongside the effect on the space charge potential, the Debye length increases with increasing defect mole fraction. The increase in the Debye length is due to the increase in lithium vacancies available in the system, leading to a more diffuse space charge region. While there is a significant variation in the Debye length over the mole fraction range for the three grain boundary

orientations, as with varying temperature, the difference between the Debye length for three orientations is negligible.

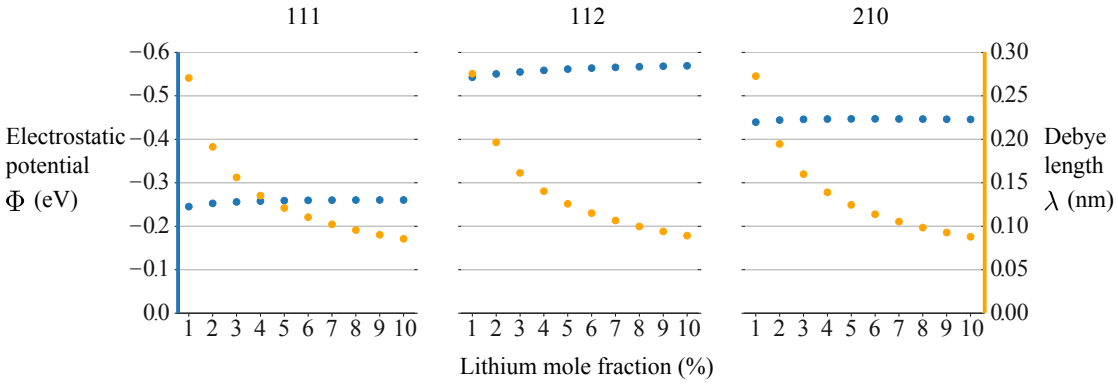

Figure 8.8: Calculated space charge potentials and Debye lengths as a function of lithium vacancy mole fraction for the (111), (112) and (210) grain boundary orientations in Li_3OCl.

8.4.2 Effect of temperature on grain boundary resistivities

Figure 8.9 shows the grain boundary resistivity ratio and activation energy as a function of the lithium vacancy mole fraction for the (111), (112) and (210) grain boundaries. It can be seen that as the lithium vacancy concentration is increased, the grain boundary resistivity decreases. The trend in relationship between defect mole fractions and resistivity is expected due to the relationship between conductivity and concentration ($\sigma = c\mu x$). In similar systems, experimentally, the decrease in resistivity is attributed to a reduction in the grain boundary "blocking effect", with the "potential barrier" being reduced due to an increased lithium vacancy concentration. The results presented here show that there is a very slight increase in the space charge potential with increased oxygen vacancy concentration, but the overall grain boundary resistivity is decreased because there is a relative decrease in the lithium vacancy depletion in the space charge region, simply because there are more lithium vacancies available in the system. It can also be seen in figure 8.9 that the grain boundary activation energy decreases with increasing lithium vacancy content.

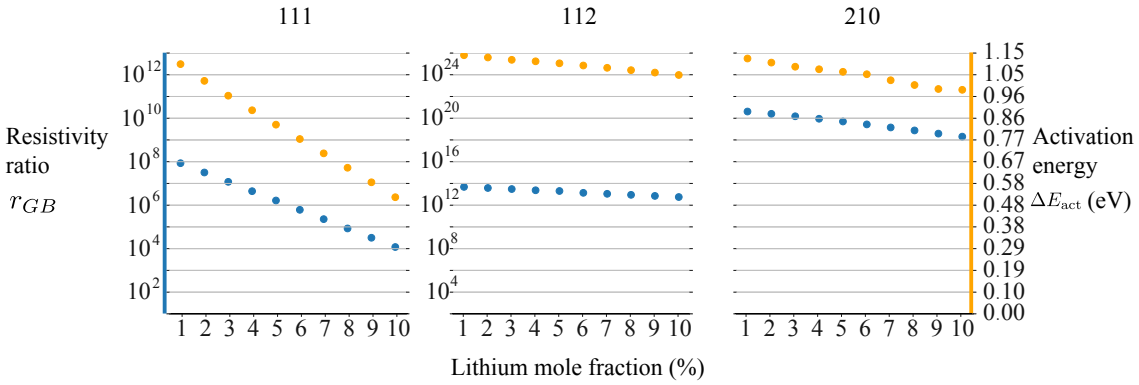

Figure 8.9: Calculated grain boundary resistivities and grain boundary activation energies as a function of lithium vacancy mole fraction for the (111), (112) and (210) grain boundary orientations in Li_3OCl.

8.5 Comparison between space charge potential approximations

As discussed in detail in section 3.2.4 and presented for gadolinium doped ceria in section 6.15, experimental conductivity data can be used to calculate a space charge potential by applying the Mott-Schottky model. The Mott-Schottky model gives an analytical description of space charge behavior that is completely characterised by the space charge potential.

Figure 8.10 shows the space charge potential calculated using the Poisson-Boltzmann solver and the Mott-Schottky model for each of the three Li_3OCl grain boundary orientations. As with the $Gd-CeO_2$ study, the Mott-Schottky model consistently overestimates the magnitude of the space charge potential compared to the Poisson-Boltzmann solver, with values of -0.32 eV compared to -0.26 eV for the (111) grain boundary, values of -0.86 eV compared to -0.57 eV for the (112) grain boundary and values of -1.2 eV compared to -0.44 eV for the (210) grain boundary.

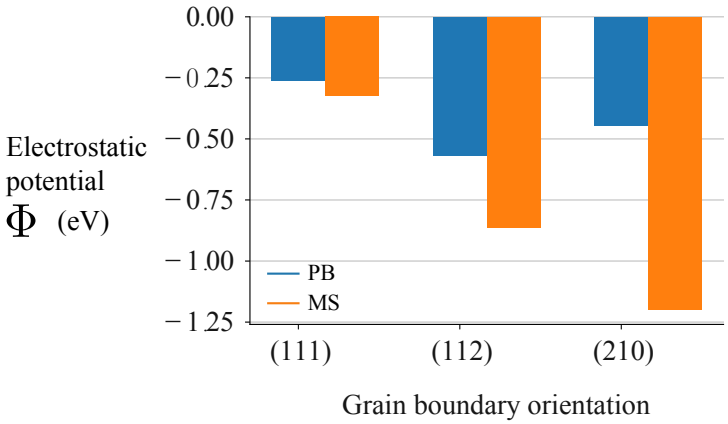

Figure 8.10: Space charge potential calculated for the (111), (112) and (210) grain boundary orientations in Li_3OCl using both the Poisson-Boltzmann solver (blue-PB) and the Mott-Schottky approximation (orange-MS).

The overestimation of the space charge potential using the Mott-Schottky approximation compared to the Poisson-Boltzmann solver is most likely attributed to the assumptions made within the model. The Mott-Schottky approximation assumes that the grain boundary region is negligibly thin, and that mobile charge carriers are completely depleted in the space charge region, giving an analytical solution of space charge behaviour completely characterised by the space charge potential. In practice, the grain boundary region has a variable thickness and charge carriers are not fully depleted in the space charge region, which results in a lower space charge potential.

8.6 Conclusions

As a material, Li_3OCl has been gaining interest as a potential solid electrolyte for use in solid state lithium ion batteries due to it exhibiting high ionic conductivities. The pre-existing literature on grain boundary effects in Li_3OCl is limited, however speculates that the presence of grain boundaries impedes the ionic conductivity of the material. This chapter has described the space charge effects in Li_3OCl using a site explicit Poisson-Boltzmann model to calculate the electrostatic potential, defect distributions and grain boundary resistivities for three structurally different grain boundaries. The results show that the presence of grain boundaries affect the distribution of mobile charge carriers in Li_3OCl, with formation of space charge due to segregation of the mobile Li vacancies to the grain boundary core and the resulting depletion in the space charge region. The formation of space charge results in a greater grain boundary resistivity, which causes a

reduction in the overall ionic conductivity of the material. It has also been shown the the grain boundary orientation affects the space charge formation and the extent to which the ionic conductivity is impacted.

While space charge formation has been extensively studied in materials for use in solid oxide fuel cells, the calculation of space charge properties in solid state battery materials is a relatively novel concept. Due to the calculated space charge properties presented in this chapter, it can be stated that considering the effect of space charge formation is important when designing novel materials for all solid state electrochemical devices.

Chapter 9

Reliability of the Computational Methods

A number of approximations are included in the model which could affect the reliability of the data presented in this thesis. Defect segregation energies are calculated using either classical atomistic calculations or density functional theory, both of which include approximations. Following this the space charge properties are calculated using a one-dimensional Poisson-Boltzmann solver which makes certain assumptions about the system.

9.1 Potential errors in segregation energy calculations

9.1.1 Constructing the grain boundary

The defect segregation energies depend on the geometry of the grain boundary, which in turn depends on how the grain boundary is constructed. The geometry of the grain boundary can be predicted using energy minimisation techniques, such as static lattice energy minimisation. In this energy minimisation technique, a fine 2D mesh is placed over the grain boundary and the two regions are moved onto each point on the mesh, altering the position of one crystal domain parallel to grain boundary with respect to the other. The energies are calculated at each mesh point and the optimum structure is that with the lowest calculated energy. The grain boundary orientation produced can also be compared to experimental observations of grain boundary structures. Grain boundary orientations can be determined experimentally using scanning tunnel microscopy and the lowest energy structures are those most likely to be found in real crystalline samples.

9.1.2 Segregation energy calculations

Density functional theory calculations offer high levels of accuracy, which increase further depending on the choice of exchange correlation functional, however the improved accuracy comes with a extremely high computational cost which limits the size of the simulation cell significantly. A prevalent issue with a limited simulation cell is having sufficient screening between a defect inserted at a site and the 'bulk-like' region. This could result in truncation errors which could limit the accuracy of the data. Classical calculations are relatively less accurate, and are only as accurate as the choice of potential model, but considerably computationally cheaper. The lower computational expense allows a significantly larger cell to be simulated, increasing confidence that the defects extend into the 'bulk-like' region, and all relevant interactions have been considered. To improve the accuracy of the classical simulations, the Mott-Littleton method implements convergence testing so the calculations can be verified as accurate to a desired level.

9.2 Potential errors in 1D modelling

Using a finite difference approximation will incorporate some error into the results from the calculation. In the continuum model, the accuracy can be improved by finer grid, although that will increase the computational expense of the calculation. Another method to improve the accuracy of the finite difference approximation is to use a higher order finite difference expansion which goes beyond using only the nearest neighbour information on the grid.

The Poisson-Boltzmann model makes certain assumptions about the crystalline system. In typical continuum analysis, it is assumed that there is no structural change in the sample from the bulk into the interface, although the structural changes are included in the site-explicit model used in this work. It also assumes that the system consists of dilute point defects with no interactions other than electrostatics. It has been found in this work that in some cases, even when the bulk defect concentration is in the dilute regime that the grain boundary core becomes completely saturated with defects. In this case, the system cannot be considered dilute and the structural impact would be significant. It is therefore important to include defect-defect interaction terms in the model to account for this behaviour. Other assumptions include that the defect mobility remains constant between the bulk and the grain boundary which may impact the results of the Poisson-Boltzmann model.

Using a more resolute finite difference approximation and including defect-defect interaction terms are discussed in more detail with the expansion of this work in chapter 10.

Chapter 10

Extending this work

10.1 Investigate other relevant materials

Space charge formation in solid electrolytes for solid oxide fuel cells has been extensively reviewed, however space charge formation is only recently being considered in materials for use in solid state batteries and other electrochemical devices. In this thesis, space charge formation is discussed in the Li_3OCl antiperovskite, which was until recently proposed as a potential solid electrolyte for use in lithium solid state batteries. It was found that there is a large space charge effect at grain boundaries in Li_3OCl and therefore, this work acts as a proof of concept that space charge formation may be a considerable factor in improving the conductivity of solid electrolytes for all applications. It is important to fully understand all aspects of the defect behaviour, including space charge formation, in these materials to fully optimise ionic transport and improve the properties of electrochemical devices. Due to the generalised nature of PYSCSES, the python code written to calculate the space charge properties discussed in this work, a natural way to extend this project would be to look at a broad range of materials and assess the impact of the formation of space charge regions.

10.2 Improving the finite difference approximation

The work discussed in this thesis uses a second order finite difference approximation to solve the second order partial differential Poisson-Boltzmann equation. This approach approximates the differential by converting it to a set of linear difference equations using the grid points either side of the point of interest. The approximation used in this work uses

the single nearest grid point either side of the point of interest, however the approximation can be improved by including multiple grid points extending from the point of interest. The finite difference approximation is obtained using a Taylor series,

$$f_{x+1} = \sum_{n=0}^{\infty} \frac{f_x^{(n)} \cdot \Delta x^n}{n!} \tag{10.1}$$

The typical finite difference approximation uses the first three terms of the Taylor series and gives,

$$f'_x = \frac{f_{x+1} - f_{x-1}}{2\Delta x} \tag{10.2}$$

for the first derivative and

$$f''_x = \frac{f_{x+1} - 2f_x + f_{x-1}}{\Delta x^2} \tag{10.3}$$

for the second derivative.

Higher order approximations to the derivatives can be obtained by using more terms in the Taylor series. Using the next term in the Taylor series leads to an expression which takes into account two grid points either side of the point of interest. For the first derivative,[226]

$$f'_x = \frac{-f_{x+2} + 8f_{x+1} - 8f_{x-1} + f_{x-2}}{12\Delta x}, \tag{10.4}$$

and the second derivative,

$$f''_x = \frac{-f_{x+2} + 16f_{x+1} - 30f_x + 16f_{x-1} - f_{x-2}}{12\Delta x^2}. \tag{10.5}$$

There are advantages and disadvantages to using a higher order finite difference approximation. The advantages include improved accuracy due to the higher resolution, however it comes with disadvantages due to the increased number of grid points used. The higher order approximation expands the linear equations and a tridiagonal matrix will no longer by suitable. Using a larger matrix can significantly increase the computational cost and therefore a balance is required between higher accuracy and higher overhead expense.[227]

10.3 Increasing the dimensionality of the model

The Poisson-Boltzmann equation is typically solved using a finite difference approximation on a one-dimensional grid. The model can be extended by implementing a finite difference approximation on a two-dimensional computational grid as shown in figure 10.1

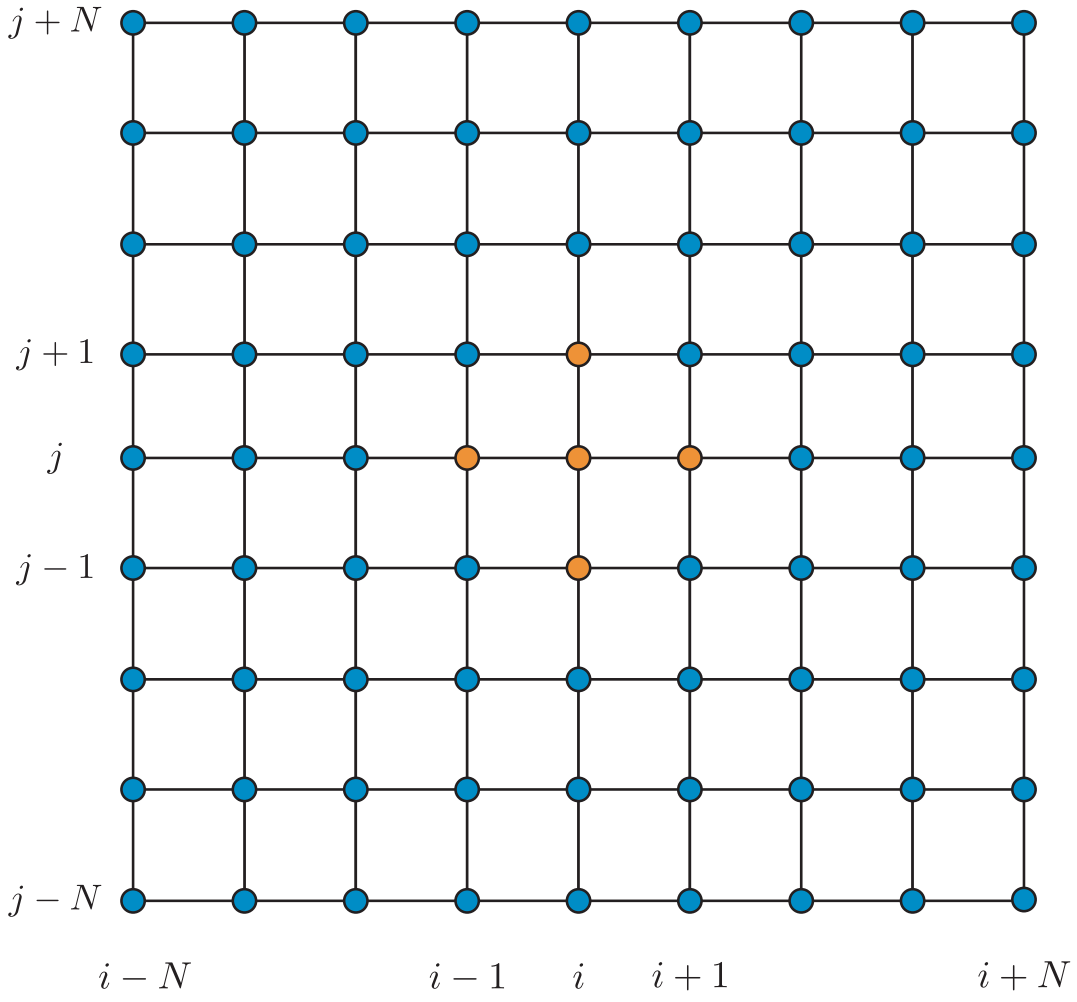

Figure 10.1: 2D finite difference grid using a uniform grid spacing. The stencil for one of the computational grids is highlighted in orange.

The grid points must be referred to using a two-integer index (i, j), and the finite difference equation becomes

$$f''_{(i,j)} = \frac{f_{i-1,j} - 2f_{i,j} + f_{i+1,j}}{\Delta x^2} + \frac{f_{i,j-1} - 2f_{i,j} + f_{i,j+1}}{\Delta y^2}. \tag{10.6}$$

Using the two-dimensional Poisson-Boltzmann solver would allow the electrostatic po-

tential to be calculated as a surface, rather than a one-dimensional profile. The model can be extended further as a three-dimensional finite difference model to calculate the electrostatic potential at all sites in a crystal structure,

$$f''_{(i,j,k)} = \frac{f_{i-1,j,k} - 2f_{i,j,k} + f_{i+1,j,k}}{\Delta x^2} + \frac{f_{i,j-1,k} - 2f_{i,j,k} + f_{i,j+1,k}}{\Delta y^2} + \frac{f_{i,j,k-1} - 2f_{i,j,k} + f_{i,j,k+1}}{\Delta z^2}. \tag{10.7}$$

Due to the increasing number of points as the model extends from one-dimensional to three-dimensional, the computational cost of running the calculation will increase significantly, and therefore for systems where the defect segregation energies do not change on equivalent sites in the crystal structure, it is not necessary to calculate the electrostatic potential using a higher dimensional finite difference approximation, although it would be interesting to explore these higher dimensional approximations to verify whether the values obtained from the calculations vary.

10.4 Including all defect species

Recent work carried out by Squires *et al.*[101] suggests that defect species present in solid electrolytes are not necessarily stoichiometric pairs such as Schottky and Frenkel defect pairs, but exist as a more complex combination of defect species. This suggests that to assume that the mobile charge carriers in a material are balanced by a single charge compensating defect may be an oversimplification of the system. A potential route for extending the work in this thesis would be to calculate all of the possible defect species in the system, their bulk concentrations and their defect segregation energies and calculate the space charge properties. The results would include the influence from each defect species present in the system, and give a more realistic model of the defect behaviour at, and around grain boundaries in solid electrolytes.

10.5 Inclusion of defect-defect interaction terms

The standard Poisson-Boltzmann approach to modelling grain boundaries only includes electrostatic interactions between defects. A potential route for extending the work carried out in this thesis is to include defect-defect interaction terms in the model. Mebane and De Souza[168] have discussed how the Poisson-Boltzmann approach assumes that points defects are dilute, non-interacting (except electrostatics) moieties and that space charge layers are

assumed to be regions of constant defect mobilities, but with altered defect concentrations. At low defect concentrations, these are reasonable assumptions but as the concentration increases (approximately above 1% dopant concentration), defect–defect interactions must be taken into consideration. In the study they give a framework which is able to model defect redistribution at boundaries over a range of defect concentrations from dilute to concentrated solid solutions. In their model, they replace the Boltzmann model with the Cahn-Hilliard theory of inhomogenous systems,[169] producing what they refer to as the "Poisson-Cahn theory".

$$\mu = \mu_v + f_{vv}n_v + f_{av}n_a + RT\ln\frac{n_v}{1-n_v} + zF\Phi - \beta_v\nabla^2 n_a \tag{10.8}$$

Where a refers to dopant ions and v refers to defects. μ is the electrochemical potential μ_v is the standard chemical potential, f_{vv} is the direct self interaction energies, f_{av} is the dopant-vacancy interaction energy, β_v is the gradient energy coefficient and n_v and n_a are the site fractions.

Compared to Boltzmann statistics:

$$\mu = RT\ln n_v + zF\Phi \tag{10.9}$$

and correct site statistics:

$$\mu = RT\ln\frac{n_v}{1-n_v} + zF\Phi. \tag{10.10}$$

They state that following this, the condition for equilibrium is, as with the Poisson-Boltzmann approach, that the electrochemical potentials for all mobile defects are constant throughout the system and the electrostatic potential follows Poisson's equation. Concluding that the model conforms to the dilute Poisson-Boltzmann case for low dopant concentrations, as at low dopant concentrations n_a and n_v tend to zero and therefore $\mu \longrightarrow \mu_v + RT\ln\frac{n_v}{1-n_v} + zF\Phi$ which is the non-interacting case. Whilst the model also conforms to the results of atomistic simulation in the concentrated case.

Including these defect-defect interaction terms would be beneficial, as it would give a more accurate representation of the defect behaviour in a real solid electrolyte. The approach outlined by Mebane and De Souza cannot be directly applied to a model whereby the free

energy is minimised by converting the system into a set of couple differential equations due to the curvature in the concentration term not being accessible through atomistic calculation. Therefore an extension to the work outlined in this thesis would be to explore other routes for minimising the free energy of the system that can be incorporated into the current Poisson-Boltzmann solver infrastructure to allow inclusion of the defect-defect interaction terms.

Chapter 11

Overall conclusions

The objective for the work carried out in this project was to bridge atomistic and continuum models, in order to create a robust, physically more accurate space charge model. This was achieved by using site explicit defect positions and defect segregation energies obtained through atomistic process, either classical or first principles calculations as the input for a continuum Poisson-Boltzmann model, ending up with a space charge model that could account for the explicit crystalline structure of the lattice and the explicit structural distortion at the grain boundary core. Over time this model became a piece of open source software, known as PYSCSES.

Throughout the case studies it has been consistently found that including the explicit crystalline structure of the system is of importance when calculating space charge properties, as it reduces the level of assumption made regarding the behaviour of defects in the system. The three main models commonly found in the literature include the use of a continuum model with a single core segregation energy, a continuum model with a core described using layered segregation energies and a site explicit model using all segregation energies. The comparison of the site explicit solver with other commonly used models allowed an observation of how the calculated space charge results vary with the choice of model. It was found that the choice of space charge model can strongly affect the calculated space charge properties, indicating that including information about the explicit lattice structure of the system is necessary for a more complete visualisation of the space charge properties, particularly the calculated defect distribution and the respective calculated ionic conductivity.

The space charge properties have been calculated for both a well known and well doc-

umented solid oxide fuel cell structure Gd-doped CeO_2, where space charge formation has been extensively studied, and a relatively novel potential solid electrolyte for use in solid state lithium ion batteries, the anti-perovskite Li_3OCl, where space charge formation has not previously been considered. In both cases, the presence of grain boundaries have a large impact on the space charge properties and ionic conductivities of the material. In $Gd-CeO_2$ mobile oxygen vacancies segregate to the grain boundary core, resulting in a depletion of oxygen vacancies in the space charge regions, and in Li_3OCl the mobile lithium vacancies segregate to the grain boundary core, resulting in a depletion of lithium vacancies in the space charge regions. The depletion of mobile charge carriers in the space charge regions causes a significant reduction in the ionic conductivity of the materials. For both cases, it was also found that the ionic conductivity varies significantly with grain boundary orientation. This reinforces the need to consider the explicit crystalline structure of the grain boundary, rather than assuming some 'average' behaviour for the sample. It can be predicted that engineering the types of grain boundary present in a sample can allow the refining of material properties, including improving the ionic conductivity and thus the performance of electrochemical devices.

The effect of grain boundary separation has also been investigated as nanocrystalline materials display a wide functional diversity and exhibit enhanced properties compared to bulk materials. In nanocrystalline materials, the space charge width is greater than the distance between the interfaces which results in a material where the space charge regions overlap and the material becomes charged throughout. Dual grain boundary systems were created at a range of inter-grain boundary distances and the space charge overlap was observed. The depletion in the space charge region due to the overlap of charge causes an enhanced mobile charge carrier depletion and thus it was found that as the distance between grain boundaries was decreased, the ionic conductivity of the material decreased. In this case, the results from the Poisson-Boltzmann solver disagree with experimental observations as it is often reported that the ionic conductivity of a material is increased in nanocrystalline systems, however the results do agree with theoretical predictions.

Overall, it can be argued that including site explicit defect information in the modelling of space charge regions is of significant benefit as it reduces the assumptions made about the crystal structure, such as that defects exist as point charges in an electrostatic continuum, therefore the objectives set out at the beginning of this project have been successfully met. While the combined atomistic and continuum model described in this work has improved reliability over some other models, some assumptions are made. Going forward

in modelling space charge regions it is important to address more of the assumptions, such as including defect-defect interaction terms, in order to produce a more reliable and physically more accurate theoretical space charge model.

Appendix A

Experimental Analysis of Space Charge Regions

A.1 Electrochemical impedance spectroscopy

Electrochemical impedance spectroscopy is a powerful method for characterising the dynamics of mobile charge carriers in bulk and boundary regions in solid electrolytes. The general approach is to apply an electrical stimulus to the sample and observe the response.[228] The typical approach to measuring boundary properties is to apply a sinusoidal voltage,

$$V(t) = \bar{V} + \hat{V} \cdot \sin(\omega t), \tag{A.1}$$

to the interface and measure the phase shift and amplitude of the resulting current,

$$I(t) = \bar{I} + \hat{I} \cdot \sin(\omega t + \phi). \tag{A.2}$$

The complex impedance is calculated as

$$Z(j\omega) = \frac{V(j\omega)}{I(j\omega)} = \frac{\hat{V}}{\hat{I}} \cdot \exp -j\phi = |Z| \cdot \exp j \cdot \mathrm{Arg}(z), \tag{A.3}$$

$$Z(j\omega) = \mathrm{Re}(Z) + j \cdot \mathrm{Im}(Z), \tag{A.4}$$

where $\hat{V}$ and $\hat{I}$ are the voltage and current amplitude, $\bar{V}$ and $\bar{I}$ are the voltage and current direct current values, ω is the angular frequency ($\omega = 2\pi f$, with f as the test signal frequency), ϕ is the phase difference between $V(t)$ and $I(t)$, $V(j\omega)$ and $I(j\omega)$ are the Steinmetz transformations of $V(t)$ and $I(t)$.[229] The sine wave parameters can be calculated using fast Fourier transform analysis or using a fitting algorithm in the time domain.[228]

The data from electrochemical impedance spectroscopy is often displayed as a Nyquist plot – the parametric plot of a frequency response. The real part of the function is plotted on the x axis and the imaginary part of the function on the y axis, so that each point describes the complex impedance at one frequency.

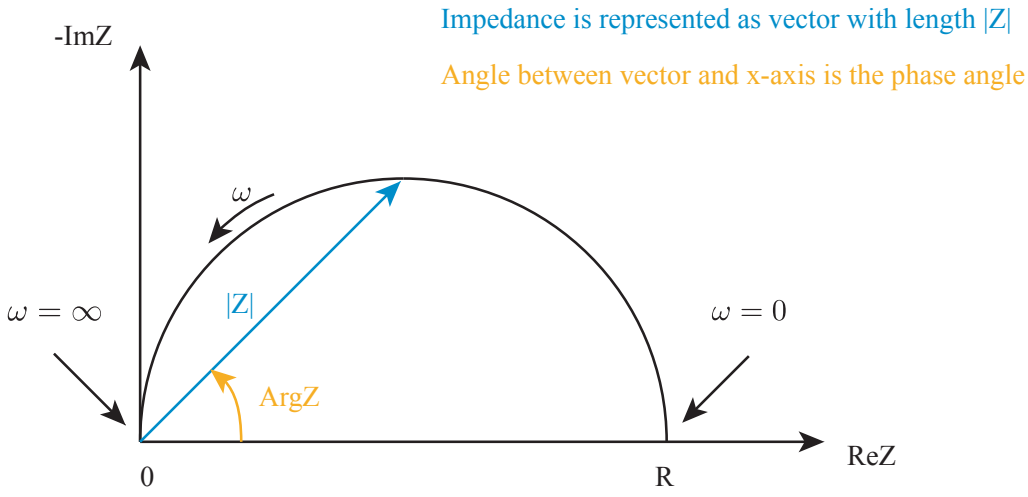

Figure A.1: Example impedance spectroscopy schematic

The impedance spectrum of a resistor and capacitor in parallel is then a semicircular arc, where the frequency increases from right to left. The arc diameter (along the real axis) corresponds to the resistance.[230] Electrochemical impedance spectra can be analysed using equivalent circuit models, consisting of a resistor (R) and capacitance (C) elements. Bauerle developed an equivalent circuit model for ionically conducting ceramics with resistive grain boundaries in 1969, which modelled their dual-arc impedance response.[231] Polycrystalline materials exhibit semi-circles for both bulk and grain boundary impedances and can be represented by the equivalent circuit model shown in figure A.2.[232]

The low frequency intercept on the real axis corresponds to the total resistivity of the material[199] .

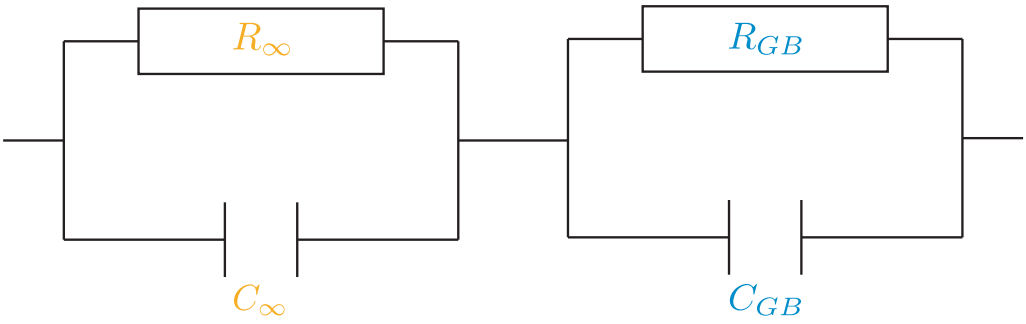

Figure A.2: Equivalent circuit representation of polycrystalline materials with bulk and grain boundary impedances.

The bulk conductivity σ_∞ can be obtained can be calculated as,

$$\sigma_\infty = \frac{1}{R_\infty}\left(\frac{l}{A}\right), \tag{A.5}$$

where l and A denote the distance between electrodes and electrode area respectively, R is the resistance and C is the capacitance. The grain boundary conductivity can be calculated as,

$$\sigma_{GB} = \left(\frac{\tau_\infty}{\tau_{GB}}\right)\sigma_\infty, \tag{A.6}$$

where $\tau = RC$.[198]

A.2 Brick-layer model

Ionic conductivity of a polycrystalline solid electrolyte includes both bulk and grain boundary contributions, and both of these contributions must be included to describe experimental measurement. Beekmans and Heyne developed the brick-layer model corresponding to the Bauerle equivalent circuit model.[233] This model consists of conducting bricks (bulk regions) surrounded by resistive mortar (grain boundaries).[230] There are two possible paths for ionic movement through the model depending on the ionic conductivity of the grain respective to the grain boundary. If the bulk ionic conductivity is much greater than the grain boundary ionic conductivity, and the grain boundary width is negligibly small, the ions will move through the bulk and across the grain boundaries. In this case, the contributions of the parallel path (figure A.3) can be neglected and the Bauerle equivalent

circuit can be implemented.[234] However, if the conductivity along the grain boundary is much greater than the conductivity in the bulk, the ions will move along the grain boundary and the parallel path must be considered.[235]

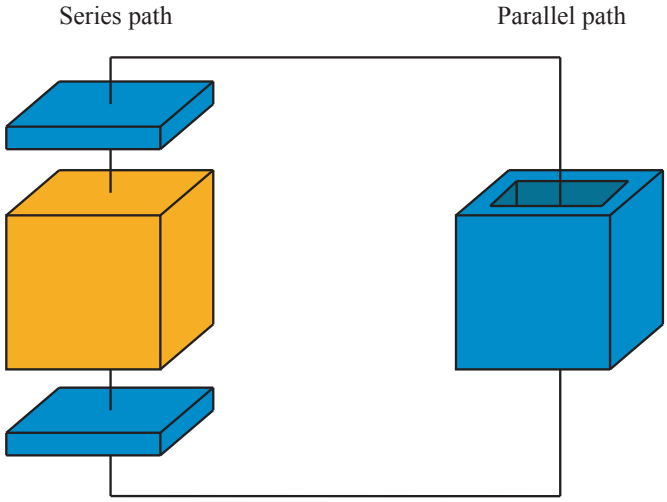

Figure A.3: A schematic of the brick-layer model representing the series and parallel conduction paths.

Bibliography

[1] W. Colella, R. O'Hayre, F. B. Prinz, and S. W. Cha, *Fuel Cell Fundamentals*. John Wiley and Sons Ltd., 2016.

[2] R. Tilley, *Crystals and Crystal Structures*. Wiley, 2006.

[3] K. J. Buschow, R. W. Cahn, M. C. Flemings, B. Ilschner, E. J. Kramer, and S. Mahajan, "Encyclopedia of materials," *Science and technology*, vol. 1, p. 11, 2001.

[4] P. Bruce, *Solid State Electrochemistry*. Chemistry of Solid State Materials, Cambridge University Press, 1997.

[5] N. J. de Klerk, E. van der Maas, and M. Wagemaker, "Analysis of diffusion in solid-state electrolytes through md simulations, improvement of the li-ion conductivity in β-li3ps4 as an example," *ACS applied energy materials*, vol. 1, no. 7, pp. 3230–3242, 2018.

[6] E. D. Wachsman and K. T. Lee, "Lowering the temperature of solid oxide fuel cells," *Science*, vol. 334, no. 6058, pp. 935–939, 2011.

[7] R. M. Ormerod, "Solid oxide fuel cells," *Chemical Society Reviews*, vol. 32, no. 1, pp. 17–28, 2003.

[8] J. A. Dawson, P. Canepa, T. Famprikis, C. Masquelier, and M. S. Islam, "Fundamentals of inorganic solid-state electrolytes for batteries," *Nature Materials*, pp. 1476–4660, 2019.

[9] J. Janek and W. G. Zeier, "A solid future for battery development," *Energy*, vol. 500, no. 400, p. 300, 2016.

[10] K. Schmidt-Rohr, "Why combustions are always exothermic, yielding about 418 kj per mole of o2," *Journal of Chemical Education*, vol. 92, no. 12, pp. 2094–2099, 2015.

[11] R. Khurmi and R. Sedha, "Textbook of material science," *S. Chand and Company Ltd. Ram Niger, New Delhi-110055*, 2005.

[12] W. G. E. M.A., "Xxiv. on voltaic series and the combination of gases by platinum," *The London, Edinburgh, and Dublin Philosophical Magazine and Journal of Science*, vol. 14, no. 86-87, pp. 127–130, 1839.

[13] N. Jaiswal, K. Tanwar, R. Suman, D. Kumar, S. Upadhyay, and O. Parkash, "A brief review on ceria based solid electrolytes for solid oxide fuel cells," *Journal of Alloys and Compounds*, vol. 781, pp. 984 – 1005, 2019.

[14] E. Groove, "Fuel cells." Accessed 2019-23-09.

[15] D. E. Curtin, R. D. Lousenberg, T. J. Henry, P. C. Tangeman, and M. E. Tisack, "Advanced materials for improved pemfc performance and life," *Journal of power Sources*, vol. 131, no. 1-2, pp. 41–48, 2004.

[16] L. Roen, C. Paik, and T. Jarvi, "Electrocatalytic corrosion of carbon support in pemfc cathodes," *Electrochemical and Solid-State Letters*, vol. 7, no. 1, pp. A19–A22, 2004.

[17] P. Stonehart, "Development of alloy electrocatalysts for phosphoric acid fuel cells (pafc)," *Journal of Applied electrochemistry*, vol. 22, no. 11, pp. 995–1001, 1992.

[18] S. R. Choudhury, M. Deshmukh, and R. Rengaswamy, "A two-dimensional steady-state model for phosphoric acid fuel cells (pafc)," *Journal of power sources*, vol. 112, no. 1, pp. 137–152, 2002.

[19] G. McLean, T. Niet, S. Prince-Richard, and N. Djilali, "An assessment of alkaline fuel cell technology," *International Journal of Hydrogen Energy*, vol. 27, no. 5, pp. 507–526, 2002.

[20] B. Lin, L. Qiu, J. Lu, and F. Yan, "Cross-linked alkaline ionic liquid-based polymer electrolytes for alkaline fuel cell applications," *Chemistry of materials*, vol. 22, no. 24, pp. 6718–6725, 2010.

[21] L. Plomp, J. Veldhuis, E. Sitters, and S. Van der Molen, "Improvement of molten-carbonate fuel cell (mcfc) lifetime," *Journal of power sources*, vol. 39, no. 3, pp. 369–373, 1992.

[22] P. Tomczyk, "Mcfc versus other fuel cells - characteristics, technologies and prospects," *Journal of Power sources*, vol. 160, no. 2, pp. 858–862, 2006.

[23] S. C. Singhal, "Advances in solid oxide fuel cell technology," *Solid state ionics*, vol. 135, no. 1-4, pp. 305–313, 2000.

[24] D. J. Brett, A. Atkinson, N. P. Brandon, and S. J. Skinner, "Intermediate temperature solid oxide fuel cells," *Chemical Society Reviews*, vol. 37, no. 8, pp. 1568–1578, 2008.

[25] R. Rosli, A. B. Sulong, W. R. W. Daud, M. A. Zulkifley, T. Husaini, M. I. Rosli, E. Majlan, and M. Haque, "A review of high-temperature proton exchange membrane fuel cell (ht-pemfc) system," *International Journal of Hydrogen Energy*, vol. 42, no. 14, pp. 9293–9314, 2017.

[26] O. Yamamoto, "Solid oxide fuel cells: fundamental aspects and prospects," *Electrochimica Acta*, vol. 45, no. 15-16, pp. 2423–2435, 2000.

[27] A. B. Stambouli and E. Traversa, "Solid oxide fuel cells (sofcs): a review of an environmentally clean and efficient source of energy," *Renewable and sustainable energy reviews*, vol. 6, no. 5, pp. 433–455, 2002.

[28] A. R. West, "Solid electrolytes and mixed ionic-electronic conductors: an applications overview," *J. Mater. Chem.*, vol. 1, pp. 157–162, 1991.

[29] A. J. Jacobson, "Materials for solid oxide fuel cells," *Chemistry of Materials*, vol. 22, no. 3, pp. 660–674, 2009.

[30] S. C. Singhal and K. Kendall, *High-temperature solid oxide fuel cells: fundamentals, design and applications*. Elsevier, 2003.

[31] A. Orera and P. Slater, "New chemical systems for solid oxide fuel cells," *Chemistry of Materials*, vol. 22, no. 3, pp. 675–690, 2009.

[32] N. Mahato, A. Banerjee, A. Gupta, S. Omar, and K. Balani, "Progress in material selection for solid oxide fuel cell technology: A review," *Progress in Materials Science*, vol. 72, pp. 141–337, 2015.

[33] R. Doshi, V. L. Richards, J. Carter, X. Wang, and M. Krumpelt, "Development of solid-oxide fuel cells that operate at 500c," *Journal of The Electrochemical Society*, vol. 146, no. 4, pp. 1273–1278, 1999.

[34] M. K. Mahapatra and P. Singh, "Chapter 24 - fuel cells: Energy conversion technology," in *Future Energy (Second Edition)* (T. M. Letcher, ed.), pp. 511 – 547, Boston: Elsevier, second edition ed., 2014.

[35] G. Pistoria, *Batteries for Portable Devices*. Elsevier, 2005.

[36] J. W. Fergus, "Recent developments in cathode materials for lithium ion batteries," *J. Power Sources*, vol. 195, no. 4, pp. 939 – 954, 2010.

[37] L. Pauling, "15: Oxidation-reduction reactions; electrolysis," *General Chemistry*, p. 539, 1988.

[38] K. Schmidt-Rohr, "How batteries store and release energy: Explaining basic electrochemistry," *Journal of Chemical Education*, vol. 95, no. 10, pp. 1801–1810, 2018.

[39] B. Kang and G. Ceder, "Battery materials for ultrafast charging and discharging," *Nature*, vol. 458, no. 7235, p. 190, 2009.

[40] "Understanding the factors in the lithium battery equation." `https://www.electronicdesign.com/power/understanding-factors-lithium-battery-equation`. Accessed: 2019-09-09.

[41] S. P. Ong, V. L. Chevrier, G. Hautier, A. Jain, C. Moore, S. Kim, X. Ma, and G. Ceder, "Voltage, stability and diffusion barrier differences between sodium-ion and lithium-ion intercalation materials," *Energy & Environmental Science*, vol. 4, no. 9, pp. 3680–3688, 2011.

[42] A. Bhatt, R. Withers, and G. Wang, "Lithium ion batteries." https://www.science.org.au/curious/technology-future/lithium-ion-batteries. Accessed: 2019-09-09.

[43] "How batteries work." `https://engineering.mit.edu/engage/ask-an-engineer/how-does-a-battery-work/`. Accessed: 2019-01-30.

[44] "Letter to peter collinson." `http://franklinpapers.org/framedVolumes.jsp`. Accessed: 2019-01-30.

[45] M. Winter, B. Barnett, and K. Xu, "Before li ion batteries," *Chemical Reviews*, vol. 118, no. 23, pp. 11433–11456, 2018.

[46] W. Li, J. R. Dahn, and D. S. Wainwright, "Rechargeable lithium batteries with aqueous electrolytes," *Science*, vol. 264, no. 5162, pp. 1115–1118, 1994.

[47] Y. Nishi, "The development of lithium ion secondary batteries," *The Chemical Record*, vol. 1, no. 5, pp. 406–413, 2001.

[48] F. Zheng, M. Kotobuki, S. Song, M. O. Lai, and L. Lu, "Review on solid electrolytes for all-solid-state lithium-ion batteries," *Journal of Power Sources*, vol. 389, pp. 198 – 213, 2018.

[49] C. Chen, S. Xie, E. Sperling, A. Yang, G. Henriksen, and K. Amine, "Stable lithium ion conducting perovskite lithium strontium tantalum zirconium oxide system," *Solid State Ionics*, vol. 167, no. 3, pp. 263 – 272, 2004.

[50] N. Anantharamulu, K. K. Rao, G. Rambabu, B. V. Kumar, V. Radha, and M. Vithal, "A wide-ranging review on nasicon type materials," *Journal of materials science*, vol. 46, no. 9, pp. 2821–2837, 2011.

[51] L. S. Plashnitsa, E. Kobayashi, Y. Noguchi, S. Okada, and J.-i. Yamaki, "Performance of nasicon symmetric cell with ionic liquid electrolyte," *Journal of the Electrochemical Society*, vol. 157, no. 4, pp. A536–A543, 2010.

[52] K. Nanjundaswamy, A. Padhi, J. Goodenough, S. Okada, H. Ohtsuka, H. Arai, and J. Yamaki, "Synthesis, redox potential evaluation and electrochemical characteristics of nasicon-related-3d framework compounds," *Solid State Ionics*, vol. 92, no. 1-2, pp. 1–10, 1996.

[53] R. Kanno, T. Hata, Y. Kawamoto, and M. Irie, "Synthesis of a new lithium ionic conductor, thio-lisicon–lithium germanium sulfide system," *Solid State Ionics*, vol. 130, no. 1-2, pp. 97–104, 2000.

[54] M. Murayama, R. Kanno, M. Irie, S. Ito, T. Hata, N. Sonoyama, and Y. Kawamoto, "Synthesis of new lithium ionic conductor thio-lisicon-lithium silicon sulfides system," *Journal of Solid State Chemistry*, vol. 168, no. 1, pp. 140–148, 2002.

[55] M. Nagao, Y. Imade, H. Narisawa, T. Kobayashi, R. Watanabe, T. Yokoi, T. Tatsumi, and R. Kanno, "All-solid-state li–sulfur batteries with mesoporous electrode and thio-lisicon solid electrolyte," *Journal of Power Sources*, vol. 222, pp. 237–242, 2013.

[56] A. C. Kozen, A. J. Pearse, C.-F. Lin, M. Noked, and G. W. Rubloff, "Atomic layer deposition of the solid electrolyte lipon," *Chemistry of Materials*, vol. 27, no. 15, pp. 5324–5331, 2015.

[57] W. West, J. Whitacre, and J. Lim, "Chemical stability enhancement of lithium conducting solid electrolyte plates using sputtered lipon thin films," *Journal of power sources*, vol. 126, no. 1-2, pp. 134–138, 2004.

[58] B. Morgan, "Lattice-geometry effects in garnet solid electrolytes: A lattice-gas monte carlo simulation study," *Royal Society Open Science*, vol. 4, 11 2017. Invited contribution to "Young Talent" special issue.

[59] M. Burbano, D. Carlier, F. Boucher, B. J. Morgan, and M. Salanne, "Sparse cyclic excitations explain the low ionic conductivity of stoichiometric li 7 la 3 zr 2 o 12," *Physical review letters*, vol. 116, no. 13, p. 135901, 2016.

[60] V. Thangadurai, S. Narayanan, and D. Pinzaru, "Garnet-type solid-state fast li ion conductors for li batteries: critical review," *Chemical Society Reviews*, vol. 43, no. 13, pp. 4714–4727, 2014.

[61] W. Zhang, G. E. Eperon, and H. J. Snaith, "Metal halide perovskites for energy applications," *Nature Energy*, vol. 1, no. 6, p. 16048, 2016.

[62] J. Suntivich, H. A. Gasteiger, N. Yabuuchi, H. Nakanishi, J. B. Goodenough, and Y. Shao-Horn, "Design principles for oxygen-reduction activity on perovskite oxide catalysts for fuel cells and metal–air batteries," *Nature chemistry*, vol. 3, no. 7, p. 546, 2011.

[63] P. Verma, P. Maire, and P. Novák, "A review of the features and analyses of the solid electrolyte interphase in Li-ion batteries," *Electrochim. Acta*, vol. 55, no. 22, pp. 6332 – 6341, 2010.

[64] P. P. Kumar and S. Yashonath, "Ionic conduction in the solid state," *Journal of Chemical Sciences*, vol. 118, no. 1, pp. 135–154, 2006.

[65] D. Baril, C. Michot, and M. Armand, "Electrochemistry of liquids vs. solids: Polymer electrolytes," *Solid State Ionics*, vol. 94, no. 1-4, pp. 35–47, 1997.

[66] D. Almond, G. Duncan, and A. West, "The determination of hopping rates and carrier concentrations in ionic conductors by a new analysis of ac conductivity," *Solid State Ionics*, vol. 8, no. 2, pp. 159–164, 1983.

[67] C. León, M. Lucia, and J. Santamaria, "Correlated ion hopping in single-crystal yttria-stabilized zirconia," *Physical Review B*, vol. 55, no. 2, p. 882, 1997.

[68] M. Nolan, J. E. Fearon, and G. W. Watson, "Oxygen vacancy formation and migration in ceria," *Solid State Ionics*, vol. 177, no. 35-36, pp. 3069–3074, 2006.

[69] A. P. Levanyuk and A. S. Sigov, "Defects and structural phase transitions," 1988.

[70] H. Van Swygenhoven, "Grain boundaries and dislocations," *Science*, vol. 296, no. 5565, pp. 66–67, 2002.

[71] G. Hasson, J.-Y. Boos, I. Herbeuval, M. Biscondi, and C. Goux, "Theoretical and experimental determinations of grain boundary structures and energies: Correlation with various experimental results," *Surface Science*, vol. 31, pp. 115–137, 1972.

[72] J. Maier, "Ionic conduction in space charge regions," *Prog. Sol. Stat. Chem.*, vol. 23, no. 3, pp. 171–263, 1995.

[73] J. Fleig, F. Noll, and J. Maier, "Surface conductivity measurements on agcl single crystals using microelectrodes," *Berichte der Bunsengesellschaft für physikalische Chemie*, vol. 100, no. 5, pp. 607–615, 1996.

[74] J. Maier, "Defect chemistry and conductivity effects in heterogeneous solid electrolytes," *J. Electrochem. Soc.*, vol. 134, no. 6, pp. 1524–1535, 1987.

[75] J. Maier, "On the conductivity of polycrystalline materials," *Ber. Bunsen. Phys. Chem.*, vol. 90, no. 1, pp. 26–33, 1986.

[76] M. Acosta, F. Baiutti, A. Tarancnd J. L. MacManus-Driscoll, "Nanostructured materials and interfaces for advanced ionic electronic conducting oxides," *Advanced Materials Interfaces*, vol. 6, no. 15, p. 1900462, 2019.

[77] J. Maier, "On the electronic conductivity of composite electrolytes," *Solid State Ionics*, vol. 28, pp. 1073–1077, 1988.

[78] J. Maier, "Pushing nanoionics to the limits: charge carrier chemistry in extremely small systems," *Chemistry of materials*, vol. 26, no. 1, pp. 348–360, 2013.

[79] P. Knauth, "Ionic conductor composites: theory and materials," *Journal of electroceramics*, vol. 5, no. 2, pp. 111–125, 2000.

[80] Z. Mišković and N. Upadhyaya, "Modeling electrolytically top-gated graphene," *Nanoscale research letters*, vol. 5, no. 3, p. 505, 2010.

[81] J. Wang, M. Wang, and Z. Li, "Lattice poisson–boltzmann simulations of electro-osmotic flows in microchannels," *Journal of Colloid and Interface Science*, vol. 296, no. 2, pp. 729–736, 2006.

[82] B. Li and D. Y. Kwok, "A lattice boltzmann model for electrokinetic microchannel flow of electrolyte solution in the presence of external forces with the poisson–boltzmann

equation," *International Journal of Heat and Mass Transfer*, vol. 46, no. 22, pp. 4235–4244, 2003.

[83] W. Dreyer, C. Guhlke, and R. Müller, "Overcoming the shortcomings of the nernst–planck model," *Physical Chemistry Chemical Physics*, vol. 15, no. 19, pp. 7075–7086, 2013.

[84] D. C. Sayle and G. W. Watson, "The atomistic structures of mgo/srtio3(001) and bao/srtio3(001) using simulated amorphization and recrystallization," *The Journal of Physical Chemistry B*, vol. 105, no. 23, pp. 5506–5514, 2001.

[85] D. C. Sayle, J. A. Doig, S. C. Parker, and G. W. Watson, "Synthesis, structure and ionic conductivity in nanopolycrystalline baf2/caf2 heterolayers," *Chem. Commun.*, pp. 1804–1806, 2003.

[86] B. J. Morgan and P. A. Madden, "Molecular dynamics simulation of ionic transport at coherent interfaces in fluorite heterostructures," *Phys. Rev. B*, vol. 89, p. 054304, Feb 2014.

[87] J. A. Dawson, P. Canepa, T. Famprikis, C. Masquelier, and M. S. Islam, "Atomic-scale influence of grain boundaries on li-ion conduction in solid electrolytes for all-solid-state batteries," *Journal of the American Chemical Society*, vol. 140, no. 1, pp. 362–368, 2018. PMID: 29224340.

[88] W. G. and M. B., "pyscses, a python site explicit solver," *Journal of Open Source Software*, vol. 4, no. 1290, p. 35, 2019.

[89] W. Hume-Rothery, "The structure of metals and alloys," *Indian Journal of Physics*, vol. 11, pp. 74–74, 1969.

[90] W. A. Wooster, *A text-book on crystal physics*. Cambridge University Press, 2016.

[91] V. L. Amirita, "Crystal structure." Accessed 2019-19-09.

[92] A. R. West, *Basic Solid State Chemistry*. Wiley, 1999.

[93] T. C. Mak and G.-D. Zhou, "Crystallography in modern chemistry. a resource book of crystal structures," *Acta Cryst*, vol. 49, pp. 576–578, 1993.

[94] W. Page, "Crystal structure." Accessed: 2019-19-09.

[95] S. R. Vippagunta, H. G. Brittain, and D. J. Grant, "Crystalline solids," *Advanced drug delivery reviews*, vol. 48, no. 1, pp. 3–26, 2001.

[96] A. R. Allnatt and A. B. Lidiard, *Atomic Transport in Solids*. Cambridge University Press, 1993.

[97] K. Kallay, *Interfacial Dynamics*. CRC Press, 2000.

[98] P. E. J. Flewitt and R. K. Wild, "Grain boundaries: their microstructure and chemistry," *Grain Boundaries: Their Microstructure and Chemistry, by PEJ Flewitt, RK Wild, pp. 338. ISBN 0-471-97951-1. Wiley-VCH, April 2001.*, p. 338, 2001.

[99] W. Wolfer and M. Ashkin, "Diffusion of vacancies and interstitials to edge dislocations," *Journal of Applied Physics*, vol. 47, no. 3, pp. 791–800, 1976.

[100] S. Mayburg, "Vacancies and interstitials in heat treated germanium," *Physical Review*, vol. 95, no. 1, p. 38, 1954.

[101] A. G. Squires, D. O. Scanlon, and B. J. Morgan, "Native defects and their doping response in the lithium solid electrolyte li7la3zr2o12," *Chemistry of Materials*, vol. 2019, no. ja, p. null, 0.

[102] C. P. Flynn, *Point defects and diffusion*, vol. 826. Clarendon Press Oxford, 1972.

[103] G. Vineyard and G. Dienes, "The theory of defect concentration in crystals," *Physical Review*, vol. 93, no. 2, p. 265, 1954.

[104] M. Gillan, "The volume of formation of defects in ionic crystals," *Philosophical Magazine A*, vol. 43, no. 2, pp. 301–312, 1981.

[105] W. D. K. Yet-Ming Chiang, Dunbar P. Birnie, *Physical Ceramics: Principles for Ceramic Science and Engineering*. Massachusetts, USA: John Wiley and Sons Inc., 1996.

[106] J. Rousset, E. Saucedo, and D. Lincot, "Extrinsic doping of electrodeposited zinc oxide films by chlorine for transparent conductive oxide applications," *Chemistry of Materials*, vol. 21, no. 3, pp. 534–540, 2009.

[107] A. M. Christie, S. J. Lilley, E. Staunton, Y. G. Andreev, and P. G. Bruce, "Increasing the conductivity of crystalline polymer electrolytes," *Nature*, vol. 433, no. 7021, p. 50, 2005.

[108] J. Kilner, "Fast anion transport in solids," *Solid State Ionics*, vol. 8, no. 3, pp. 201–207, 1983.

[109] J. B. Goodenough, "Ceramic solid electrolytes," *Solid State Ionics*, vol. 94, no. 1-4, pp. 17–25, 1997.

[110] Inflibnet, "Aliovalent doping of cations."

[111] S. Zha, C. Xia, and G. Meng, "Effect of gd (sm) doping on properties of ceria electrolyte for solid oxide fuel cells," *Journal of Power Sources*, vol. 115, no. 1, pp. 44–48, 2003.

[112] C. R. A. Catlow, "Atomistic mechanisms of ionic transport in fast-ion conductors," *Journal of the Chemical Society, Faraday Transactions*, vol. 86, no. 8, pp. 1167–1176, 1990.

[113] P. Vashishta, J. N. Mundy, and G. Shenoy, "Fast ion transport in solids: electrodes and electrolytes," 1979.

[114] G. Mahan, *Superionic conductors*. Springer Science & Business Media, 2013.

[115] M. Y. He X., Zhu Y., "Origin of fast ion diffusion in super-ionic conductors," *Nature Communications*, vol. 8, no. 15893, 2017.

[116] P. M. Fahey, P. Griffin, and J. Plummer, "Point defects and dopant diffusion in silicon," *Reviews of modern physics*, vol. 61, no. 2, p. 289, 1989.

[117] A. Suzuki and Y. Mishin, "Atomistic modeling of point defects and diffusion in copper grain boundaries," *Interface science*, vol. 11, no. 1, pp. 131–148, 2003.

[118] C. Catlow, "Static lattice simulation of structure and transport in superionic conductors," *Solid State Ionics*, vol. 8, no. 2, pp. 89 – 107, 1983.

[119] P. Heitjans and S. Indris, "Diffusion and ionic conduction in nanocrystalline ceramics," *Journal of Physics: Condensed Matter*, vol. 15, no. 30, p. R1257, 2003.

[120] G. Murch, "The nernst-einstein equation in high-defect-content solids," *Philosophical Magazine A*, vol. 45, no. 4, pp. 685–692, 1982.

[121] K. Dill and S. Bromberg, *Molecular driving forces: statistical thermodynamics in biology, chemistry, physics, and nanoscience*. Garland Science, 2012.

[122] J. O. Bockris, A. K. Reddy, and M. Gamboa-Aldeco, *Modern Electrochemistry: Fundamentals of Electrodics. V. 2a*. Plenum Press, 1998.

[123] D. Prot and C. Monty, "Self-diffusion in α–al2o3. ii. oxygen diffusion in undopedsingle crystals," *Philosophical Magazine A*, vol. 73, no. 4, pp. 899–917, 1996.

[124] S. I. Smedley, *The interpretation of ionic conductivity in liquids*. Springer Science & Business Media, 2012.

[125] A. Bogicevic, C. Wolverton, G. M. Crosbie, and E. B. Stechel, "Defect ordering in aliovalently doped cubic zirconia from first principles," *Physical Review B*, vol. 64, no. 1, p. 014106, 2001.

[126] D. Brandon, "The structure of high-angle grain boundaries," *Acta metallurgica*, vol. 14, no. 11, pp. 1479–1484, 1966.

[127] M. Verkerk, B. Middelhuis, and A. Burggraaf, "Effect of grain boundaries on the conductivity of high-purity zro2 y2o3 ceramics," *Solid State Ionics*, vol. 6, no. 2, pp. 159–170, 1982.

[128] A. Nowick *et al.*, "The grain-boundary effect in doped ceria solid electrolytes," *Journal of Solid State Chemistry*, vol. 35, no. 3, pp. 325–333, 1980.

[129] A. Alva, M. Sumner, and W. Miller, "Relationship between ionic strength and electrical conductivity for soil solutions," *Soil Science*, vol. 152, no. 4, pp. 239–242, 1991.

[130] N. Sata, K. Eberman, K. Eberl, and J. Maier, "Mesoscopic fast ion conduction in nanometre-scale planar heterostructures," *Nature*, vol. 408, pp. 946–9, 12 2000.

[131] C. Hammond and C. Hammond, *The Basics of Cristallography and Diffraction*, vol. 214. Oxford, 2001.

[132] C. F. Macrae, P. R. Edgington, P. McCabe, E. Pidcock, G. P. Shields, R. Taylor, M. Towler, and J. Streek, "Mercury: visualization and analysis of crystal structures," *Journal of Applied Crystallography*, vol. 39, no. 3, pp. 453–457, 2006.

[133] A. P. Sutton and V. Vitek, "On the structure of tilt grain boundaries in cubic metals i. symmetrical tilt boundaries," *Philosophical Transactions of the Royal Society of London. Series A, Mathematical and Physical Sciences*, vol. 309, no. 1506, pp. 1–36, 1983.

[134] P. Tasker and D. Duffy, "On the structure of twist grain boundaries in ionic oxides," *Philosophical Magazine A*, vol. 47, no. 6, pp. L45–L48, 1983.

[135] L. F., M. Islam, D. B., and M. P., "Structural, magnetic, electronic, defect, and diffusion properties of cr 2 o 3 : A dft+ u study," *The Journal of Physical Chemistry C*, vol. 118, pp. 18133–18145, 08 2014.

[136] D. Wolf, "Structure-energy correlation for grain boundaries in fcc metalsiv. asymmetrical twist (general) boundaries," *Acta Metallurgica et Materialia*, vol. 38, no. 5, pp. 791–798, 1990.

[137] D. Wolf, "Structure-energy correlation for grain boundaries in fcc metalsiii. symmetrical tilt boundaries," *Acta metallurgica et materialia*, vol. 38, no. 5, pp. 781–790, 1990.

[138] G. A. Chadwick and D. A. Smith, *Grain boundary structure and properties.* Academic Press, 1976.

[139] V. Gertsman, "Coincidence site lattice theory of multicrystalline ensembles," *Acta Crystallographica Section A: Foundations of Crystallography*, vol. 57, no. 6, pp. 649–655, 2001.

[140] E. Lehockey, A. Brennenstuhl, and I. Thompson, "On the relationship between grain boundary connectivity, coincident site lattice boundaries, and intergranular stress corrosion cracking," *Corrosion Science*, vol. 46, no. 10, pp. 2383–2404, 2004.

[141] I. MacLaren and M. Aindow, "Analysis of the reference structure adopted by a mixed tilt-twist vicinal high-angle grain boundary in titanium," *Philosophical Magazine A*, vol. 76, no. 4, pp. 871–888, 1997.

[142] J. Maier, "Space charge regions in solid two-phase systems and their conduction contribution I. conductance enhancement in the system ionic conductor-inert phase and application on AgCl:Al_2O_3 and AgCl:SiO_2," *J. Phys. Chem. Sol.*, vol. 46, no. 3, pp. 309 – 320, 1985.

[143] J. Maier, "Defect chemistry in heterogeneous systems," *Solid State Ionics*, vol. 75, pp. 139 – 145, 1995.

[144] Porous35, "Space charge layer in semiconductors." Accessed 2019-19-09.

[145] S. Braun, C. Yada, and A. Latz, "A thermodynamically consistent model for space-charge-layer formation in a solid electrolyte," *Journal of Physical Chemistry C*, vol. 119, pp. 22281–22288, 09 2015.

[146] J. Maier, "Enhancement of the ionic conductivity in solid-solid-dispersions by surface induced defects," *Ber. Buns. Phys. Chem.*, vol. 88, no. 11, pp. 1057–1062, 1984.

[147] S. Kim, J. Fleig, and J. Maier, "Space charge conduction: Simple analytical solutions for ionic and mixed conductors and application to nanocrystalline ceria," *Phys. Chem. Chem. Phys.*, vol. 5, pp. 2268–2273, 2003.

[148] H. Helmholtz, "Ueber einige gesetze der vertheilung elektrischer ströme in körperlichen leitern, mit anwendung auf die thierisch-elektrischen versuche (schluss.)," *Annalen der Physik*, vol. 165, no. 7, pp. 353–377, 1853.

[149] M. Gouy, "Sur la constitution de la charge electrique a la surface d'un electrolyte," *J. Phys. Theor. Appl.*, vol. 9, no. 1, pp. 457–468, 1910.

[150] D. L. Chapman, "LI. a contribution to the theory of electrocapillarity," *The London, Edinburgh, and Dublin philosophical magazine and journal of science*, vol. 25, no. 148, pp. 475–481, 1913.

[151] J. Frenkel, "The surface motion of particles in crystals and the natural roughness of crystalline faces," *Z. Eksperiment. Teor. Fizik.*, vol. 16, no. 1, pp. 39–52, 1946.

[152] K. Lehovec, "Space-charge layer and distribution of lattice defects at the surface of ionic crystals," *The Journal of Chemical Physics*, vol. 21, no. 7, pp. 1123–1128, 1953.

[153] K. L. Kliewer and J. S. Koehler, "Space charge in ionic crystals. I. general approach with application to NaCl," *Phys. Rev.*, vol. 140, pp. A1226–A1240, Nov 1965.

[154] J. M. Blakely and S. Danyluk, "Space charge regions at silver halide surfaces: Effects of divalent impurities and halogen pressure," *Surf. Sci.*, vol. 40, no. 1, pp. 37 – 60, 1973.

[155] R. Poeppel and J. Blakely, "Origin of equilibrium space charge potentials in ionic crystals," *Surface Science*, vol. 15, no. 3, pp. 507 – 523, 1969.

[156] D. McLean, *Grain Boundaries in Metals*. Clarendon Press, 1957.

[157] M. F. Yan, R. M. Cannon, and H. K. Bowen, "Space charge contribution to solute segregation near grain boundaries," *MRS Proceedings*, vol. 5, p. 57, 1981.

[158] D. R. Franceschetti, "Local thermodynamic formalism for space charge in ionic crystals," *Sol. Stat. Ionics*, vol. 2, no. 1, pp. 39 – 42, 1981.

[159] P. C. McIntyre, "Equilibrium point defect and electronic carrier distributions near interfaces in acceptor-doped strontium titanate," *J. Am. Ceram. Soc.*, vol. 83, no. 5, pp. 1129–1136, 2000.

[160] R. A. De Souza, "The formation of equilibrium space-charge zones at grain boundaries in the perovskite oxide $SrTiO_3$," *Phys. Chem. Chem. Phys.*, vol. 11, pp. 9939–9969, 2009.

[161] R. A. D. Souza, Z. A. Munir, S. Kim, and M. Martin, "Defect chemistry of grain boundaries in proton-conducting solid oxides," *Solid State Ionics*, vol. 196, no. 1, pp. 1 – 8, 2011.

[162] "Lambert w function." Accessed 2019-09-24.

[163] J. Jamnik, J. Maier, and S. Pejovnik, "Interfaces in solid ionic conductors: Equilibrium and small signal picture," *Sol. Stat. Ionics*, vol. 75, pp. 51–58, 1995.

[164] M. C. Gobel, G. Gregori, and J. Maier, "Numerical calculations of space charge layer effects in nanocrystalline ceria. part I: comparison with the analytical models and derivation of improved analytical solutions," *Phys. Chem. Chem. Phys.*, vol. 16, pp. 10214–10231, 2014.

[165] M. C. Gobel, G. Gregori, and J. Maier, "Numerical calculations of space charge layer effects in nanocrystalline ceria. part II: detailed analysis of the space charge layer properties," *Phys. Chem. Chem. Phys.*, vol. 16, pp. 10175–10186, 2014.

[166] E. Fabbri, D. Pergolesi, and E. Traversa, "Topical review ionic conductivity in oxide heterostructures: the role of interfaces," *Science and Technology of Advanced Materials - SCI TECHNOL ADV MATER*, vol. 11, 10 2010.

[167] J. Jamnik and J. Maier, "Defect chemistry and chemical transport involving interfaces," *Solid State Ionics*, vol. 119, no. 1, pp. 191 – 198, 1999.

[168] D. S. Mebane and R. A. De Souza, "A generalised space-charge theory for extended defects in oxygen-ion conducting electrolytes: from dilute to concentrated solid solutions," *Energy Environ. Sci.*, vol. 8, pp. 2935–2940, 2015.

[169] J. W. Cahn and J. E. Hilliard, "Free energy of a nonuniform system. I. interfacial free energy," *J. Chem. Phys.*, vol. 28, no. 2, pp. 258–267, 1958.

[170] D. M. Duffy and P. W. Tasker, "A calculation ofthe formation energies of intrinsic defects near grain boundaries in nio," *Philosophical Magazine A*, vol. 50, pp. 143–154, 02 1985.

[171] A. Lindman, E. E. Helgee, and G. Wahnström, "Theoretical modeling of defect segregation and space-charge formation in the $BaZrO_3$ (210)[001] tilt grain boundary," *Sol. Stat. Ionics*, vol. 252, pp. 121 – 125, 2013. SSPC-16 Conference Proceedings SSI Special Issue.

[172] E. E. Helgee, A. Lindman, and G. Wahnström, "Origin of space charge in grain boundaries of proton-conducting $BaZrO_3$," *Fuel Cells*, vol. 13, no. 1, pp. 19–28, 2013.

[173] J. M. Polfus, T. Norby, and R. Bredesen, "Proton segregation and space-charge at the $BaZrO_3$ (001)/MgO (001) heterointerface," *Sol. Stat. Ionics*, vol. 297, pp. 77–81, 2016.

[174] P. W. Atkins, *Physical Chemistry*. Oxford University Press, 1998.

[175] J. Maier, "Defect chemistry: Composition, transport, and reactions in the solid state; part i: Thermodynamics," *Angewandte Chemie International Edition in English*, vol. 32, no. 3, pp. 313–335, 1993.

[176] P. Jungwirth, *Density Functional Theory. A Practical Introduction. By David Sholl and Janice A. Steckel.*, vol. 49. John Wiley and Sons Inc., 2010.

[177] J. J. J., *Thermodynamics for practical kesterite photovoltaics*. PhD thesis, University of Bath, Bath, England, 2016.

[178] D. W. Davies, *Materials Discovery using chemical heuristics and high-throughput calculations*. PhD thesis, University of Bath, Bath, England, 2018.

[179] P. Hohenberg and W. Kohn, "Inhomogeneous electron gas," *Phys. Rev.*, vol. 136, pp. B864–B871, Nov 1964.

[180] B. L. A., *Phase Stability and Composition of Tin Sulfide for Thin-Film Solar Cells*. PhD thesis, University of Bath, Bath, England, 2014.

[181] W. Kock and M. Holthausen, *A Chemists Guide to Density Functional Theory*. Wiley, 2001.

[182] C. W. M. Castleton, A. Höglund, and S. Mirbt, "Density functional theory calculations of defect energies using supercells," *Modelling and Simulation in Materials Science and Engineering*, vol. 17, p. 084003, nov 2009.

[183] M. Born and K. Huang, *Dynamical Theory of Crystal Lattices*. Oxford classic texts in the physical sciences, Clarendon Press, 1988.

[184] L. H. and C. W., "Ewald summation for coulomb interactions in a periodic supercell." Accessed: 2019-19-09.

[185] P. P. Ewald, "Die berechnung optischer und elektrostatischer gitterpotentiale," *Annalen der Physik*, vol. 369, no. 3, pp. 253–287, 1921.

[186] J. Allen, *A computational study of the adsorption of water and carbon dioxide at oxide surfaces*. PhD thesis, University of Bath, Bath, England, 2009.

[187] J. E. Jones and S. Chapman, "On the determination of molecular fields. —ii. from the equation of state of a gas," *Proceedings of the Royal Society of London. Series*

A, Containing Papers of a Mathematical and Physical Character, vol. 106, no. 738, pp. 463–477, 1924.

[188] N. F. Mott and M. J. Littleton, "Conduction in polar crystals. i. electrolytic conduction in solid salts," *Trans. Faraday Soc.*, vol. 34, pp. 485–499, 1938.

[189] A. M. Karo and J. R. Hardy, "Calculation of point-defect energies and displacements in alkali halides using the lattice-statics method," *Phys. Rev. B*, vol. 3, pp. 3418–3425, May 1971.

[190] "Abulsfia thesis." `http://abulafia.mt.ic.ac.uk/publications/theses/ball/2-Methodology.pdf`. Accessed: 2019-02-13.

[191] T. X. T. Sayle, M. Molinari, S. Das, U. M. Bhatta, G. Möbus, S. C. Parker, S. Seal, and D. C. Sayle, "Environment-mediated structure, surface redox activity and reactivity of ceria nanoparticles," *Nanoscale*, vol. 5, pp. 6063–6073, July 2013.

[192] R. Kutner, "Chemical diffusion in the lattice gas of non-interacting particles," *Physics Letters A*, vol. 81, no. 4, pp. 239 – 240, 1981.

[193] S. Kim, "Isn't the space charge potential in ceria-based solid electrolytes largely overestimated?," *Phys. Chem. Chem. Phys.*, 2016.

[194] H. Tuller and A. Nowick, "Doped ceria as a solid oxide electrolyte," *Journal of the Electrochemical Society*, vol. 122, no. 2, pp. 255–259, 1975.

[195] F. Giannici, G. Gregori, C. Aliotta, A. Longo, J. Maier, and A. Martorana, "Structure and oxide ion conductivity: Local order, defect interactions and grain boundary effects in acceptor-doped ceria," *Chemistry of Materials*, vol. 26, no. 20, pp. 5994–6006, 2014.

[196] V. V. Kharton, F. M. Figueiredo, L. Navarro, E. N. Naumovich, A. V. Kovalevsky, A. A. Yaremchenko, A. P. Viskup, A. M. F. M. B. Carneiro, F. M. B. Marques, and J. R. Frade, "Ceria-based materials for solid oxide fuel cells," *Journal of Materials Science*, vol. 36, no. 5, pp. 1105–1117, 2001.

[197] S. Kim and J. Maier, "On the conductivity mechanism of nanocrystalline ceria," *J. Electrochem. Soc.*, vol. 149, no. 10, pp. J73–J83, 2002.

[198] H. J. Avila-Paredes, K. Choi, C.-T. Chen, and S. Kim, "Dopant-concentration dependence of grain-boundary conductivity in ceria: A space-charge analysis," *J. Mater. Chem.*, vol. 19, pp. 4837–4842, 2009.

[199] U. Anselmi-Tamburini, F. Maglia, G. Chiodelli, A. Tacca, G. Spinolo, P. Riello, S. Bucella, and Z. A. Munir, "Nanoscale effects on the ionic conductivity of highly doped bulk nanometric cerium oxide," *Adv. Func. Mater.*, vol. 16, no. 18, pp. 2363–2368, 2006.

[200] D. V. Laethem, J. Deconinck, D. Depla, and A. Hubin, "Finite element modelling of the ionic conductivity of acceptor doped ceria," *J. Euro. Ceram. Soc.*, vol. 36, no. 8, pp. 1983 – 1994, 2016.

[201] J. Schoonman, "Nanoionics," *Solid State Ionics*, vol. 157, no. 1, pp. 319 – 326, 2003. Proceedings of the 6th International Symposium on Systems with Fast Ionic Transport (ISSFIT).

[202] A. V. Chadwick and S. L. Savin, "Structure and dynamics in nanoionic materials," *Solid State Ionics*, vol. 177, no. 35, pp. 3001 – 3008, 2006. Proceedings of the E-MRS Symposium P on Solid State Ionics: Mass and Charge Transport at Various Length Scales.

[203] J. Maier, "Nanoionics: Ion transport and electrochemical storage in confined systems," *Nature Mater.*, vol. 4, pp. 805–815, 2005.

[204] J. Maier, "Nanoionics: ionic charge carriers in small systems," *Phys. Chem. Chem. Phys.*, vol. 11, pp. 3011–3022, 2009.

[205] J. Maier, "Defect chemistry and ion transport in nanostructured materials: Part ii. aspects of nanoionics," *Solid State Ionics*, vol. 157, no. 1, pp. 327 – 334, 2003. Proceedings of the 6th International Symposium on Systems with Fast Ionic Transport (ISSFIT).

[206] J. Jamnik and J. Maier, "Nanocrystallinity effects in lithium battery materials aspects of nano-ionics. part iv," *Phys. Chem. Chem. Phys.*, vol. 5, pp. 5215–5220, 2003.

[207] H. L. Tuller, "Ionic conduction in nanocrystalline materials," *Solid State Ionics*, vol. 131, no. 1, pp. 143 – 157, 2000.

[208] J. Maier, "Defect chemistry and ionic conductivity in thin films," *Solid State Ionics*, vol. 23, no. 1, pp. 59 – 67, 1987.

[209] F. Chiabrera, I. Garbayo, and A. Taranc'17 - nanoionics and interfaces for energy and information technologies," in *Metal Oxide-Based Thin Film Structures* (N. Pryds and V. Esposito, eds.), Metal Oxides, pp. 409 – 439, Elsevier, 2018.

[210] P. Balaya, A. Bhattacharyya, J. Jamnik, Y. Zhukovskii, E. Kotomin, and J. Maier, "Nano-ionics in the context of lithium batteries," *Journal of Power Sources*, vol. 159, no. 1, pp. 171 – 178, 2006. Special issue including selected papers from the 3rd International Conference on Materials for Advanced Technologies (ICMAT 2005, Singapore, Malaysia) and the Summer School on Synthesis of Nanostructured Materials for Polymer Batteries (Augustoland) together with regular papers.

[211] Q. N. Chen, S. B. Adler, and J. Li, "Imaging space charge regions in sm-doped ceria using electrochemical strain microscopy," *Appl. Phys. Lett.*, vol. 105, no. 20, 2014.

[212] E. C. C. Souza and J. B. Goodenough, "The origin of grain boundary capacitance in highly doped ceria," *Phys. Chem. Chem. Phys.*, vol. 18, pp. 5901–5904, 2016.

[213] P. F. Yan, T. Mori, A. Suzuki, Y. Y. Wu, G. J. Auchterlonie, J. Zou, and J. Drennan, "Grain boundary's conductivity in heavily yttrium doped ceria," *Sol. Stat. Ionics*, vol. 222—223, pp. 31 – 37, 2012.

[214] M. G. Bellino, D. G. Lamas, and N. E. Walsöe de Reca, "Enhanced ionic conductivity in nanostructured, heavily doped ceria ceramics," *Adv. Func. Mater.*, vol. 16, no. 1, pp. 107–113, 2006.

[215] D. Pérez-Coll, P. Núnez, J. C. Ruiz-Morales, J. P. na Martínez, and J. R. Frade, "Re-examination of bulk and grain boundary conductivities of $Ce_{1-x}Gd_xo_{2-\delta}$ ceramics," *Electrochim. Acta*, vol. 52, no. 5, pp. 2001–2008, 2007.

[216] M. C. Gobel, G. Gregori, and J. Maier, "Size effects on the electrical conductivity of ceria: Achieving low space charge potentials in nanocrystalline thin films," *The Journal of Physical Chemistry C*, vol. 117, no. 44, pp. 22560–22568, 2013.

[217] J. Bae, Y. Lim, J.-S. Park, D. L. S. Hong, J. An, and Y.-B. Kim, "Thermally-induced dopant segregation effects on the space charge layer and ionic conductivity of nanocrystalline gadolinia-doped ceria," *J. Electrochem. Soc.*, vol. 163, pp. 919–926, 2016.

[218] Z. Lu, W. Xu, W. Zhu, Q. Yang, X. Lei, J. Liu, Y. Li, X. Sun, and X. Duan, "Three-dimensional nife layered double hydroxide film for high-efficiency oxygen evolution reaction," *Chem. Commun.*, vol. 50, pp. 6479–6482, 2014.

[219] B. Scrosati, "Recent advances in lithium ion battery materials," *Electrochimica Acta*, vol. 45, no. 15, pp. 2461 – 2466, 2000.

[220] F. Zheng, M. Kotobuki, S. Song, M. O. Lai, and L. Lu, "Review on solid electrolytes for all-solid-state lithium-ion batteries," *Journal of Power Sources*, vol. 389, pp. 198 – 213, 2018.

[221] Y. Zhao and L. L. Daemen, "Superionic conductivity in lithium-rich anti-perovskites," *Journal of the American Chemical Society*, vol. 134, no. 36, pp. 15042–15047, 2012. PMID: 22849550.

[222] X. L, G. Wu, J. W. Howard, A. Chen, Y. Zhao, L. L. Daemen, and Q. Jia, "Li-rich anti-perovskite li3ocl films with enhanced ionic conductivity," *Chem. Commun.*, vol. 50, pp. 11520–11522, 2014.

[223] X. L, J. W. Howard, A. Chen, J. Zhu, S. Li, G. Wu, P. Dowden, H. Xu, Y. Zhao, and Q. Jia, "Antiperovskite li3ocl superionic conductor films for solidstate liion batteries," *Advanced Science*, vol. 3, 3 2016.

[224] S. Stegmaier, J. Voss, K. Reuter, and A. C. Luntz, "Li+ defects in a solid-state li ion battery: Theoretical insights with a li3ocl electrolyte," *Chemistry of Materials*, vol. 29, no. 10, pp. 4330–4340, 2017.

[225] B. Chen, C. Xu, and J. Zhou, "Insights into grain boundary in lithium-rich anti-perovskite as solid electrolytes," *Journal of The Electrochemical Society*, vol. 165, no. 16, pp. A3946–A3951, 2018.

[226] "Derivative approximation by finite differences." `https://www.geometrictools.com/Documentation/FiniteDifferences.pdf`. Accessed: 2019-03-15.

[227] "Finite difference method." http://www.mathematik.uni-dortmund.de/ kuzmin/cfdintro/lecture4.pdf. Accessed: 2019-03-15.

[228] E. Barsoukov and J. Macdonald, *Impedance Spectroscopy: Theory, Experiment, and Applications*. Wiley, 2005.

[229] M. Grossi and B. Ricco, "Electrical impedance spectroscopy (eis) for biological analysis and food characterization: a review," *J. Sens. Sens. Syst.*, vol. 6, pp. 303 – 325, 2017.

[230] N. J. Kidner, N. H. Perry, T. O. Mason, and E. J. Garboczi, "The brick layer model revisited: Introducing the nano-grain composite model," *Journal of the American Ceramic Society*, vol. 91, no. 6, pp. 1733–1746, 2008.

[231] J. Bauerle, "Study of solid electrolyte polarization by a complex admittance method," *Journal of Physics and Chemistry of Solids*, vol. 30, pp. 2657–2670, Dec. 1969.

[232] U. Ahmadu, T. Salkus, S. Jonah, A. Musa, and N. Rabiu, "Equivalent circuit models and analysis of impedance spectra of solid electrolyte na0.25li0.75zr2(po4)3," *Advanced Materials Letters*, vol. 4, pp. 185–195, 03 2013.

[233] N. Beekmans and L. Heyne, "Correlation between impedance, microstructure and composition of calcia-stabilized zirconia," *Electrochimica Acta*, vol. 21, no. 4, pp. 303 – 310, 1976.

[234] J.-H. Hwang, D. S. McLachlan, and T. O. Mason, "Brick layer model analysis of nanoscale-to-microscale cerium dioxide," *J. Electroceram.*, vol. 3, no. 1, pp. 7–16, 1999.

[235] H. N, "Ionic conductivity of tho2- and zro2-based electrolytes between 300 and 2000 k," *Solid State Ionics*, vol. 13, no. 3, pp. 255 – 263, 1984.